RSC Advances

REVIEW

View Article Online
View Journal | View Issue

Cite this: *RSC Adv.*, 2025, **15**, 30921

Metal–organic framework/MXene-based materials: preparations and applications

Shasha Zheng, * Keke Zhou, Xiaoxue Zhang and Ning Ren

Metal–organic framework (MOF) materials have attracted significant attention due to their high surface area and adjustable pore structure, which enable potential applications across various fields. However, their practical application is often hindered by poor electrical conductivity and limited structural stability. Integrating MOF with two-dimensional transition metal carbides/nitrides (MXene) offers a powerful strategy to overcome these limitations, synergistically combining the porous architecture of MOF with the exceptional conductivity and mechanical robustness of MXenes. Notably, the performance of MOF/MXene-based materials is governed by the diversification of MOF components. This review provides a systematic and comprehensive analysis of MOF/MXene-based materials, emphasizing a component-driven design approach. These materials are classified into three different types: pure MOF/MXene, MOF composite/MXene, and MOF derivative/MXene, and their synthetic strategies are detailed, including *in situ* growth, solvothermal/hydrothermal methods, self-assembly, and co-precipitation method. Further exploration was conducted on their advanced performance in multifunctional applications such as batteries, supercapacitors, sensors, catalysts, and electromagnetic wave absorbing materials.

Received 22nd June 2025
Accepted 11th August 2025

DOI: 10.1039/d5ra04436g

rsc.li/rsc-advances

1. Introduction

The relentless progress in scientific innovation has driven the development of novel nanomaterials, whose outstanding physicochemical characteristics enable extensive applicability across diverse fields.[1–4] Among these, metal–organic framework (MOF) nanomaterials, a class of compounds constructed through the coordination of metal ions or clusters with organic ligands to form one-, two-, and three-dimensional (1D, 2D, and 3D) structures, have garnered significant attention.[5–8] The exceptionally high specific surface area and tunable porosity of MOF materials endow them with superior adsorption and separation performance.[9–11] Furthermore, the structural and functional versatility of MOF materials has enabled their application in fields such as catalysis,[12–14] energy storage,[15–17] and so on.[18–20] Despite these advantages, MOF materials also present certain limitations, including insufficient chemical stability, inadequate mechanical strength, poor electrical conductivity, and restricted adsorption capacity and selectivity.[21–23] To address these challenges and fully exploit the potential of MOF materials, the design of MOF-based composites has emerged as a promising strategy.[24–27] By integrating MOF materials with other functional materials, synergistic effects can be achieved, effectively combining the strengths of each component while compensating for their individual deficiencies.[28–31]

MXene, a novel class of 2D transition metal carbides and nitrides with the general formula $M_{n+1}X_nT_x$ (M = early transition metals; X = carbon and/or nitrogen; T_x = surface functional groups), has garnered significant attention in advanced materials science.[32–36] Its unique 2D layered structure imparts exceptional electrical conductivity, good mechanical flexibility, intrinsic hydrophilicity, and abundant surface functional groups (*e.g.*, –OH, –F, –O).[37–41] These properties render MXene a highly promising material for diverse applications, including batteries,[42,43] supercapacitors (SCs),[44,45] catalysis,[46,47] water purification,[48–50] adsorption,[51,52] sensors,[53–55] and various other fields.[56–60] Nevertheless, practical implementation of MXene is hindered by several intrinsic limitations, such as oxidative instability, restacking of the 2D nanosheets, and a relatively limited number of accessible active sites.[61–63] A particularly effective approach to overcome these challenges involves the integration of MXene with MOF porous materials. This hybridization generates significant synergistic effects: the porous structure of MOF materials can serve as a structural scaffold to prevent the restacking of MXene nanosheets, thereby preserving their high surface area and excellent electrical conductivity.[64–68] Conversely, the highly conductive MXene network facilitates efficient electron transport, serving as a rapid charge transfer channel that markedly enhances the typically sluggish charge transfer kinetics of the inherently less conductive MOF component.[69–71] The distinctiveness of MOF/MXene-based materials lies in the unique synergy offered by MXene, which sets them apart from other common MOF-based hybrids. Compared to MOF/carbon nanotubes (CNTs), the 2D

College of Energy Engineering, Huanghuai University, Zhumadian, 463000, Henan, P. R. China. E-mail: zhengshasha@huanghuai.edu.cn

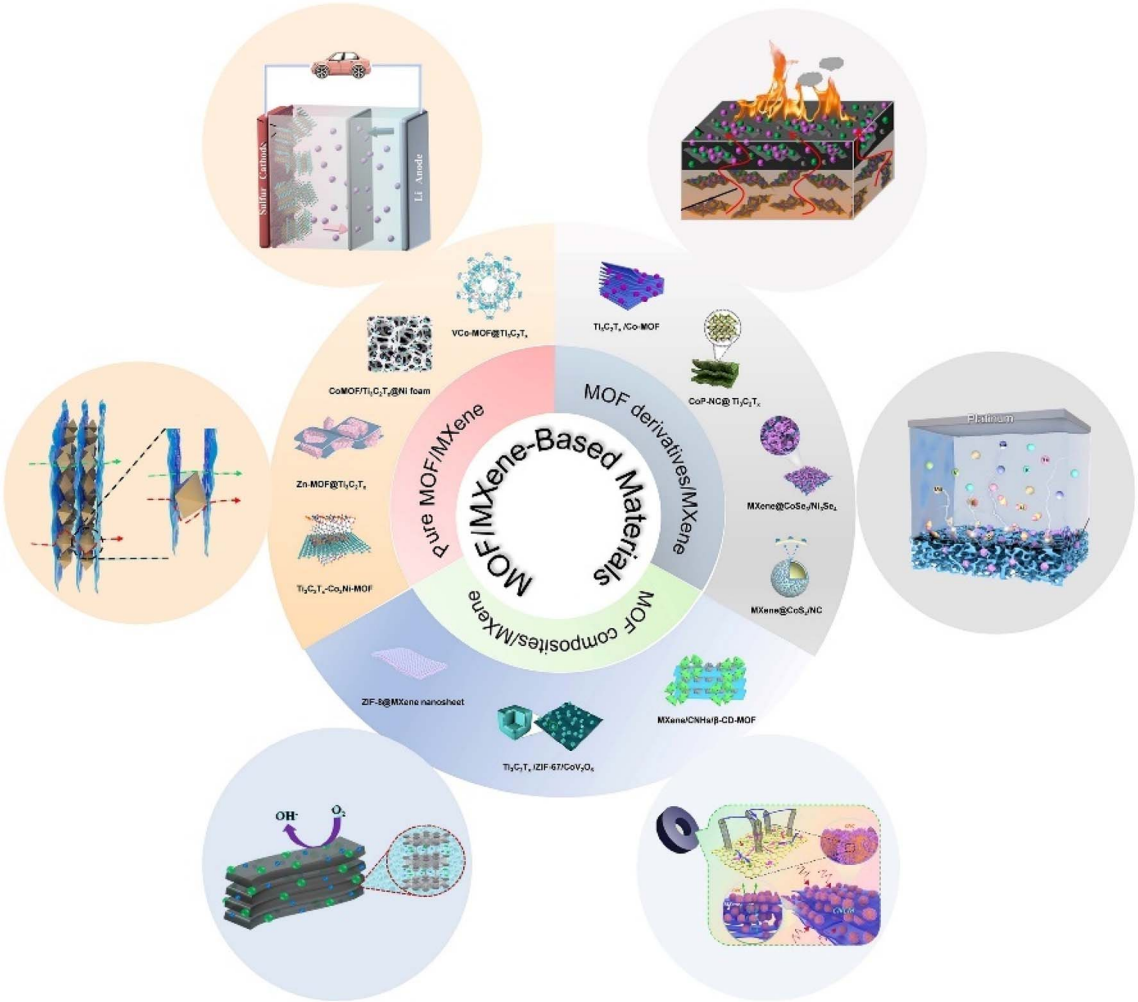

Scheme 1 Overview of MOF/MXene-based materials and their application fields.

structure of MXene provides a larger contact interface and better dispersion.[63,72] Unlike MOF/graphene, MXene's rich surface functional groups enable strong chemical bonding with MOF materials, forming stable heterojunctions.[73,74] In contrast to MOF/metal nanoparticles (NPs), MXene enhances both conductivity and stability cost-effectively.[75,76] Finally, compared to MOF/polymer composites, MXene integration directly addresses the core issue of poor electrical conductivity.[77–79] This multifaceted advantage positions MOF/MXene-based materials as a highly attractive class of materials.

Numerous comprehensive reviews have been conducted on MOF/carbon-based materials,[80–84] MOF/polymers,[85–90] MOF/quantum dots (QDs),[91–93] MOF/metal NPs,[94–96] and other MOF composites.[97–103] However, in the field of MOF/MXene-based materials, despite a series of valuable reviews have been reported, they generally have limited scope. Many reviews focus on specific applications (such as energy storage,[72,77,104–109] catalysis,[75,110,111] biomedical,[78] wastewater treatment,[112,113] electromagnetic interference shielding,[114] *etc.*) or specific types of materials (such as MOF derivatives/MXene[115]), resulting in a fragmented understanding of this field. Therefore, there is currently a lack of a comprehensive, systematic, and up-to-date review that covers the complete system of MOF/MXene-based materials from basic classification, synthesis strategies to diverse applications. Compared with these existing reviews, the main purpose of this review is to provide a comprehensive and detailed analysis of MOF/MXene-based materials, providing a reference for researchers in materials science, chemistry, and engineering fields to fully understand this dynamic field.

It is worth noting that the diversity of MOF components (including pure MOF, MOF composite and MOF derivative) in MOF/MXene-based materials has a decisive influence on the material properties. To our knowledge, there are currently no comprehensive reports on the component classification, synthesis strategies and multiple application potentials of MOF/MXene-based materials. Therefore, this review focuses on the classification of MOF/MXene-based materials, with emphasis on their preparation techniques and application fields. As shown in Scheme 1, MOF/MXene-based materials are systematically classified into three primary categories based on their MOF constituents: pure MOF/MXene, MOF composite/MXene, and MOF derivative/MXene. Their applications span

a wide range of fields, including batteries, SCs, sensors, catalysis, and absorption, among others. Furthermore, the future development trends and challenges that need to be addressed with MOF/MXene-based materials are also discussed.

2. Synthesis of MOF/MXene-based materials

MXene materials, featuring abundant surface functional groups and excellent electrical conductivity, are considered promising substrates for enhancing the stability and electrical conductivity of MOF materials.[116–119] The integration of MOF and MXene is driven by interfacial interactions between the two components. The surface functional groups of MXene serve as active sites for the heterogeneous nucleation of MOF. Metal ions from the MOF precursor solution are attracted to the negatively charged oxygen-containing groups on the MXene surface *via* electrostatic interactions. This initial adsorption facilitates the coordination of organic ligands, initiating MOF growth directly on the MXene substrate.[65,120] Crucially, beyond physical interactions, strong chemical bonding often occurs at the interface, forming stable heterojunctions. Coordination bonds can form between the metal atoms (Ti) in the MXene layer and the donor atoms (O, N) from the organic ligands of MOF, such as Ti–O–C or Ti–N.[113,121]

This synergistic interaction has attracted significant research attention toward developing MOF/MXene-based materials through various synthetic strategies. These composites not only promote advancements in material design but also expand the application potential of MOF-based materials.[73,122–125] As shown in Scheme 2, these composites are systematically classified into three main types based on their MOF constituents: pure MOF/MXene, MOF composites/MXene, and MOF derivatives/MXene. The primary synthesis methods for MOF/MXene-based materials encompass *in situ* synthesis, hydrothermal synthesis, electrostatic self-assembly, solvothermal method, and co-precipitation method. This section provides a comprehensive overview of the preparation of various MOF/MXene-based materials employing these different methods.

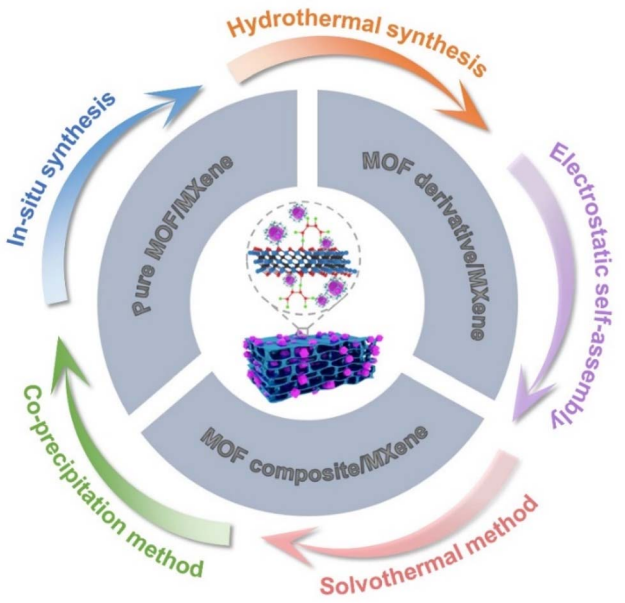

Scheme 2 Classification and synthesis methods of MOF/MXene-based materials.

2.1. Pure MOF/MXene

Pure MOF/MXene composite materials are categorized into seven distinct categories according to the type of metal ions present in the MOF structure: (1) Fe-MOF/MXene, exemplified by $Ti_3C_2T_x$/MIL-53(Fe),[126] synthesized *via* an *in situ* growth method; (2) Co-MOF/MXene, represented by Ti_3C_2-ZIF-67,[127] fabricated through self-assembly; (3) Ni-MOF/MXene, such as Ni-MOF@$Ti_3C_2T_x$,[128] constructed using a solvothermal approach; (4) Cu-MOF/MXene, including Cu-MOF/MXene/glassy carbon electrode (GCE),[129] directly synthesized without intermediate steps; (5) Zn-MOF/MXene, typified by Zn-MOF-Ti_3C_2,[130] prepared *via* a one-pot electrostatic self-assembly strategy in aqueous solution; (6) Zr-MOF/MXene, as demonstrated by MOF-801@MXene nanosheets,[131] synthesized *via* an *in situ* strategy under ambient conditions; (7) bimetallic MOF/MXene, such as CoNi-ZIF-67@$Ti_3C_2T_x$,[132] synthesized through coprecipitation process.

2.1.1. Fe-MOF/MXene. Liu *et al.*[126] fabricated a novel $Ti_3C_2T_x$/MIL-53(Fe) composite (TiCFe) through *in situ* integration of MIL-53(Fe) with layered $Ti_3C_2T_x$ MXene. Initially, Ti_3AlC_2 MAX phase was selectively etched using hydrofluoric acid (HF) to generate accordion-like $Ti_3C_2T_x$ nanosheets. The negatively charged surface of the exfoliated MXene facilitated the adsorption of metal ions, promoting their coordination with MIL-53(Fe). This synergistic interaction resulted in a hierarchical TiCFe architecture, which exhibited an enhanced specific surface area and abundant accessible active sites. Furthermore, a Fe-MOF/MXene hybrid material was developed by Xiao *et al.*[133] through a straightforward solvothermal approach, enabling the direct growth of Fe-MOF crystals on $Ti_3C_2T_x$ MXene substrates. This composite retained the characteristic octahedral morphology of pristine Fe-MOF while significantly enhancing charge transfer efficiency through the incorporation of MXene. In the same year, Jia *et al.*[134] designed a 2D hybrid electrode by utilizing $Mn_{n+1}X_nT_x$ as the electrode of the SCs, integrating electrochemically active sites from Fe-MOF (MIL-100(Fe)) to construct an interfacial columnar structure on the $Ti_3C_2T_x$ MXene layer. Through chemical bond coupling, the Fe-MOF nanospheres and MXene nanosheets were transformed into a 3D multilayer porous nanostructure, which not only suppressed MXene aggregation but also preserved the laminar flow of reaction sites within the composite electrode. Similarly, Li *et al.*[135] synthesized butylimidazolium chloride (BIC)-modified MIL-101(Fe), denoted as BIC@MIL-101(Fe), by the solvothermal synthesis method. Subsequently, by employing vacuum-assisted self-assembly technology, they successfully prepared MXene-BIC@MIL-101(Fe) composite membrane exhibiting excellent structural stability, high mechanical

strength, and good separation performance. Recently, Wang *et al.*[136] fabricated a hydroxyl-rich MXene@MOF composite by the *in situ* growth of Fe-based MOF on MXene, inspired by the structure of bacterial cell walls, for the efficient isolation of lysozyme. In contrast, Han *et al.*[137] developed an innovative solar-driven evaporation system through synergistically integrating MXene with Fe-MOF@cellulose acetate/polyvinyl pyrrolidone. Their approach combined electrospinning and vacuum-assisted filtration to effectively couple the photothermal conversion properties of MXene with the enhanced hydraulic conductivity of electrospun cellulose acetate substrates. This design optimized both solar energy utilization and fluid transport, leading to significantly improved evaporation efficiency under solar irradiation. Meanwhile, Liu *et al.*[138] synthesized self-reporting molecularly imprinted polymers as internal reference probes and *in situ* grew Fe-MOF on MXene as signal nanoprobes, which were applied in a ratiometric electrochemical biosensor for rapid and effective detection of *Staphylococcus aureus*.

2.1.2. Co-MOF/MXene. In 2018, Ramachandran and colleagues fabricated a Co-MOF/$Ti_3C_2T_x$ composite directly on Ni foam (NF) through *in situ* hydrothermal deposition. Fig. 1a schematically illustrates the fabrication procedure for the Co-MOF/$Ti_3C_2T_x$@NF composite. The porous structure of Co-MOF matrices, coupled with the high electrical conductivity of 2D $Ti_3C_2T_x$ nanosheets, synergistically enhances the availability of catalytic sites and facilitates efficient ionic diffusion. As illustrated in Fig. 1c and d, scanning electron microscopy (SEM)

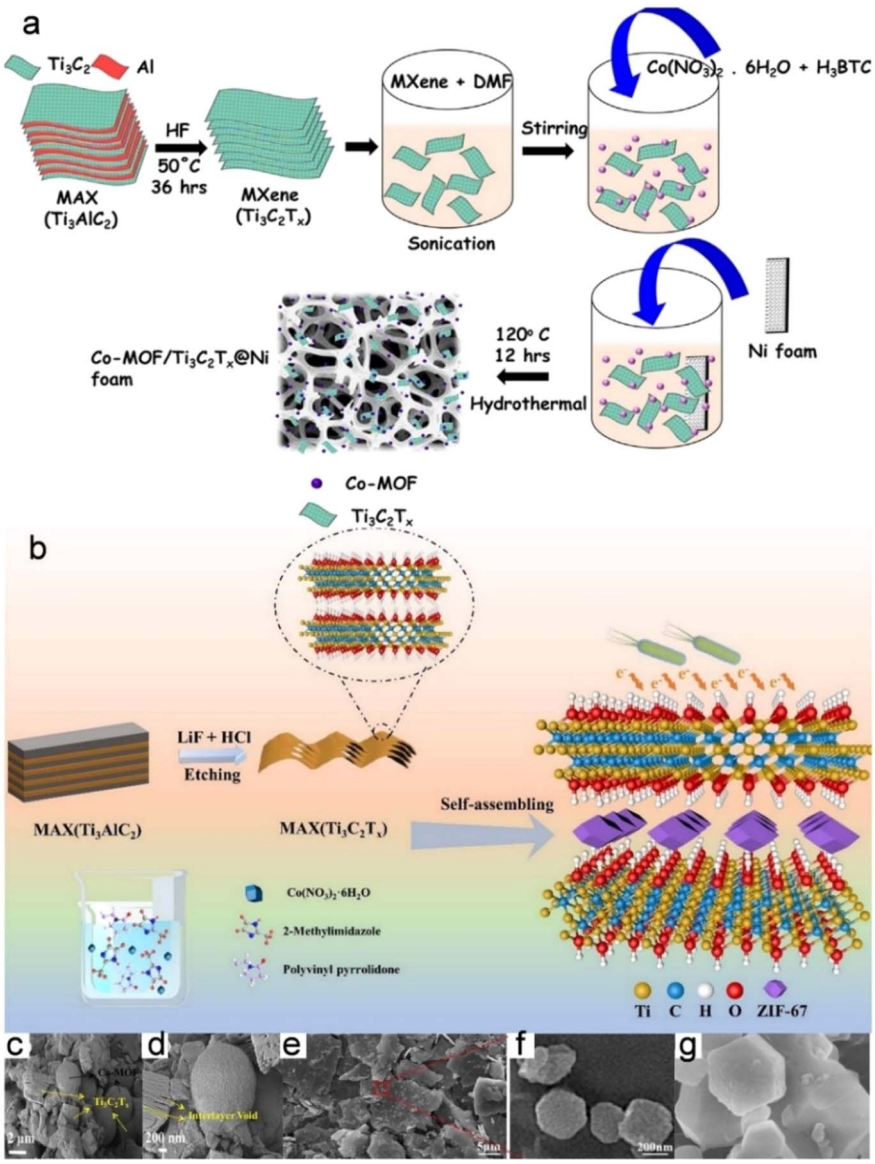

Fig. 1 (a) The synthesis process of Co-MOF/$Ti_3C_2T_x$@NF composite. (b) Synthesis mechanism of the MXene-ZIF67. SEM images of Co-MOF/$Ti_3C_2T_x$@NF (c and d), ZIF-67@MXene hybrid (e and f), and MXene-ZIF67 (g). (a, c and d) Reproduced with permission.[139] Copyright 2018, Elsevier. (e and f) Reproduced with permission.[141] Copyright 2022, Multidisciplinary Digital Publishing Institute. (b and g) Reproduced with permission.[127] Copyright 2022, Elsevier.

analysis confirms the uniform coating and strong interfacial adhesion between the 2D $Ti_3C_2T_x$ nansheets and Co-MOF on the NF substrate.[139] In 2021, Liang *et al.* utilized *in situ* growth to prepare ZIF-67@Ti_3C_2.[140] Transmission electron microscopy (TEM) images reveal the hybrid structure, with ZIF-67 particles, averaging approximately 800 nm in diameter, uniformly anchored on the surface of Ti_3C_2. Subsequently, Wan *et al.* developed an innovative ZIF-67 functionalized MXene composite using sequential precipitation synthesis. This hybrid material was subsequently integrated into thermoplastic polyurethane (TPU) matrices through melt compounding technology. The synthesis process involved dissolving 2.9 g (0.01 mol) of cobalt nitrate hexahydrate in 250 mL of methanol under continuous magnetic stirring for 10 min, followed by a 24 h aging period. Post-synthesis purification included sequential washing, vacuum filtration, and thermal drying at 80 °C for 24 h to obtain the final MXene/Co-ZIF composite. As illustrated in Fig. 1e and f, the resulting hybrid structure demonstrates unique interfacial features. MXene nanosheets with reactive surface groups (–O, –OH, and/or –F) facilitate effective chemical grafting, while ZIF-67 NPs provide abundant unsaturated cobalt coordination sites, promoting strong heterogeneous interfacial bonding. This mutual interaction promotes uniform dispersion of ZIF-67 crystallites across MXene lamellae, simultaneously achieving particle size refinement through surface confinement effects. The engineered TPU nanocomposites exhibited remarkable thermal performance enhancements, particularly demonstrating significant reduction in heat release rate alongside improved thermostability.[141]

Concurrently, Yang *et al.* developed a "sandwich-like" Ti_3C_2-ZIF-67 composite through cubic-structured intercalation within MXene layer. Fig. 1b illustrates the fabrication process, in which MXene nanosheets were derived through selective HF etching of Al atoms from Ti_3AlC_2 precursors. The surface functional groups, which acquired negative charges during the etching process, facilitated the immobilization of ZIF-67 on the MXene substrate. Structural characterization, as evidenced by SEM image (Fig. 1g), confirmed the formation of ZIF-67 crystals, exhibiting a distinct crystalline morphology. The ZIF-67 NPs were uniformly modified on both sides of the MXene nanosheets. This composite material harnessed the combined advantages of its constituent components, namely, the hydrophilicity and conductivity of MXene and the biocompatibility of MOF. The composite exhibited exceptional colonization potential for microorganisms and maintained remarkable species diversity, while the synergistic interactions within the microbial consortium significantly improved bioelectricity production efficiency.[127] In addition to the above preparation strategies, there are some synthesis strategies about $Ti_3C_2T_x$/ZIF-67 have been reported simultaneously.[142,143]

In addition, Roy *et al.*[144] constructed a hierarchical Co-MOF-MXene@carbon black electrode architecture for electrochemical sensor electrodes and point-of-care testing chips by synthesizing MXene-supported Co-MOF-based nanocomposites and integrating them with carbon black ink through 3D printing technology. Ding *et al.*[145] adopted an interdiffusion reaction strategy to construct a 0D/2D heterostructure *via* self-assembling Co-MOF onto highly conductive MXene nanosheets, enabling the design of highly reliable room-temperature gas sensing devices. In this architecture, the MXene nanosheets served as highly conductive core substrates, promoting efficient electron and mass transport while suppressing the agglomeration of MOF NPs during solution self-assembly. Concurrently, the Co-MOF functional sensing layer effectively separated the MXene nanosheets, mitigating their restacking and enhancing the overall thermodynamic stability of the composite.

2.1.3. Ni-MOF/MXene. Qin *et al.*[146] utilized a straightforward self-assembly strategy to construct MXene QDs integrated with 2D Ni-MOF architectures in tunable ratios, thereby forming type II heterojunction structures. The composites demonstrated enhanced absorption and superior interfacial charge transfer ability, as evidenced by their optical and optoelectronic properties. The following year, Cheng *et al.* used layered Ti_3C_2 MXene as a catalyst and employed a facile electrostatic self-assembly process to synthesize 2D composites incorporating ultrathin Ni-MOF nanosheets. The similar layered structure of Ti_3C_2 MXene and Ni-MOF facilitated the formation of a conductive intimate interface, thereby promoting charge transfer and accelerating the separation of photogenerated charge carriers (electrons and holes).[147] Concurrently, Zhang and co-workers reported an innovative MXene-directed synthesis strategy for high-performance SCs using $Ti_3C_2T_x$ MXene/Ni-based MOF composite.[148] Simultaneously, Zhang *et al.* developed an advanced battery-type nickel phosphates-MXene electrode material that is highly suitable for SCs. This material effectively inhibited the aggregation of MXene nanosheets while maintaining a laminar flow structure within the electrode, thereby facilitating rapid ion migration.[149] In 2022, Ganiyat Olatoye *et al.* resolved the challenge of low specific capacitance by depositing Ni-ZIF-67 onto MXene substrates. The researchers first synthesized Ni-ZIF-67 hybrid materials under a controlled temperature gradient (150–450 °C), followed by the fabrication of Ni-ZIF-67-200/K-Ar-MXene composites through modification of intercalated 2D MXene layers (K-Ar-MXene) serving as a structural scaffold.[150]

In addition, to address the inherent limitations of MOF, such as poor conductivity, unsatisfactory stability, and easy aggregation, Zheng *et al.* successfully developed Ti_3C_2 MXene-supported pillared-layer MOF with enhanced cyclability (MXene@Ni-MOF). The hybrid material features a 3D architecture stabilized by Ni–N coordination networks, which confers exceptional structural integrity, as evidenced by sustained performance during cyclic testing. Furthermore, the immobilization of Ni-MOF nanosheets on the MXene substrate facilitates rapid charge transfer between the two components, effectively mitigating the intrinsic low conductivity of Ni-MOF and preventing nanosheet agglomeration (Fig. 2a and b).[70] In Fig. 2c, Wan *et al.* successfully fabricated 3D flower-like Ni-MOFs on multiterminal lamellar MXene using a solvothermal approach and investigated its flame retardant properties in TPU.[128] Concurrently, Yang and colleagues prepared Ni-MOF/V_2CT_x-MXene composites through precisely controlled thermal annealing, resulting in heterostructured materials with hierarchically porous nanorod architectures. This engineered

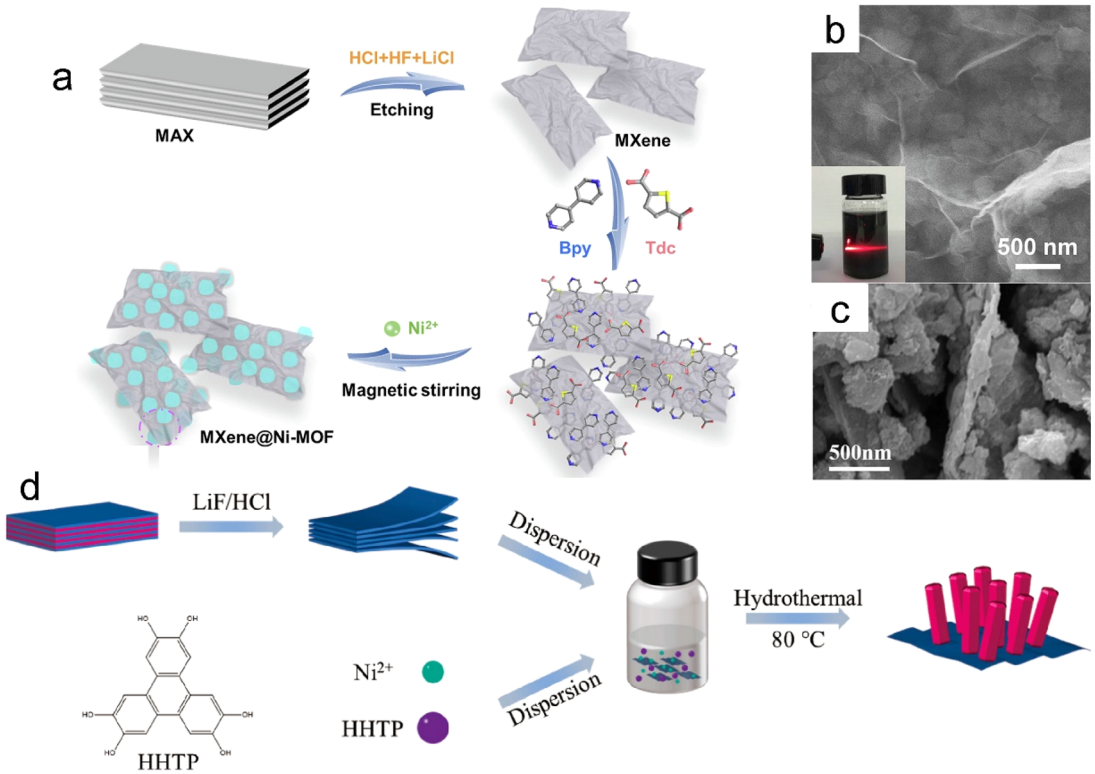

Fig. 2 (a) Schematic illustration of the synthetic process for MXene@Ni-MOF. (b) SEM and optical images of MXene@Ni-MOF. (c) SEM image for Ni-MOF@MXene hybrids. (d) Schematic diagram for the preparation of Ni-MOF/MXene. (a and b) Reproduced with permission.[70] Copyright 2022, Elsevier. (c) Reproduced with permission.[128] Copyright 2022, Elsevier. (d) Reproduced with permission.[152] Copyright 2023, Multidisciplinary Digital Publishing Institute.

composite demonstrated significant improvements in both charge transport efficiency and electrochemically active surface characteristics.[151] In 2023, Li *et al.* leveraged the conductive properties of Ni-MOF and the high strength of $Ti_3C_2T_x$ to enhance the stability of Ni-MOF. The prepared an innovative hybrid material featuring vertically aligned Ni-MOF nanorods on MXene substrates *via* controlled hydrothermal synthesis (Fig. 2d).[152] Additionally, Nanda *et al.* introduced a nickel-containing MXene composite with a nanosheet morphology, synthesized *via* solvothermal treatment in an autoclave. The resulting material demonstrated a high specific energy capacity and improved power delivery characteristics.[153]

The composite of highly conductive MXene and porous conductive MOF ($Ni_3(HITP)_2$, HITP = 2,3,6,7,10,11-hexaaminotriphenylene) has also been widely reported, Lin *et al.*[154] fabricated electrophysiological $Ni_3(HITP)_2$ MOF/MXene electrodes. Xu *et al.*[155] fabricated a temperature sensor with high thermal sensitivity and excellent flexibility by loading conductive $Ni_3(HHTP)_2$ MOF (HHTP = 2,3,6,7,10,11-hexahydroxytriphenylene) onto MXene *via in situ* polymerization. Moreover, the electrochemical performance of MXene was significantly improved by compounding it with Ni-HHTP[156] and (Fe-, Cu-, Co-, Ni)-1,3,5-benzene tricarboxylate (BTC) MOFs,[157] which showed excellent performance for SCs. Shivade *et al.* used an innovative strategy to synthesize Ni-MOF/MXene composites assisted by biomolecule folic acid, which effectively prevented the oxidation and restacking of MXene.[158]

2.1.4. Cu-MOF/MXene. In 2021, a novel 3D flower-like Cu-MOF combined with ultrathin MXene nanosheets was synthesized and studied by Cheng *et al.*[129] The Cu-MOF was synthesized *via* a straightforward, one-step process utilizing copper nitrate and 2-aminoterephthalic acid as the starting materials (Fig. 3a–c). Subsequent progress in MOF engineering was demonstrated by Gu *et al.* through strategic modification of the conventional HKUST-1 framework.[159] Their methodology involved the incorporation of 2D $Ti_3C_2T_x$ MXene components, resulting in a novel composite material exhibiting enhanced structural integrity under hydrothermal conditions (Fig. 3d). Hassan *et al.*[160] prevented the restacking of MXene sheets by integrating them with Cu-BTC MOF, thereby improving the electrochemical performance. However, Liu *et al.*[161] adopted an innovative approach combining thermal induction with solvent-assisted oxygen anion etching, enabling precise modulation of pores in rigid microporous Cu-based MOFs. These engineered MOFs were subsequently assembled with MXene-derived aerogels through self-assembly to construct flexible NO_2 sensing platforms. Sharma *et al.*[162] designed MXene@Cu-TCPP (TCPP = tetrakis (4-carboxyphenyl) porphyrin) hybrid architectures that formed 2D heterogeneous nanostructures by van der Waals forces, exhibiting excellent stability and conductivity. Zhu *et al.*[163] constructed a dimensional-matched

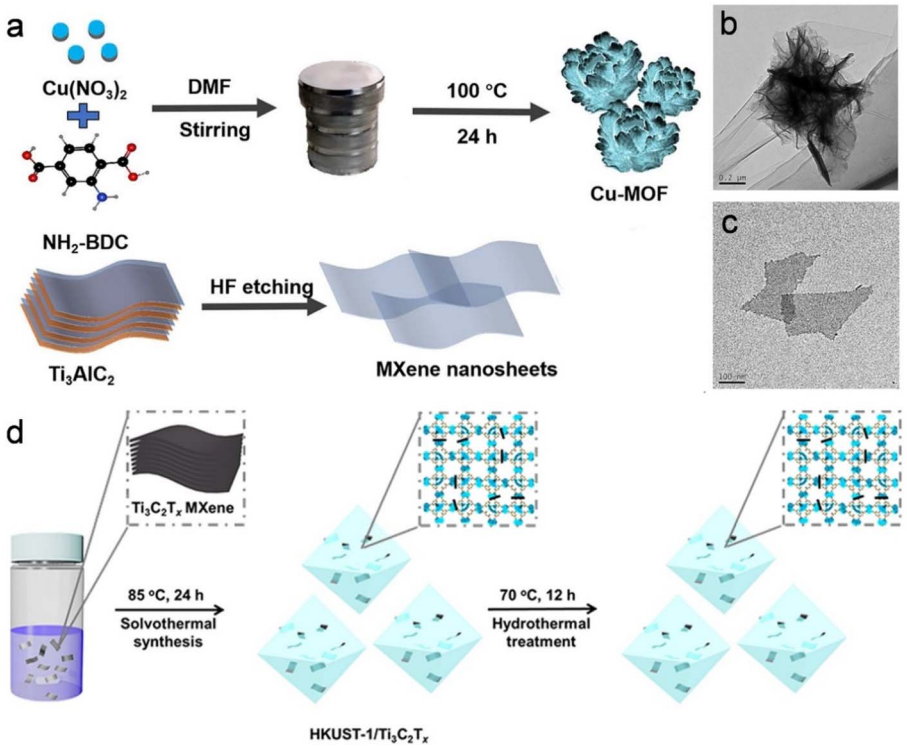

Fig. 3 (a) Preparation of Cu-MOF and MXene nanosheets. TEM images of Cu-MOF (b) and MXene (c). (d) Schematic diagram for the synthesis of HKUST-1/$Ti_3C_2T_x$ MXene hybrid materials. (a–c) Reproduced with permission.[129] Copyright 2021, Wiley. (d) Reproduced with permission.[159] Copyright 2021, American Chemical Society.

organic–inorganic nanohybrid with high light absorption capacity and strong interfacial attraction by combining MXene/TiO_2 with a small amount of Cu-TCPP through a one-step solvothermal method. In addition, Lin *et al.*[164] reported a novel MXene/Cu-TCPP lamellar membrane that achieved efficient pervaporation energy generation by synergistically combining 2D MXene and Cu-TCPP MOF. Wang *et al.*[165] constructed MXene@MOF-based electrochemical biosensors *via* heterogeneous interface design: the TCPP organic ligand was first employed to functionalize MXene nanosheets, followed by surfactant-assisted solvothermal synthesis of MOF, yielding a MXene@MOF architecture with superior stability, enhanced conductivity, and a multilayered folded morphology. This architecture significantly increased electrochemical active sites, enabling label-free, ultrasensitive detection of glycoprotein nonmetastatic melanoma protein B in serum samples from patients with Parkinson's disease.

Recently, Zhou *et al.*[166] drew inspiration from the 3D interlocking hierarchical structure of the skin to construct a multifunctional artificial epidermal device through *in situ* growth of $Cu_3(HHTP)_2$ NPs on the surface of hollow spherical MXene, resulting in a biomimetic MXene@$Cu_3(HHTP)_2$ composite sensor. In this design, the gas-sensitive $Cu_3(HHTP)_2$ is heterogeneously assembled *in situ* at the MXene interface, mimicking the hollow spherical morphology found in skin, thereby structurally emulating the stratum spinosum and stratum granulosum of the epidermis. However, Ge *et al.*[167] proposed an all-solution process method to fabricate a photodetector by sequentially spraying conductive $Cu_3(HHTP)_2$ and MXene onto a Si substrate, forming a van der Waals double heterojunction.[127] The heterojunction structure promotes unidirectional electron hole separation with type I band alignment within the $Cu_3(HHTP)_2$/Si interface, while it also takes advantage of the potential barrier difference between the $Cu_3(HHTP)_2$/Si and MXene/$Cu_3(HHTP)_2$ Schottky junctions. The MXene/$Cu_3(HHTP)_2$/Si photodetector exhibits excellent photoelectric properties.

2.1.5. Zn-MOF/MXene. In 2020, Li *et al.* employed a gentle water freezing-and-thawing approach to exfoliate multilayer MXene, followed by the integration of ZIF-8 NPs into the MXene layers through a straightforward layer-by-layer assembly strategy. The MXene/ZIF-8 composite exhibits unique architectural characteristics, featuring flexible MXene nanosheets with surface corrugations that serve as effective nucleation sites for the controlled growth of ZIF-8. This methodology provides an efficient solution to the persistent challenge of MXene layer restacking commonly encountered in conventional synthesis methods.[168] Concurrently, Yao and co-workers utilized the MXene/ZIF-8 nanocomposite as an electrode material through an *in situ* growth method.[169] At almost the same time, Wang and co-workers prepared MXene/ZIF-8 nanocomposites by mixing the $Zn(NO_3)_2 \cdot 6H_2O$ solution with the 2-methylimidazole solution, followed by stirring for approximately 24 h, and subsequent centrifugation, washing, and drying steps.[170] Rabiee *et al.* constructed an innovative inorganic MXene/MOF-5 nanostructure using a vacuum-assisted filtration process.[171] In 2022,

Guo *et al.* successfully synthesized a bioactive Zn-MOF over the $Ti_3C_2T_x$ nanosheets through *in situ* growth.[172] The fabrication pathway of the Zn-MOF@$Ti_3C_2T_x$ composite is schematically depicted in Fig. 4a. Expanding on earlier work, Yao *et al.* systematically investigated ZIF-8@$Ti_3C_2T_x$ hybrid materials through an optimized single-step microemulsion synthesis.[173] The experimental scheme involved the gradual incorporation of microemulsion phases A and B into $Ti_3C_2T_x$ suspensions, followed by vigorous stirring under ambient conditions. The product was then isolated *via* centrifugation, purified through repeated methanol washes, and finally dehydrated under vacuum at 60 °C. More recently, Jose Paul *et al.* synthesized $[Zn_4(1,2,4,5\text{-benzene-tetra carboxylate})_2(H_2O)_6]_n \cdot 3nH_2O$ MOF using pyromellitic acid-based linkers and $Zn(NO_3)_2 \cdot 6H_2O$ as precursors *via* a reticular synthesis approach. Multilayer MXene was prepared through conventional HF etching, and the MOF-MXene hybrid composite was subsequently constructed through the one-step electrostatic self-assembly process in aqueous medium. As demonstrated in Fig. 4b, this integration process successfully occurred under ambient conditions within distilled water through reticular synthesis principles. SEM and TEM images of the MOF-MXene microstructure (Fig. 4c–e) indicate that the MOF envelops MXene with a casually oriented, block-structured configuration.[130] Deng *et al.* developed polyurethane (PU)-MXene-MOF sponge using an *in situ* growth technique.[174] As shown in Fig. 4f and g, the ZIF-8 NPs were uniformly dispersed on the surface of the PU-MXene sponge, resulting in a significantly roughened surface morphology of the PU-MXene-MOF sponge skeleton. Building upon previous research, Hao *et al.* successfully synthesized MXene@ZIF-8 to a mitigate the inherently low electrical conductivity of MOF.[175] In addition, Shahriyari Far and co-workers fabricated MXOF composites *via* solvothermal growth, demonstrating the synergistic effect between Zn-MOF and MXene nanosheets.[176]

2.1.6. Zr-MOF/MXene. Li *et al.*[131] constructed a significantly improved MOF@MXene membrane for gas separation by a room temperature *in situ* synthesis strategy. Initially, the negatively charged MXene nanosheets immobilized adjacent Zr metal ions through electrostatic interactions. Subsequently, under ambient conditions, these metal ions coordinated with organic ligands, promoting the homogeneous nucleation and growth of MOF-801 crystalline structures on the MXene surfaces, thereby yielding MOF-801@MXene nanosheets. The as-prepared nanocomposites were then uniformly deposited onto a porous organic support *via* vacuum-assisted filtration, ultimately forming the MOF@MXene composite membrane. Wen *et al.*[177] synthesized the 3D hierarchical Zr-MOF/$Ti_3C_2T_x$ nanocomposite through a facile method that involved electrostatic interaction between the $Ti_3C_2T_x$ MXene nanosheet and Zr^{4+}, followed by the solvothermal method for the *in situ* synthesis of Zr-MOF on the $Ti_3C_2T_x$ nanosheets. In addition, Kashif *et al.*[178] fabricated UiO-66/MXene hybrids *via*

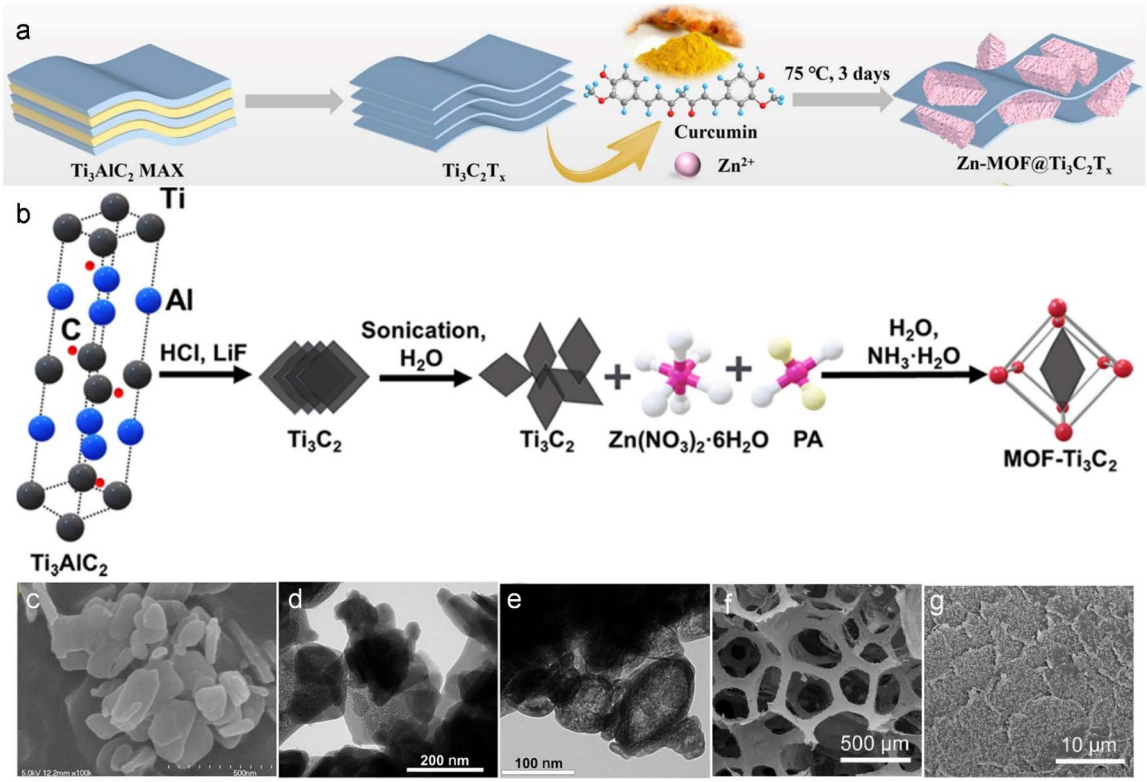

Fig. 4 (a) Schematic diagram for the preparation of Zn-MOF@MXene hybrid. (b) Schematic illustration of the synthetic process for MOF-MXene composite. (c) SEM image of MOF-MXene. (d and e) TEM images of MOF-MXene. (f and g) SEM images of PU-MXene-MOF sponge. (a) Reproduced with permission.[172] Copyright 2022, Wiley. (c–e) Reproduced with permission.[130] Copyright 2023, Elsevier. (f and g) Reproduced with permission.[174] Copyright 2023, Elsevier.

solvothermal method. UiO-66 and MXene were heat treated in solvent to make them closely combined to form composite materials. Xiang *et al.*[179] prepared a polyethylene glycol/MXene@MOF membrane with stable interlayer spacing and excellent antifouling performance by a simple interface self-assembly strategy. In this approach, UiO-66-NH_2 MOF NPs were used as structural supports to induce intercalation within layered MXene nanosheets, effectively tuning the interlayer spacing and enhancing the permeability. Subsequently, hydrophilic polyethylene glycol was introduced through hydrogen bonding, further stabilizing the intercalated architecture. However, Maleki *et al.*[180] focused on the preparation of a novel MXene modified polyether sulfone membrane. By compounding UiO-66-NH_2 NPs with MXene, UiO-66-NH_2@MXene 2D nanocomposites were created to modify polyethersulfone membrane. During the membrane modification process, 0.25 wt% UiO-66-NH_2@MXene nanocomposite was used as modifier to successfully synthesize the modified MXene based polyethersulfone membrane. Recently, Meng *et al.*[181] employed electrostatic self-assembly to rationally integrate NH_2-UiO-66 with MXene nanosheets, resulting in an innovative hybrid material. This process involved the solution-phase mixing of oppositely charged Zr-MOF and MXene components, which spontaneously assembled into an ordered multilayer structure driven by electrostatic interactions.

2.1.7. Bimetallic MOF/MXene. In 2019, Wen *et al.*[132] synthesized CoNi-ZIF-67@$Ti_3C_2T_x$ by *in situ* coprecipitation growth of bimetallic CoNi-ZIF-67 rhombic dodecahedrons on $Ti_3C_2T_x$. The resulting hybrid structure is clearly depicted in the SEM image (Fig. 5a), where the layered structure of $Ti_3C_2T_x$ is well preserved, with uniformly dispersed CoNi-ZIF-67 particles embedded within the interlayer spaces. For comparison, SEM analysis (Fig. 5b) of pristine CoNi-ZIF-67 highlights its distinct morphological features in the absence of $Ti_3C_2T_x$ support. Liu *et al.*[182] engineered 3D MXene/NiCo-MOF composite films by integrating 2D nanosheets with NiCo-MOF nanoflakes through hydrogen bonds, employing vacuum-assisted filtration. This approach initiated with the synthesis of 2D NiCo-MOF nanosheets under ambient conditions, followed by multilayered MXene production through HF etching of Ti_3AlC_2 and subsequent alkalization (Fig. 5f). In 2021, Du *et al.*[183] obtained $Ti_3C_2T_x$/CoNi-MOF nanosheets by *in situ* growth process. Additionally, Wu and co-workers developed the 1D heterostructure *via* integrating MXene fibers with CoNi-MOF.[184] In recent years, Xiao *et al.* demonstrated a novel 2D heterostructure synthesized by vertically growing NiCo-MOF ultrathin nanosheets on exfoliated $Ti_3C_2T_x$ MXene substrates. This architecture effectively integrates the synergistic merits of conductive MXene with the enhanced electrochemical properties inherent to bimetallic MOF nanomaterials.[185] The superior electrical conductivity and effective interfacial compatibility of aminated MXene with electrolytes enables homogeneous *in situ* anchoring of bimetallic NiCo-MOF on its surface. Yue *et al.* successfully prepared highly redox-active NiCo-MOF that were *in situ* stabilized using 2D aminated $Ti_3C_2T_x$.[186] Recently, Tan *et al.*[187] fabricated multiple 2D MOF/$Ti_3C_2T_x$ hybrid materials through electrostatically directed assembly (Fig. 5g). As illustrated in Fig. 5c–e, the atomic force microscope (AFM) characterization of Co_2Ni-MOF@$Ti_3C_2T_x$ reveals a uniform thickness distribution, in contrast to its individual components (Co_2Ni-MOF and $Ti_3C_2T_x$). Beyond these strategies, recent studies[188–191] have reported analogous *in situ* growth methods for fabricating MXene-supported bimetallic NiCo-MOF composites.

In addition to the above-mentioned NiCo-MOF/MXene, other bimetallic MOF/MXene composite materials such as VCo-MOF/MXene, FeCu-MOF/MXene, FeNi-MOF/MXene, FeCo-MOF/MXene, CuZn-MOF/MXene and NiMn-MOF/MXene have also been reported. Li and co-workers synthesized a composite catalyst by *in situ* growth of VCo-MOF on the surface of MXene using a solvothermal method.[192] Furthermore, M. Adil and co-workers synthesized the FeCu MOF/MXene composite *via in situ* hydrothermal growth on NF to form a binder-free electrode.[193] A hybrid electrocatalyst, FeNi-MOF@MXene, composed of Fe, Ni-based MOF (FeNi-BTC MOF) and MXene, was prepared *via* a solvothermal reaction.[194] Meanwhile, Thai *et al.*[195] developed a novel bimetallic FeCo-MOF composite (MIL-100@ZIF-67) supported on MXene nanosheets, resulting in the hybrid material MIL-100@ZIF-67@MXene. To optimize the ion transport pathway and improve the ion permeability, Li *et al.*[196] used block copolymers to generate mesopores within 2D MOF nanosheets, thereby constructing hierarchically porous Cu–Zn-MOF@MXene hybrids. In addition, both Ali *et al.*[197] and Siva Shalini *et al.*[198] synthesized NiMn-MOF nanocomposites through a hydrothermal method, and similarly achieved MXene incorporation into NiMn-MOF to improve electrochemical performance through the same synthetic route.

2.1.8. Others. As mentioned above, a variety of single-metal (Fe, Co, Ni, Cu, Zn, and Zr) and bimetallic (NiCo, VCo, FeCo, FeNi, FeCu, ZnCu, and NiMn) MOF-based materials have been reported for the construction of composites with MXene. In addition to these, several other representative MOF/MXene-based materials incorporating Bi-, Ce-, Al-, Ti-, La-, and Mo-based MOF have also been recently developed. For example, Gong *et al.* fabricated leaf-like MXene-based flame retardants (MXene@Bi-MOF) through the *in situ* growth of shuttle-shaped Bi-MOF on the surface of MXene.[199] Chen *et al.* successfully prepared a novel Ce-MOF/MXene composite *via* employing the 3D straw-sheaf-like Ce-MOF and MXene nanosheets.[200] Meanwhile, Li *et al.*[201] prepared MXene@Ce-MOF composites featuring abundant oxygen vacancies. Zhang *et al.*[202] synthesized MXene@MOF-303(Al) composites through *in situ* growth of MOF-303(Al) on MXene, effectively combining the advantageous properties of both components. Subsequently, a composite membrane composed of MXene@MOF-303(Al), polyvinyl alcohol, and polyacrylonitrile was prepared using the composite as a filler and a polyacrylonitrile ultrafiltration membrane as substrate. In addition, Li *et al.*[203] utilized MXene as a Ti source to synthesize layered Ti-MOF nanosheets *via* organic ligand coordination, followed by strategic integration of mesopores to create multiscale porous MXene-MOF composites with superior charge storage characteristics. Zhao *et al.*[204] achieved *in situ* synthesis of a Ti-based MOF (NH_2-MIL-125) using 2-aminoterephthalic acid and tetrabutyl titanate, concurrently hybridizing it with MXene to form a Ti-MOF@MXene composite

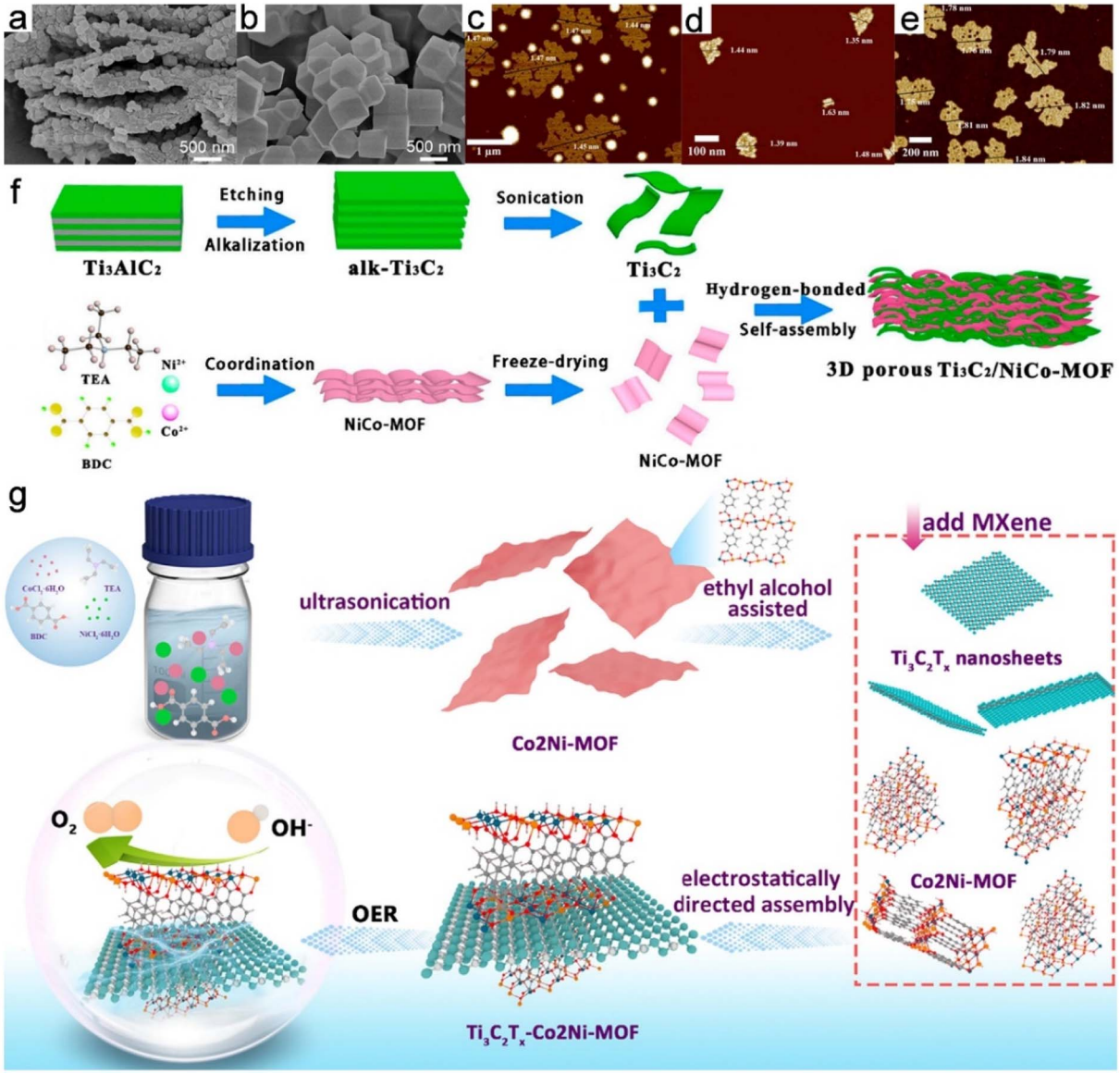

Fig. 5 SEM images of CoNi-ZIF-67@$Ti_3C_2T_x$ (a) and pure CoNi-ZIF-67 (b). AFM images of Co_2Ni-MOF (c), $Ti_3C_2T_x$ (d), and Co_2Ni-MOF@$Ti_3C_2T_x$ (e). (f) Fabrication process of MXene/NiCo-MOF. (g) A scheme for the preparation of MXene/NiCo-MOF. (a and b) Reproduced with permission.[132] Copyright 2019, Molecular Diversity Preservation International. (c–e and g) Reproduced with permission.[187] Copyright 2022, Elsevier. (f) Reproduced with permission.[182] Copyright 2020, Molecular Diversity Preservation International.

material, which was further functionalized with polyethyleneimine and covalently connected immobilized onto a gold electrode to construct a sensing platform. Yu *et al.*[205] developed lanthanide-based La-MOF on MXene nanosheets *via* an *in situ* growth strategy, producing La-MOF@MXene hybrid flame retardants. In addition, Lin *et al.*[206] proposed an interface engineering strategy to construct defect-engineered La-MOF@MXene nanohybrids with oxygen vacancies by synergistic defect and *in situ* growth. Kaur *et al.*[207] fabricated a composite by combining Mo-MOF with MXene (NH_2–Mo-MOF/MXene), which was subsequently deposited onto screen-printed electrodes.

To address structural limitations inherent in conventional MOF synthesis, Wang *et al.*[208] proposed an innovative metal-ion-assisted conversion methodology employing 2D MXene as a precursors. This method enabled the successful fabrication of 3D catechol-functionalized TiCu-HHTP MOFs with a non-interpenetrated $SrSi_2$ architecture. The transformation mechanism involves three synergistic processes: (1) electron transfer from MXene substrates to adsorbed Cu^{2+}, initiating oxidation–reduction reactions, (2) cleavage of Ti–C bonds releasing Ti^{4+} ions, and (3) subsequent coordination of Ti^{4+}/Cu^{2+} with the HHTP ligand to form a stable MOF structure. Notably, this approach exhibits remarkable versatility, V_2CT_x can substitute conventional MXene precursors, and various M^{n+} (Ni^{2+}, Co^{2+}, Mn^{2+}, and Zn^{2+}) can effectively replace the original metal ions, highlighting the broad adaptability of the methodology.

2.1.9 Summary. The synthesis of pure MOF/MXene composites, as detailed in the previous sections, relies on a variety of strategies, among which the selection of metal ions plays a crucial role in determining the best approach and the properties of the composites. A critical comparison reveals the different patterns in the synthesis approaches employed for different metal ions.

(1) *In situ* growth is the most versatile method, successfully applied for Fe-MOF/MXene (*e.g.*, $Ti_3C_2T_x$/MIL-53(Fe)[126]), Zr-MOF/MXene (*e.g.*, MOF-801@MXene[131]), Zn-MOF/MXene (*e.g.*, ZIF-8@$Ti_3C_2T_x$[173]), and bimetallic MOF/MXene (*e.g.*, CoNi-ZIF-67@$Ti_3C_2T_x$[132]). This method generally promotes strong interfacial interaction and good dispersion of MOF on the MXene surface, making it a robust choice for achieving intimate contact.

(2) Solvothermal and hydrothermal methods are frequently used for Co-MOF/MXene (*e.g.*, Co-MOF/$Ti_3C_2T_x$@NF[139]) and Ni-MOF/MXene (*e.g.*, Ni-ZIF-67/MXene[150]). These techniques offer good control over crystal morphology but require high temperatures, which can be detrimental to the stability of MXene if the temperature cannot be precisely controlled.

(3) Self-assembly strategies, including electrostatic self-assembly and vacuum-assisted filtration, are effective for Zn-MOF/MXene (*e.g.*, Zn-MOF-$Ti_3C_2T_x$ *via* one-pot strategy[130]), Ni-MOF/MXene (*e.g.*, MXene QDs coupled with 2D Ni-MOF[146]), and Cu-MOF/MXene (*e.g.*, Cu-BTC MOF/MXene[160]). These methods usually carried out under mild conditions, which is beneficial for preserving the integrity of MXene and is particularly suitable for creating layered or membranous structures.

(4) Coprecipitation is a straightforward method used for the synthesis of bimetallic MOF/MXene composites, such as CoNi-ZIF-67@$Ti_3C_2T_x$,[132] offering a rapid route to bimetallic integration.

In conclusion, while *in situ* growth emerges as the most widely adopted and effective strategy for achieving strong interfacial bonding across various metal ions, the selection of a synthesis method must be carefully tailored to the specific MOF and the desired composite morphology. The diversity of approaches highlighted in this section underscores the flexibility in designing pure MOF/MXene materials, with each method offering a unique balance of interfacial strength, morphological control, and compatibility with the MXene substrate.

2.2. MOF composite/MXene

In recent years, significant research efforts have been devoted to the fabrication of MOF composite/MXene-based materials. These MOF composites typically involve the integration of MOF materials with various functional components, including metal NPs, metal oxides, carbon-based materials, organic compounds, metal hydroxides, and other materials.

With respect to MOF@metal NPs/MXene composites, Dai and co-workers[209] successfully synthesized Zr-Fc MOF/AuNPs/4-mercaptophenylboronic acid (4-MPBA) nanocomposites, which were subsequently integrated with 2D $Ti_3C_2T_x$ MXene. Huang *et al.*[210] introduced a bottom-up synthesis of porous heterostructure substrates by stepwise solvothermal reactions with Zn-based MOFs and MXene nanosheets, and spatially constructed stable ultrafine Pt nanocrystals on them (Pt/ZIF-$Ti_3C_2T_x$). In addition, Wen *et al.*[211] developed a hierarchical assembly approach involving the direct *in situ* growth of porous ZIF-8 nanocrystals on multilayer MXene substrates, followed by the precise immobilization of abundant Pt NPs on the MXene@ZIF-8 hybrid substrate. The resulting MXene@ZIF-8@Pt NPs composite material demonstrates enhanced electrochemical durability and catalytic efficiency, attributed to the complementary characteristics of its constituent materials: the conductive MXene framework, surface-enhanced ZIF-8 matrix, and catalytically active Pt nanostructures. Recently, Zhang *et al.*[212] successfully prepared a Ru-doped Co-MOF@MXene composite catalyst with high conductivity and high catalytic activity, achieved by modulating the electronic structure of Co-pyridinedicarboxylic MOF through Ru doping and room temperature hybridization with MXene nanosheets.

The development of MOF@metal oxide/MXene composites has also advanced significantly. Lu *et al.*[213] successfully fabricated an innovative Fe_3O_4@MXene@MOF-74 composite through a straightforward synthesis strategy. Structural characterization revealed the formation of well-defined crystalline NPs after Fe_3O_4 modification, with Fig. 6a illustrating the homogeneous magnetic integration across the MXene substrate. Elemental mapping analysis quantitatively verified the coexistence of Zn, Fe, C, Ti, and O, thereby verifying the compositional homogeneity and structural integrity of the composite. Liu *et al.*[120] reported a universal strategy for constructing 3D MXene/MOF composites. Through *in situ* growth *via* a coprecipitation reaction, a series of hollow 3D MXene/MOF composites ($Ti_3C_2T_x$/Cu-BTC, $Ti_3C_2T_x$/ZIF-8, $Ti_3C_2T_x$/ZIF-67, $Ti_3C_2T_x$/FeCo-PBA, and $Ti_3C_2T_x$/ZIF-67/CoV_2O) were successfully prepared (Fig. 6e). Furthermore, Chi *et al.*[214] prepared a MXene@SnO_2–Ce-MOF Z-scheme heterojunction with abundant oxygen vacancies as a photoactive material by hydrothermally combining the etched MXene with SnO_2, and then combining it with Ce-MOF prepared by co-precipitation method.

Recently, MOF@carbon-based material/MXene composites have attracted considerable attention. Tu *et al.*[215] synthesized a novel composite material through the integration of MXene with carbon nanohorns and β-cyclodextrin MOFs (MXene/CNHs/β-CD-MOFs). The layered MXene component maintained its characteristic accordion-like configuration, while the CNHs preserved their quasi-spherical nanostructure. Fig. 6b demonstrates the successful encapsulation of MXene/CNHs assemblies within elongated β-CD-MOF crystalline matrices. Rana *et al.*[216] employed a MOF-525@Ecoffex nanocomposite featuring a layer of Ecoffex@MXene@Co-nanoporous carbon (NPC) to construct stretchable and humidity-resistant multifunctional triboelectric nanogenerator (TENG). In this configuration, MOF-525 (Fig. 6c) served as the charge generation layer, while the Co-NPC@MXene nanocomposite (Fig. 6d) functioned as the conductive intermediate layer. However, Rajan *et al.*[217] constructed a ternary heterojunction photocatalyst (Ni-MOF/graphitized carbon nitride (g-C_3N_4)/MXene) through

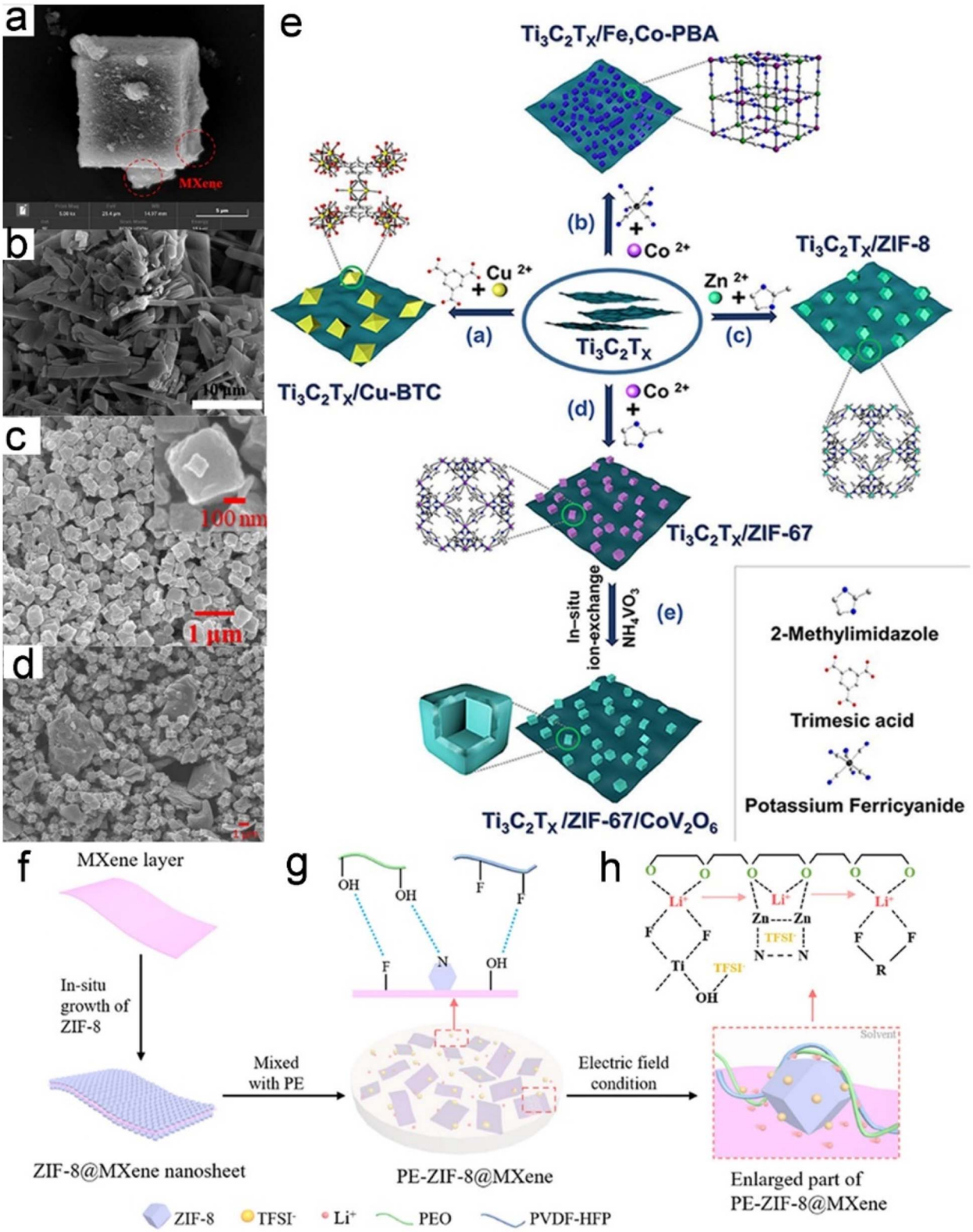

Fig. 6 SEM images of Fe_3O_4@MXene@MOF-74 (a), MXene/CNHs/β-CD-MOFs (b), MOF-525 (c), and MXene@Co-NPC (d). Synthesis procedure of 3D MXene/MOF (e), ZIF-8@MXene (f) and PE-ZIF-8@MXene (g). (h) Schematic illustration of the intermolecular interaction between ZIF-8@MXene, polymer molecules and lithium salt. (a) Reproduced with permission.[213] Copyright 2022, Elsevier. (b) Reproduced with permission.[215] Copyright 2020, Elsevier. (c and d) Reproduced with permission.[216] Copyright 2022, Elsevier. (e) Reproduced with permission.[120] Copyright 2022, Wiley. (f–h) Reproduced with permission.[221] Copyright 2022, Elsevier.

integrated solvothermal synthesis and wet impregnation techniques. This innovative architecture combined Ni-MOF, g-C_3N_4, and MXene, establishing dual charge-transfer mechanisms through an engineered Type II heterojunction configuration coupled with a noble-metal-free Schottky interface. Subsequently, Qi *et al.*[218] engineered a Fe-MOF-NH_2/CNT-NH_2/MXene composite through electrostatic self-assembly, strategically combining positively charged amino-functionalized components (Fe-MOF-NH_2 and CNT-NH_2) with negatively charged MXene, and further prepared molecularly imprinted polymer modified resistive type electrochemical sensor using electropolymerization technology. In addition, Hassan *et al.*[219] synthesized carbon aerogel induced chromium MOF (CA@MIL-101) with $Ti_3C_2T_x$ MXene nanocomposite material (CA@MIL-101-(Cr)/$Ti_3C_2T_x$) by hydrothermal method, which had interconnected porous structure that provided abundant divalent ionic active sites and significantly enhanced charge transfer kinetics. Recently, Lin *et al.*[220] prepared g-C_3N_4 nanosheets using thermal polymerization and peeling method under air conditions. Subsequently, MIL-101(Fe)/g-C_3N_4 composites were constructed using hydrothermal method at 120 °C. Subsequently, MXene nanosheets were added, and MXene@MIL-101(Fe)/g-C_3N_4 composite materials were prepared by solvothermal method. The results showed that MIL-101(Fe)/g-C_3N_4 successfully deposited on the MXene nanosheets.

Building upon advancements in MOF@carbon-based materials/MXene composites, investigators have extended their efforts to engineer MOF@organic compound/MXene composites, aiming to achieve richer functions and performance. Zhao and colleagues[221] engineered a polymer composite electrolyte reinforced with ZIF-8@MXene nanosheet (PE-ZIF-8@MXene) *via* an *in situ* growth process. Fig. 6f–h demonstrate the fabrication process for both ZIF-8@MXene and PE-ZIF-8@MXene, accompanied by molecular-level interaction schematics among the hybrid nanofillers, polymer matrix, and lithium salt components. Guo *et al.*[222] successfully synthesized ZIF-67@MXene/polyimide (PI) hybrid materials with ordered lamellar structures through thermal compression of 3D networked aerogels, where PI was synergistically integrated with MXene-supported ZIF-67 crystalline frameworks. This synthesis method took advantage of the compressibility of the aerogel, which kept the aerogel walls always parallel to the sliding direction and thus provided significant antifriction effect. In addition, Liang *et al.*[223] employed a ternary mixed ligand system comprising Eu^{3+}, 1,3,5-benzenetricarboxylic acid, and terephthalic acid with polydopamine-functionalized MXene (PDA@MXene) to fabricate multilayered sandwich-structured Eu-MOF/PDA@MXene composites through an *in situ* assembly strategy. This synthesis method not only endowed the material with a multilayer porous structure but also realized the magnetic functionalization of the material by uniformly immobilizing Fe_3O_4 NPs in Eu-MOF/PDA@MXene through self-assembly. However, Hou *et al.*[224] reported the successful synthesis of MXene@PDA/MOF composites with a unique honeycomb-like morphology, achieved by *in situ* coordination of 2-methylimidazole and Zn^{2+} on the surface of PDA-modified MXene. This synthesis method endowed the material with extensive surface area and superior electrical conductivity, establishing fundamental advantages for electrochemical sensing applications. Recently, Zhu *et al.*[225] successfully intercalated tannic acid (TA) etched ZIF-8 (TZIF-8) nanocrystals with hollow structures into the interlayer spacing of MXene, thus forming MXene/TZIF-8 membranes with high permeability and good separation effects on various oil-water emulsions. Moreover, Yang *et al.*[226] reported a novel photocatalyst created through *in situ* growth and self-assembly, where MXene served as a support for ZIF-8 MOF immobilization. The MXene@ZIF-8 was further modified with TA and polyphenol compounds to form a cross-linked network that enhanced the heterogeneous interface, which is essential for efficient photocatalysis. The performance of the photocatalyst was optimized by exploring different concentrations of TA.

In addition to the previously described metal NPs, metal oxide, carbon-based materials, organic compound@MOF composites combined with MXene, Sun *et al.*[227] adopted a novel kirkendall effect assisted electrostatic self-assembly method to construct a MOF (MIL-88A) substrate surface decorated with Ni–Fe layered double hydroxide (LDH) and formed multilayer nanocages, which were coated with MXene on the outer surface of the nanocage. By adjusting the adsorption of MXene on the LDH surface, the heterogeneous interface in the MOF-LDH-MXene ternary composite exhibited excellent interfacial polarization loss. Recently, hybrid systems incorporating $MnCO_3$@-MOF,[228] polydimethylsiloxane-MOF@Ag,[229] and the reduced graphene oxide (rGO)/PDA/FeCu-MOF[230] composites with MXene have also been investigated.

The synthesis of MOF composite/MXene materials, as detailed in the preceding sections, is characterized by a remarkable diversity in both the composition of the MOF composite and the strategies used to integrate it with MXene. A critical analysis reveals that the choice of synthesis method often depends on the properties of the MOF composite and the desired final architecture.

(1) *In situ* growth is a powerful strategy for constructing multi-layered or core–shell architectures. This approach was used to prepare Pt/ZIF-$Ti_3C_2T_x$ by sequentially growing ZIF-67 on MXene and then depositing Pt nanocrystals,[210] and to construct the hierarchical MXene@ZIF-8@Pt NPs composite.[211] This method allows for precise, step-by-step engineering of complex heterostructures with strong interfacial contact.

(2) Solvothermal and hydrothermal methods are particularly effective for the synthesis of MOF@metal oxide/MXene and MOF@carbon-based material/MXene composites. The synthesis of Fe_3O_4@MXene@MOF-74 (ref. 213) and the MXene@SnO_2-Ce-MOF Z-scheme heterojunction[214] relied on these techniques. Similarly, the integration of MXene with preformed MIL-101(Fe)/g-C_3N_4 composites was achieved *via* a solvothermal process.[220] These methods are highly suitable for reactions that require controlled temperature and pressure to form crystalline composites.

(3) Self-assembly strategies, including electrostatic self-assembly, vacuum-assisted filtration, and thermal compression, are highly versatile for creating layered, membrane-like, or 3D aerogel-based composites. This approach was used to

synthesize MOF-525@Ecoffex nanocomposites with a MXene@Co-NPC hybrid,[216] to construct ZIF-67@MXene/PI hybrid materials *via* thermal compression of aerogels,[222] and to fabricate MXene/TZIF-8 membranes with high permeability.[225] The self-assembly of MOF@organic compound/MXene composites is also common, as demonstrated by the electrostatic self-assembly of Fe-MOF-NH_2/CNT-NH_2/MXene[218] and the *in situ* growth of ZIF-8@MXene for polymer electrolytes.[221] These methods are often conducted under mild conditions, preserving the integrity of MXene.

(4) Coprecipitation is a direct and scalable method for the *in situ* formation of MOF composites on MXene, as demonstrated by the universal strategy for fabricating hollow 3D MXene/MOF composites.[120]

In conclusion, the synthesis of MOF composite/MXene materials is highly flexible, with the choice of method enabling the design of a wide range of morphologies and architectures. *In situ* growth excels in building complex, multi-component systems, solvothermal/hydrothermal methods are ideal for crystalline composite integration, and self-assembly offers a powerful route to layered and functionalized materials.

2.3. MOF derivative/MXene

MOF derivatives, which exhibit high specific surface area and porosity, structural flexibility, tunable functionality, and excellent chemical stability, have been effectively integrated with MXene, known for its ultra-thin nature, robust mechanical toughness, and superior electrical conductivity. This synergistic combination has garnered significant attention from research groups worldwide. Several successful syntheses of MOF derivative/MXene composites are documented herein, categorized into seven distinct groups based on the variations in MOF derivatives: (1) MOF-derived metal/MXene; (2) MOF-derived metal oxide/MXene; (3) MOF-derived metal phosphide/MXene; (4) MOF-derived metal selenide/MXene; (5) MOF-derived metal sulfide/MXene; (6) MOF-derived metal hydroxide/MXene; (7) carbon-based material derived from MOF/MXene-based materials. Each category presents unique challenges and opportunities, highlighting the diverse potential applications of these composite materials.

2.3.1. MOF-derived metal/MXene. With the increasing demand for high-performance composite materials, the combination of MOF-derived metal-based materials with MXene has emerged as a prominent research focus. Wang *et al.*[231] developed a hierarchical composite through electrostatic-mediated assembly. By leveraging cationic attraction between Co and Fe ions and anionic MXene substrates functionalized with surface-terminating groups, they achieved uniform adsorption of metallic precursors. Subsequent introduction of 1,4-benzenedicarboxylic acid as bridging ligand induced spontaneous coordination assembly, generating interlamellar FeCo-MOF spacers that effectively mitigated MXene restacking through structural confinement. The carbonization protocol under controlled pyrolysis enabled *in situ* formation of bimetallic nanocatalysts, where the spatial restriction from the MOF-derived matrix ensured homogeneous dispersion of FeCo NPs across the MXene scaffolds. The resulting engineered nanohybrids exhibited dual functional advantages: (1) simultaneous high polarity and ionic-electronic conductivity facilitating polysulfide redox mediation, and (2) optimized sulfur electrochemistry through shortened charge-transfer pathways. Notably, the 0D–2D architecture demonstrated synergistic catalytic functionality by integrating metallic active sites with conductive MXene platforms, significantly enhancing sulfur utilization efficiency in energy storage systems.

Furthermore, considering the suboptimal electrochemical performance of MXene layered 2D structures, Haridas B. Parse *et al.*[232] reported the preparation and electrocatalytic ability of a composite material comprising MXene and Co NPs derived from Co-MOF, encapsulated within N-doped carbon (NC). Han and co-workers[233] explored the construction of accordion-like MXene@Co-CZIF and MXene@Ni-CZIF composites (derived from the pyrolysis of Co-ZIF and Ni-ZIF, denoted as Co-CZIF and Ni-CZIF, respectively) *via* an electrostatic self-assembly strategy coupled with subsequent pyrolysis in H_2/Ar atmosphere. As depicted in Fig. 7b, the Co-CZIF component maintained well-defined polyhedral geometry throughout MXene's surface and internal matrix. Fig. 7c demonstrates the effective incorporation of spherical Ni-ZIF nanostructures with hierarchical architecture into the MXene framework through this assembly process, with NPs distributed across both the exterior and interior regions. Xiang *et al.*[234] prepared laminated $Ti_3C_2T_x$/CNTs/Co through combining microwave-assisted synthesis, *in situ* carbonization, and electrostatic assembly methods. A schematic illustration of the nanocomposite formation mechanism is presented in Fig. 7a, while Fig. 7d specifically illustrates the anchoring of sea urchin-shaped CNTs/Co nanostructures onto $Ti_3C_2T_x$ MXene substrates. In a subsequent advancement, Liu and co-workers[235] fabricated $Ti_3C_2T_x$/carbon nanofibers (CNFs)/TiO_2/CoNi nanocomposites *via* electrostatic self-assembly combined with thermal treatment. Fig. 7e–g provide a comprehensive overview of the synthetic pathway and morphological characterization, as revealed by SEM analysis.

2.3.2. MOF-derived metal oxide/MXene. MOF-derived metal oxide-based materials/MXene composites have garnered significant research interest owing to their distinctive structural characteristics and synergistically enhanced functional performance.[236] These hybrid materials effectively combine the intrinsic high catalytic activity of MOF-derived oxides with the excellent electrical conductivity and robust mechanical stability of MXene. This section provides a systematic overview of the prevailing synthetic strategies employed in the fabrication of MOF-derived metal oxide/MXene.

Ji *et al.*[237] prepared uniform-sized MOF structures *via* hydrothermal synthesis, which were subsequently subjected to thermal decomposition to yield hollow Fe_2O_3. Concurrently, MXene was synthesized *via in situ* etching and processed under controlled conditions to enable directional alignment of MXene nanosheets driven by ice-crystal compression, resulting in highly ordered MXene aerogel frameworks. The hollow Fe_2O_3 structures were then dispersed in a silica sol and infiltrated into the porous MXene structure. Ultimately, the processed

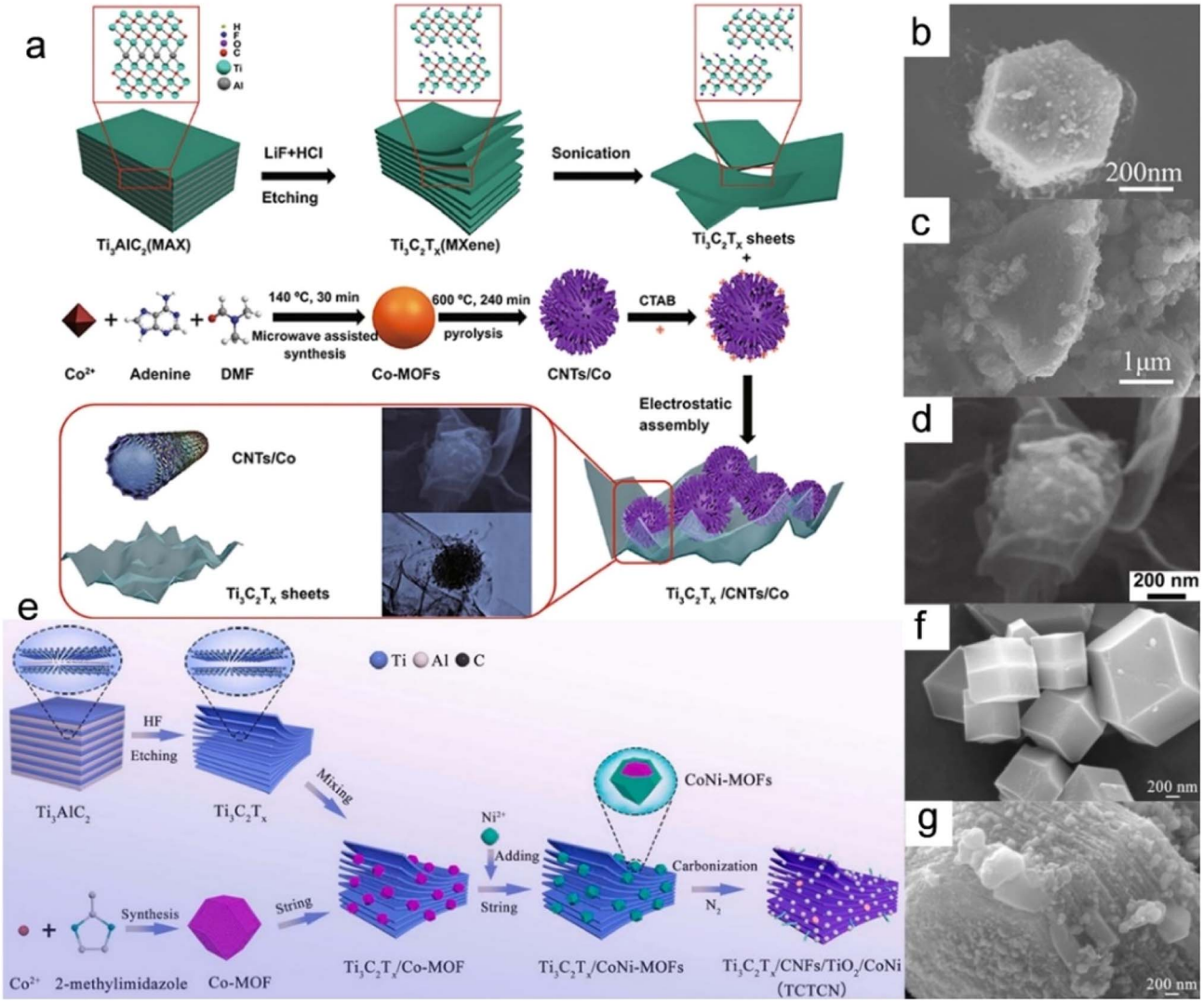

Fig. 7 (a) Synthetic route for $Ti_3C_2T_x$/CNTs/Co nanocomposites. SEM images of MXene@Co-CZIF (b), MXene@Ni-CZIF (c), and $Ti_3C_2T_x$/CNTs/Co (d). (e) Scheme for the preparation of $Ti_3C_2T_x$/CNFs/TiO_2/CoNi nanocomposites. SEM images of CoNi-MOF (f) and $Ti_3C_2T_x$/CNFs/TiO_2/CoNi nanocomposites (g). (a and d) Reproduced with permission.[234] Copyright 2021, Springer. (b and c) Reproduced with permission.[233] Copyright 2020, American Chemical Society. (e–g) Reproduced with permission.[235] Copyright 2022, Elsevier.

composite underwent lyophilization, yielding MXene-Fe_2O_3–SiO_2 aerogels. Xie and co-workers[238] successfully synthesized a flexible electrode film through vacuum filtration integration of $Ti_3C_2T_x$ and MOF-derived Co–Fe oxide porous nanorods. Fig. 8a illustrates the composite fabrication process, which involves three principal stages. Firstly, the precursor Ti_3AlC_2 undergoes chemical etching using HCl/LiF solution, yielding multilayer MXene sediment that is subsequently delaminated into colloidal suspension *via* manual agitation. Concurrently, hydrothermal synthesis produces Co–Fe-MOF nanorod precursors that are subsequently calcined in oxidative atmosphere to generate porous mixed oxide phases. The resulting dispersions are combined and subjected to vacuum-assisted filtration, yielding a free-standing Co–Fe oxide/MXene composite film. In 2022, Lei *et al.*[239] prepared a layered $Ti_3C_2T_x$ hybrid material designated as $Ti_3C_2T_x$@CoFe@TiO_2 through microwave-assisted thermal treatment of CoFe-MOF@$Ti_3C_2T_x$ precursor at multiple temperature gradients, employing an integrated *in situ* synthesis strategy. Shi *et al.*[240] also demonstrated the construction of MOF-derived porous $CoFe_2O_4$@-carbon@alkalized MXene composite architecture using electrospinning, *in situ* growth, and subsequent calcination. Shingte *et al.*[241] embedded MOF-derived rhombic nickel ferrite NPs (NFO NPs) into $Ti_3C_2T_x$ MXene layers by a straightforward blending technique. The embedded NFO NPs served as effective interlayer spacers, mitigating restacking of MXene nanosheets and thereby increasing the accessible surface area of the composite.

Liu *et al.*[242] fabricated a MOF-derived In_2O_3/$Ti_3C_2T_x$ MXene composite using a simple oil-bath method. The synthetic process is illustrated in Fig. 8c. Morphological characterization (Fig. 8d and e) demonstrates the successful growth of pristine

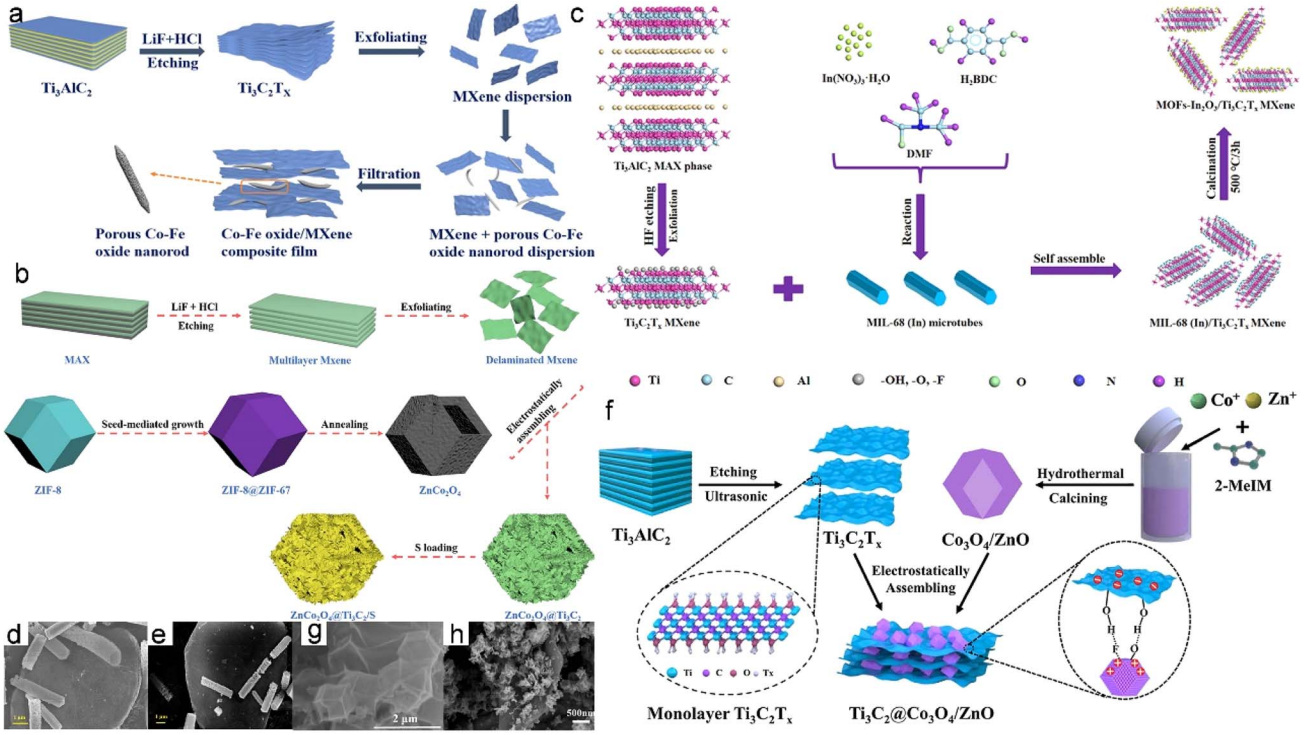

Fig. 8 Schematic fabrication process of Co–Fe oxide/MXene composite film (a), $ZnCo_2O_4$@MXene/S composite (b), and $In_2O_3/Ti_3C_2T_x$ MXene composite (c). (d and e) SEM images of $In_2O_3/Ti_3C_2T_x$ MXene composite. (f) Schematic illustration of the synthesis approach of MXene@Co_3O_4/ZnO composite. (g and h) SEM images of MXene@Co_3O_4/ZnO and Co_3O_4/MXene nanocomposite. (a) Reproduced with permission.[238] Copyright 2020, Elsevier. (b) Reproduced with permission.[244] Copyright 2021, Elsevier. (c–e) Reproduced with permission.[242] Copyright 2022, Elsevier. (f and g) Reproduced with permission.[246] Copyright 2022, Elsevier. (h) Reproduced with permission.[247] Copyright 2022, Elsevier.

In_2O_3 microtubes on delaminated MXene substrates, confirming effective heterostructure formation through this solution-phase approach. Subsequently, Zhang *et al.*[243] successfully synthesized In_2O_3/ZnO/MXene by integrating MOF-derived hollow In_2O_3/ZnO nanotubes with MXene. The process began with the hydrothermal synthesis of MIL-68(In), followed by the introduction of $Zn(NO_3)_2 \cdot 6H_2O$ to form In_2O_3/ZnO hollow nanotubes after calcination. These nanotubes, surface-modified with (3-aminopropyl) triethoxysilane, were dispersed in deionized water and stoichiometrically combined with MXene to yield the final ternary nanocomposite.

Wei and colleagues[244] synthesized the $ZnCo_2O_4$@MXene/S composite. The process involves coating the MXene layer onto hollow $ZnCo_2O_4$ polyhedron through electrostatic assembly, as shown in Fig. 8b. The synthesis commenced with the production of faceted ZIF-8 nanocrystals through Zn^{2+} coordination with 2-methylimidazole in methanol, which subsequently acted as templates for the epitaxial deposition of ZIF-67 shells. A sequential growth approach was then implemented in Co^{2+}-containing methanol solution to construct the core–shell ZIF-8@ZIF-67 architecture. Hollow porous $ZnCo_2O_4$ polyhedrons were obtained after annealing treatment. Afterwards, MXene layers were coated on the surface of hollow $ZnCo_2O_4$ polyhedrons through electrostatic assembly to form $ZnCo_2O_4$@-MXene composites. Finally, sulfur was introduced into $ZnCo_2O_4$@MXene at 155 °C to easily synthesize $ZnCo_2O_4$@MXene/S composites. In 2022, Kshetri *et al.*[245] engineered two specialized electrode architectures: a capacitor-type Co-porous carbon (PC)@MXene-CNF and a battery-type MnO_2@Co_3O_4-PC@MXene-CNF assembly, both strategically constructed through hierarchical integration of Co-MOF@MXene-CNF. By strategically combining MOF-derived components with MXene substrates, Wu *et al.*[246] developed a MXene@Co_3O_4/ZnO hybrid material using an optimized fabrication protocol. The architectural evolution of this multi-level MXene@MOF derivative system is schematically presented in Fig. 8f, revealing its sequential assembly mechanism. The morphological characteristics of the synthesized MXene@Co_3O_4/ZnO material are further evidenced by SEM analysis, with representative microstructural features displayed in Fig. 8g. Recently, Bu *et al.* synthesized the novel mesoporous Co_3O_4/MXene nanocomposites by direct calcination of ZIF-67 grown *in situ* on MXene sheets. The SEM image of $Co_3O_4/Ti_3C_2T_x$ nanocomposite (Fig. 8h) reveals that the surfaces of the $Ti_3C_2T_x$ sheets are entirely covered by Co_3O_4 NPs, demonstrating strong interfacial coupling between constituent phases.[247] Then, Oh *et al.* constructed a simple strategy involving the construction of a 2D structural hybrid material consisting of Co_3O_4 and MXene nanosheets coated with N-doped graphite C (NGC), represented as Co_3O_4@NGC. The presence of MXene nanosheets can impart high electronic conductivity and structural stability to the composite material.[248] Given that the

restacking of 2D layered materials such as MXene limits their practical scalability, Zhou *et al.* prepared an electrocatalyst consisting of MOF-derived hollow CoV_2O_6 nanocubes (TS-V_2CT_x/CoV_2O_6 HN) anchored on lattice-stretched V_2CT_x MXene, achieved through an ion-exchange process followed by liquid nitrogen quenching.[249] To enhance the electronegativity of nanocomposites, Rahman *et al.* engineered a dual-layer triboelectric device with enhanced flexibility and multifunctionality by incorporating MOF-derived nanoporous cobalt oxide (NPCO) blended with silicone polymer alongside MXene-based nanocomposites.[250] Wang *et al.* conducted a series of studies on the construction of a hollow Co_9S_8 core@multi-shell MXene@Bi_2O_3 structure using MOF as a precursor, with optimization of the flexible substrate by varying the concentration of Co_9S_8.[251]

In addition, Wang *et al.*[252] designed a $Ti_3C_2T_x$ MXene composite integrated with MOF-derived CuO components. This architecturally layered structure, composed of alternating MXene sheets and CuO NPs derived from MOF precursors, significantly augmented the effective surface area of the resultant MXene-CuO hybrid material. Song *et al.*[253] introduces the strategic combination of MnO_2/Mn_3O_4 derived from MOFs with MXene, leading to the construction of a multifunctional MnO_2/Mn_3O_4/MXene/Au NPs composite. The hierarchical architecture features 3D MnO_2/Mn_3O_4 microcuboids embedded with vertically oriented nanosheets, which, in synergistic combination with MXene-supported Au NPs, substantially improves both electrochemical characteristics and interfacial accessibility. This design achieves dual enhancement in signal transduction efficiency and biocompatibility through complementary material properties.

2.3.3. MOF-derived metal phosphide/MXene. Zong *et al.*[254] synthesized a novel MOFs-CoP@MXene composite *via* the self-assembly method. The MOFs-CoP component is easily deformable, and its heterostructure forms a hollow polyhedral structure that enhances the stability of the MOFs-CoP@MXene composite. Similarly, Liu and co-workers[255] successfully synthesized the hierarchical sandwich-like CoP-NC@$Ti_3C_2T_x$ composite through argon-protected *in situ* intercalation and phosphorylation of MOF@MXene precursors (Fig. 9a). Their approach involved the deposition of geometrically distorted ZIF-67 rhombic dodecahedrons onto $Ti_3C_2T_x$ substrates, creating a ZIF-67@$Ti_3C_2T_x$ architecture. Subsequent thermal treatment triggered ZIF-67 decomposition into 100–200 nm CoP-NC NPs. In a related methodology, Zong *et al.*[256] engineered Ti_2NT_x@MOF-CoP heterostructures by phosphate-functionalizing Ti_2NT_x@ZIF-67 assemblies. This protocol commenced with Ti_2NT_x MXene synthesis, followed by electrostatic-driven ZIF-67 integration and final phosphidation. Li and colleagues reported MXene@MOF-Co_2P nanocomposites through ZIF-67 templating, where nitrogen/carbon-doped Co_2P architectures were immobilized on bimetallic MXene matrices.[257] Building on their previous study, Wang and co-workers developed a simple procedure to prepare CoPC/CNTs@MXene absorbers by combining 0D/1D stratified CoPC/CNTs with MXene *via* electrostatic self-assembly.[258]

Ma *et al.*[259] employed a self-assembly strategy combined with *in situ* phosphorization to construct a porous core–shell CoP@NC nano-polyhedral composite system (CoP@NC/MXene), using 2D MXene nanosheets as a conductive substrate. The precursor framework was first formed *via* self-assembly, followed by a phosphorization process that simultaneously generated the CoP core and a NC shell. The incorporation of MXene enhanced charge transfer efficiency through its 2D conductive network and suppressed the pulverization of active materials. Cui *et al.*[260] focused on the integration of MOFs with 2D materials, synthesizing a layered porous material (graphene oxide (GO)/MXene@NiZrP) by *in situ* compositing UIO-66 with GO and MXene *via* hydrothermal and calcination methods. This approach leveraged the dual-substrate synergistic effects of GO and MXene to offer plentiful active sites and modulate interlayer spacing. During calcination, the MOF structure was transformed into metal phosphides while retaining high specific surface area and surface defect characteristics. Zhang *et al.*[261] further expanded the MOF-derived strategy for MXene composites by embedding Co-doped Cu_3P/NC octahedra (derived from MOF precursors) into MXene interlayers through an *in situ* growth method, forming a 3D@2D heterostructure (Co–Cu_3P/NC@MXene). This synthetic route not only modulated the electronic structure of Cu_3P *via* heterometal doping but also leveraged the 2D interlayer confinement effect of MXene to facilitate mass transport, thereby achieving dual optimization of hierarchical architecture and electronic properties.

2.3.4. MOF-derived metal selenide/MXene. Through a practical two-stage synthesis approach involving hydrothermal treatment and subsequent selenization at 400 °C in an argon environment, Hou *et al.* successfully fabricated multilayer $NiSe_2$–$CoSe_2$@C/$Ti_3C_2T_x$ composites. As depicted in Fig. 9b and c, the petal-like structure was disrupted following high-temperature selenization, resulting in the appearance of carbon-coated particles adhering to each other.[262] In 2022, Yang and co-workers achieved the fabrication of distinctive 2D hierarchical MXene@$CoSe_2$/Ni_3Se_4 nanosheets through an innovative template-assisted approach. This method encompassed the *in situ* growth of MOF on MXene substrates, followed by sequential ion exchange and controlled selenization processes. Fig. 9d presents the synthetic pathway for constructing these multilayered heterostructures. Morphological characterization (Fig. 9e and f) reveals a well-defined architecture in which $CoSe_2$/Ni_3Se_4 nanolayers uniformly adhere to both sides of the MXene substrates, forming a stable sandwich-like configuration.[263] More recently, Li *et al.* reported on the recent research development regarding the VSe_2–ZrO_2/C/MXene composite by a practical solvothermal method and *in situ* selenization process.[264] Additionally, Shi *et al.* synthesized the $CoSe_2$@C/MXene composite material by annealing a pre-prepared Co-MOF/MXene (mass ratio 10 : 1) with selenium powder at 650 °C in an Ar atmosphere for 3 h. The resulting $CoSe_2$ NPs were uniformly dispersed both on the surface and within the multi-heteroatom-doped carbon matrix, while the MXene nanosheets maintained their sheet structure within the composite material.[265] Wang *et al.* reported a series of hollow-structured ZnSe–CoSe composites (45@ZnSe–CoSe/S, 45@ZnSe–CoSe/P/S, and 45@ZnSe–CoSe/MXene/S) with distinct hollow

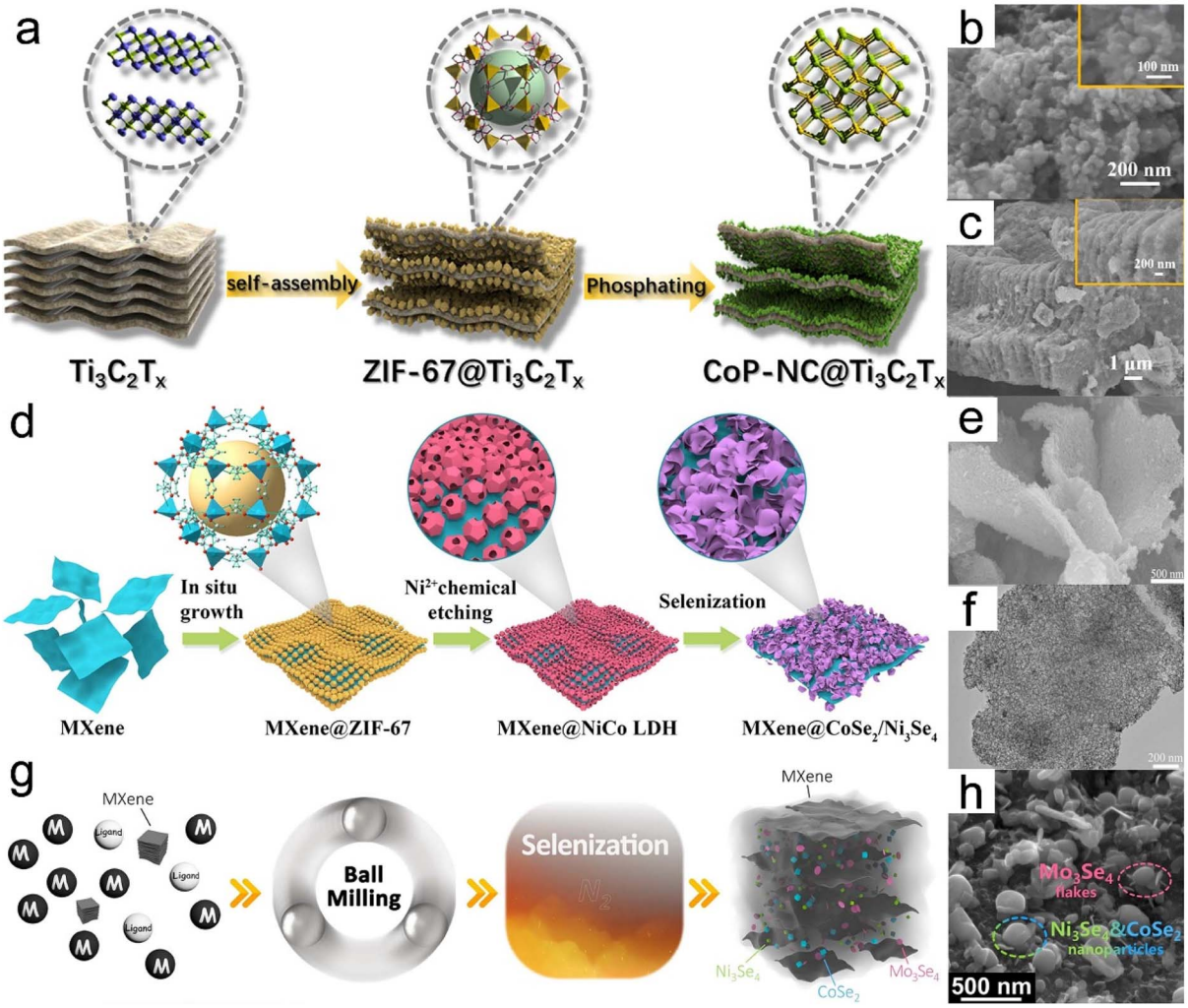

Fig. 9 (a) Formation approach of CoP-NC@$Ti_3C_2T_x$. SEM images of $NiSe_2$–$CoSe_2$@C (b) and $NiSe_2$–$CoSe_2$@C/$Ti_3C_2T_x$ (c). (d) Schematic view of formation for the hierarchical 2D MXene@$CoSe_2$/Ni_3Se_4 nanosheets. (e) SEM and (f) TEM images of MXene@$CoSe_2$/Ni_3Se_4 nanosheets. (g) Synthetic route of NCMS@C/MX. (h) SEM image of NCMS@C/MX. (a) Reproduced with permission.[255] Copyright 2021, Elsevier. (b and c) Reproduced with permission.[262] Copyright 2021, Elsevier. (d–f) Reproduced with permission.[263] Copyright 2022, Elsevier. (g and h) Reproduced with permission.[267] Copyright 2023, Wiley.

architectures, fabricated through a simple two-step synthesis method. This approach combined TA-assisted etching with subsequent selenization treatment of ZIF-8@ZIF-67.[266] Fig. 9g presents a schematic diagram outlining the synthesis procedure of MOFs/MXene-derived multi-metal selenides@C/MXene (NCMS@C/MX). Liang *et al.* achieved the preparation of NCMS@C/MX by first synthesizing MOF and exfoliating MXene, followed by further selenization of the selenides@C/MXene composite. The morphology of NCMS@C/MX composite is depicted in the SEM image (Fig. 9h), where Ni_3Se_4 and $CoSe_2$ NPs, as well as Mo_3Se_4 nanosheets, are uniformly distributed within the multi-heteroatom-doped carbon matrix.[267] Furthermore, the advancement of K-ion batteries (KIBs) faces challenges stemming from insufficient anode materials possessing optimal theoretical capacity, rapid K^+ transport characteristics, and environmental sustainability. To address this challenge, Hu *et al.* developed a MOF-templated synthetic route to fabricate ZnTe@C composites. Their strategy enabled homogeneous dispersion of ZnTe NPs within a conductive carbon framework, which was subsequently immobilized on MXene substrates. Crucially, electronic structure modulation of ZnTe enhanced K^+ adsorption kinetics, while their pioneering work elucidated the conversion mechanism: yZnTe + xK$^+$ + xe^- → yZn + K_xTe_y, establishing ZnTe as a promising KIB anode.[268] Jeong Ho Na and colleagues successfully prepared 3D MXene microspheres *via* spray-drying assembly. This configuration effectively mitigates MXene sheet restacking while encapsulating MOF-derived ZnSe@NC heterostructures, demonstrating enhanced electrode stability.[269] Vallem *et al.*[270] proposed a rational design of a high-efficiency selenium host material, Fe-CNT/TiO_2, based on a tailored composite nanostructure. The synthetic protocol involved the initial construction of a MOF-MXene composite, followed by CNT surface decoration, and final high-temperature sintering. The key innovation lies in

utilizing the MOF-derived Fe-CNT structure to provide both conductive networks and catalytic active sites, while the MXene transforms into a TiO_2 phase through sintering, forming a hierarchical porous architecture.

2.3.5. MOF-derived metal sulfide/MXene. Metal sulfides are regarded as highly promising nanomaterials. However, their practical applications are hindered by intrinsic limitations such as poor conductivity and significant volume expansion during electrochemical processes. To address these issues, metal sulfides derived from MOF offer a viable solution by enhancing electrical conductivity and mitigating volume expansion. Moreover, integrating MOF-derived metal sulfides to MXene conductive substrates can further improve their conductivity.[271] In 2018, Zou *et al.* synthesized a unique porous Ni–Co mixed metal sulfide (NiCoS), which was grown on MXene derived from ZIF-67/MXene. The preparation process for NiCoS/MXene is depicted in Fig. 10a.[272] Subsequently, Wei *et al.* designed and constructed a MOF-derived $NiCo_2S_4$ attached to MXene to form a $NiCo_2S_4$@MXene composite. The MOF-derived $NiCo_2S_4$ promotes the surface hydroxylation of MXene, facilitating the adsorption of metal ions and inducing sulfur vacancy formation. In addition, MXene provides a high specific surface area, enabling rapid charge carrier transport. Through synergistic interactions between components, the resulting composites have significantly enhanced nonlinear optical and electrochemical properties.[273] In Fig. 10b, Li *et al.* addressed the primary limitations of metal sulfide materials, namely slow kinetics and severe volume expansion, *via* utilizing poly(methyl methacrylate) spheres as sacrificial template to form MXene nanosheets. Subsequently, through a multi-step procedure involving *in situ* growth, carbonization, and sulfurization processes, they successfully synthesized MXene@CoS_2/NC composite materials comprising MOF-derived CoS_2/NC integrated with MXene nanosheets.[274] More recently, Adil *et al.* developed an inventive method for creating the MXene cobalt sulfide (MXene-CoS) composite material. A cost-effective Co-MOF was sulfided and directly integrated with an MXene film *via* a binder-free *in situ* growth strategy on NF, resulting in the formation of MXene-CoS/NF. This architecture exhibits favorable structural characteristics, including increased porosity, abundant active sites, enlarged interfacial area, and superior electrocatalytic activity.[275] Additionally, Farooq *et al.*[276] established a synthetic strategy for preparing bifunctional electrocatalyst CoS@C/MXene through high-temperature vulcanization. The process involves first combining ZIF-67 with MXene to form a precursor hybrid material, followed by high-temperature vulcanization treatment in a H_2S atmosphere. For instance, the CoS@C/MXene underwent vulcanization at 800 °C, which transformed the cobalt species in ZIF-67 into CoS while simultaneously carbonizing them into a carbon layer structure encapsulating CoS. This structure tightly integrated with the MXene, ultimately forming the CoS@C/MXene nanocomposite.

2.3.6. MOF-derived metal hydroxide/MXene. In recent years, the synthesis strategies of MOF-derived metal hydroxides/MXene composite have demonstrated unique advantages in structural engineering. Hu *et al.*[277] innovatively constructed CoFe LDH/MXene composite structure through an "etching-coprecipitation" post-treatment method: by utilizing MXene as a multifunctional support, they anchored MOF precursors and

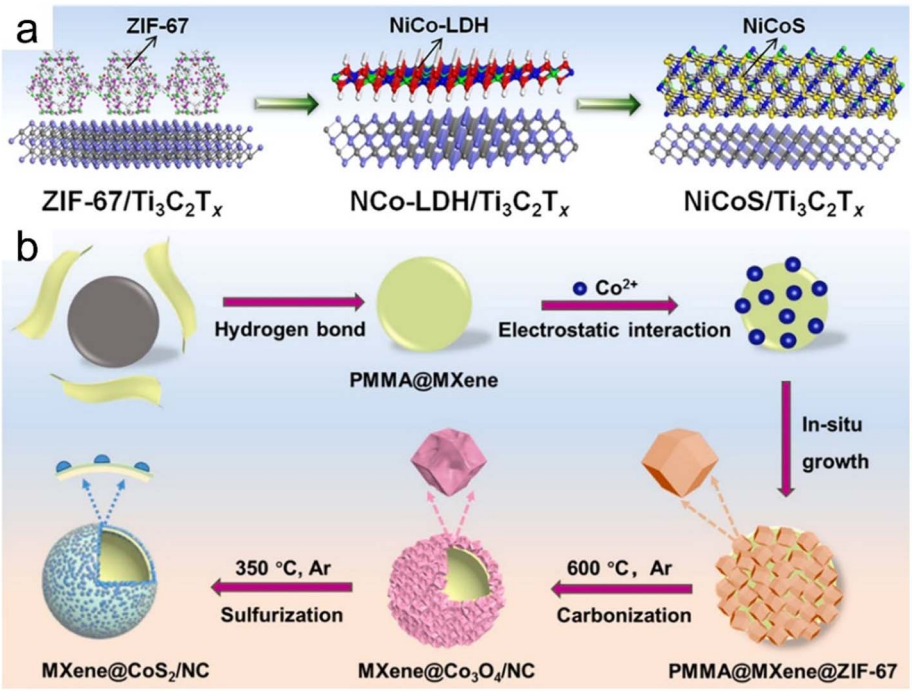

Fig. 10 (a) The preparation process of NiCoS/MXene. (b) Schematic representation of the synthesis of MXene@CoS_2/NC. (a) Reproduced with permission.[272] Copyright 2018, American Chemical Society. (b) Reproduced with permission.[274] Copyright 2022, Elsevier.

achieved controlled etching to release metal ions, thereby inducing the *in situ* coprecipitation growth of LDH. This interfacial engineering not only optimized the charge transport pathways but also regulated the intermediate adsorption strength at active sites through strong electronic interactions between CoFe LDH and MXene. In contrast, Kasinathan *et al.*[278] adopted a "charge-directed self-assembly" strategy, leveraging electrostatic interactions to integrate chitosan (CS)-modified

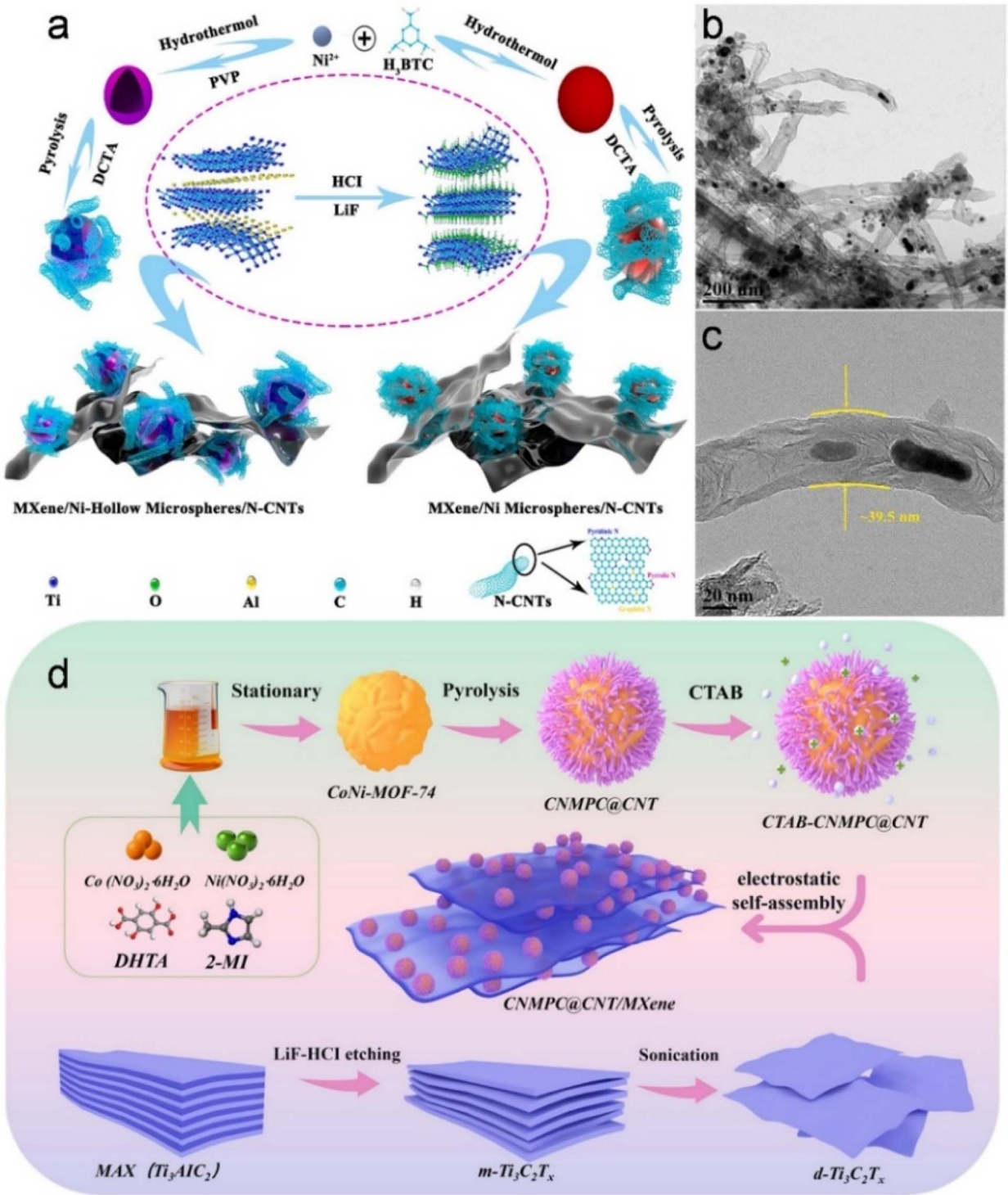

Fig. 11 (a) Schematic illustration of the synthesis of MXene/Ni/N-CNTs. (b and c) TEM images different magnifications of MXene/Ni/N-CNTs nanocomposites. (d) Schematic illustration of the fabrication of CoNi-MPC@CNTs/MXene. (a–c) Reproduced with permission.[282] Copyright 2021, Elsevier. (d) Reproduced with permission.[284] Copyright 2024, Elsevier.

MXene nanosheets with cobalt-tungsten LDH, resulting in the formation of a CS/MXene@LDH hybrid structure. The self-assembly process, driven by the complementary surface charges of negatively charged MXene and positively charged CoW LDH, enabled uniform dispersion and robust integration of the nanoscale components. Although these two studies differ in application fields, both highlight the shared philosophy of precise structural regulation and functional integration in composite system fabrication through interfacial synergistic design with MXene, employing distinct pathways of chemical etching reconstruction and physical electrostatic adsorption respectively.

2.3.7. Carbon-based material from MOF/MXene-based materials. Synthesis methods of MOF-derived carbon/MXene-based materials have demonstrated diversified innovative pathways in recent years.[279–281] To advance the development of high-performance microwave absorption materials, Zhou *et al.*[282] developed an innovative approach by integrating 1D CNTs derived from Ni-MOFs (exhibiting hollow solid microsphere architecture) with 2D MXene to establish an interconnected 3D conductive framework (Fig. 11a–c). In addition, Gu *et al.* reported a MXene-supported MOF-derived Fe–N–C catalyst (Fe–N_x/N/MXene), which exhibits good oxygen reduction reaction (ORR) activity and long-term stability.[283] To achieve optimal electromagnetic wave (EMW) absorption capability, Wu *et al.* synthesized a Co–Ni-MOF-derived waxberry-like magnetic porous carbon (CoNi-MPC)@CNTs/MXene hybrid (CoNi-MPC@CNTs/MXene) through a simple solution precipitation, heat treatment, and electrostatic self-assembly strategy (Fig. 11d).[284]

In 2018, in order to further enhance the electromagnetic attenuation ability, Liao and co-workers[285] prepared laminated Co/TiO_2–C hybrids through thermal treatment of $Ti_3C_2T_x$/Co-MOF, integrating them with MXene-derived TiO_2–C laminates (Fig. 12a–d). Building upon this foundation, Deng *et al.*[286] subsequently engineered innovative sandwich-structured 2D nanocomposites containing Fe & TiO_2 NPs embedded in carbon matrices, utilizing MXene-MOF hybrid architectures as synthetic platforms. As shown in Fig. 12e–h, Fe-MOFs were initially transformed into Fe_3O_4/PC, and subsequently formed carbon-coated Fe NPs (Fe@C) under a reducing atmosphere. With increasing pyrolysis temperature, both TiO_2 and Fe particles exhibited progressive growth and pronounced aggregation. Recently, Wang and colleagues[287] successfully prepared 3D spherical Ni/TiO_2/C microspheres alongside hierarchically layered Ni/TiO_2/C nanocomposites through an innovative

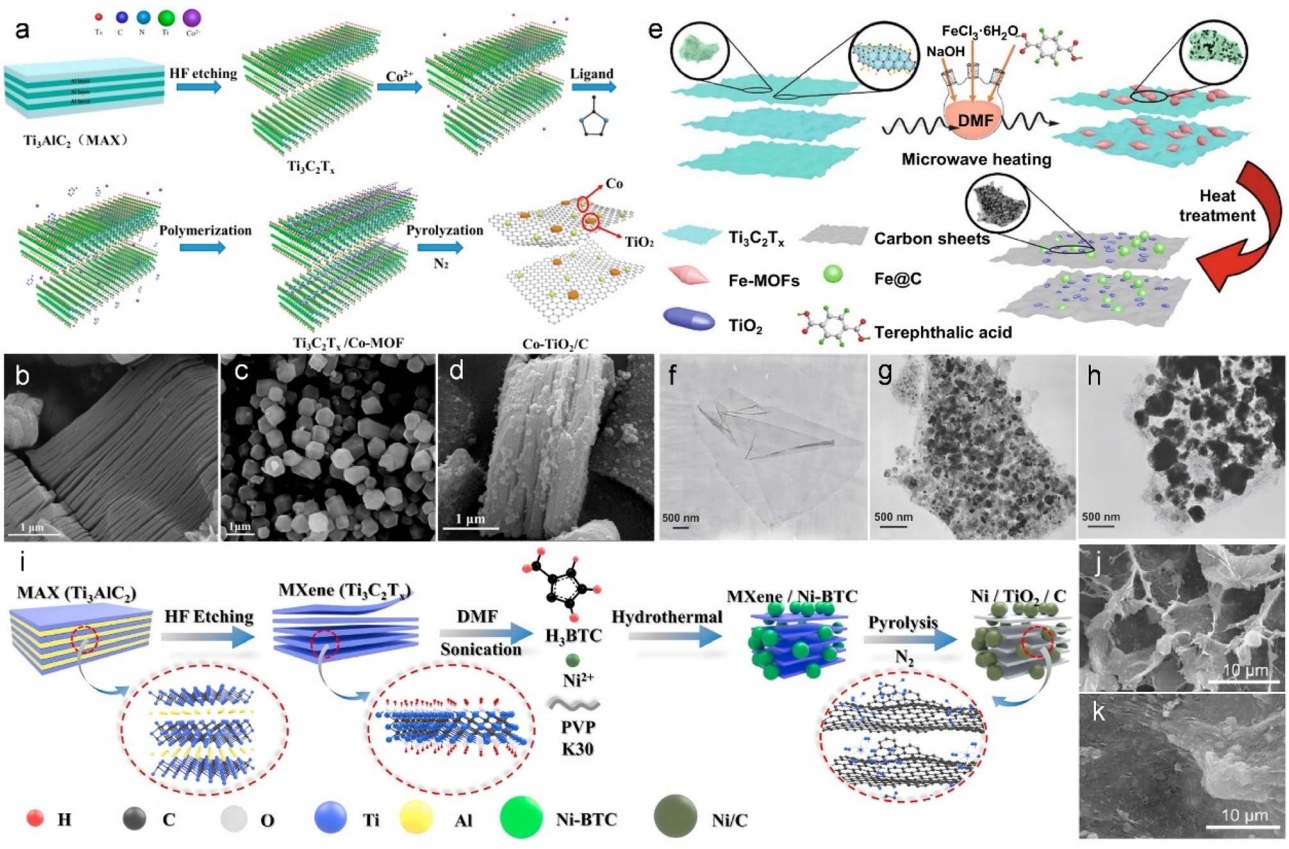

Fig. 12 (a) Illustration of the preparation of Co/TiO_2–C. (b–d) SEM images of $Ti_3C_2T_x$, Co-MOF, and Co/TiO_2–C composites. (e) Preparation of Fe & TiO_2@C. (f–h) TEM images of $Ti_3C_2T_x$, Fe & TiO_2@C (700 °C), and Fe & TiO_2@C (800 °C). (i) Illustration of the fabrication process of Ni/TiO_2/C nanocomposites. (j and k) SEM images of ZIF-67/Nb_2CT_x/cellulose aerogel and Co/Nb_2CT_x/cellulose CA. (a–d) Reproduced with permission.[285] Copyright 2018, American Chemical Society. (e–h) Reproduced with permission.[286] Copyright 2020, Springer. (i) Reproduced with permission.[287] Copyright 2022, Elsevier. (j and k) Reproduced with permission.[288] Copyright 2023, American Chemical Society.

synthesis approach. Utilizing Ni-BTC and $Ti_3C_2T_x$ MXene as precursor materials, the researchers implemented an *in situ* solvothermal self-assembly strategy coupled with controlled thermal annealing. The resulting nanostructures incorporate precisely arranged 2D carbon matrices hosting uniformly dispersed TiO_2 NPs (Fig. 12i). Cui *et al.*[288] employed biomass-derived bamboo as carbon source to construct a 3D interconnected network through porous structure engineering strategy. Briefly, bamboo cellulose was assembled with few-layer Nb_2CT_x MXene to form a 3D aerogel framework. Subsequently, ZIF-67 precursors were uniformly anchored *via* chemical deposition, and ultimately Co NPs/Nb_2CT_x/CA composite was obtained through high-temperature pyrolysis (Fig. 12j and k). This architecture establishes a conductive network through synergistic interactions between the biomass-derived carbon matrix and MXene components, while simultaneously optimizing impedance matching *via* interfacial polarization and magnetic loss contributions from MOF-derived magnetic nanoparticles. Zheng *et al.*[289] proposed a biomimetic structural design strategy. Their methodology employed solvothermal synthesis to realize controlled *in situ* crystallization of bimetallic CoNi-MOF within MXene layers, which subsequently underwent pyrolysis conversion into magnetically responsive carbon hybrids (CoNi@C). This transformation process yielded a hierarchically organized structure mimicking marine coral morphology. This strategy effectively alleviates MXene stacking through interlayer-embedded MOF-derived carbon nanorods, while introducing porous heterogeneous interfaces to enhance dielectric-magnetic coupling effects. Furthermore, Guo *et al.*[290] innovatively addressed limitations associated with single-layer architectures through a sequential vacuum-assisted filtration strategy. Their Janus architecture combined two functionally distinct components: a magnetic CNF composite derived from CoNi-MOF-74 served as the electromagnetic absorption layer, and MXene/CNF acting as the reflective layer. The integrated system achieved robust interfacial bonding *via* hydrogen bonding interactions between constituent layers. This dual-layer architecture not only optimizes electromagnetic dissipation pathways through "absorption-reflection-reabsorption" mechanism, but also enhances multifunctionality by harnessing MXene's plasmonic effects and the mechanical reinforcement properties of CNF.

2.3.8 Summary. The synthesis of MOF derivative/MXene composites, as detailed in the previous sections, is fundamentally different from that of pure MOF/MXene or MOF composite/MXene materials. The defining characteristic of this type of material is the essential role of post-synthetic thermal treatment (*e.g.*, calcination, pyrolysis, sintering) in transforming the MOF structure into the final derivative while preserving the structural integrity of the MXene substrate.

A critical analysis reveals that the synthesis strategy is a multi-step process: firstly, a precursor composite is formed by integrating the MOF with MXene, and secondly, this composite undergoes a controlled thermal transformation to generate the derivative. The choice of the initial integration method for the precursor is diverse. *In situ* growth is a common approach, used to construct MOF@MXene that are subsequently converted into metal phosphides[261] or metal sulfides.[275] Electrostatic self-assembly is also highly effective for creating the initial hybrid, as demonstrated by the formation of MXene@Co-CZIF and MXene@Ni-CZIF composites, which were then pyrolyzed to form metal/carbon hybrids.[233] Solvothermal methods are employed to create layered porous materials, such as GO/MXene@NiZrP, which are then transformed into phosphides *via* calcination.[260]

The thermal treatment step is the most critical and challenging aspect. The temperature, atmosphere (*e.g.*, N_2, Ar), and heating rate must be meticulously controlled. The objective is to completely decompose the MOF into the desired derivative (*e.g.*, metal, oxide, phosphide, sulfide), while minimizing the oxidation and degradation of the MXene. For instance, the successful synthesis of MOF-derived metal phosphides,[260,261] sulfides,[275,276] and hydroxides[277] depends on finding this delicate balance. The use of MXene as a conductive and mechanically robust substrate not only provides a support for MOF precursors but also plays a crucial role in stabilizing the derivative phases and preventing its aggregation during the high-temperature process.

In conclusion, the synthesis of MOF derivative/MXene composites is a complex process, with the core being the integration of MOF precursors with MXene, followed by precisely controlled thermal transformation. The success of this strategy depends on the synergy between a well-designed precursor architecture and optimized thermal conditions to achieve high-performance hybrid materials.

3. Applications

The versatility of MOF/MXene-based materials is illustrated in Scheme 3, highlighting their broad applicability in batteries,[291–293] SCs,[120,245] sensors,[294–296] catalysts,[297–299] and absorption.[300–302] In advanced battery systems, MOF compounds serve bifunctional roles. These porous materials serve not only as high-performance anode components in lithium-ion batteries (LIBs) due to their exceptional specific capacity and outstanding energy storage properties, but also show promise as cathode materials by maintaining stable redox activity and effectively mitigating detrimental shuttling effects.[303] For SC applications, MOF/MXene composites demonstrate ultra-high specific capacitance and excellent reversibility, rendering them strong candidates as binder-free electrode materials.[105,196] Furthermore, MOF/MXene composites are extensively utilized in multiple sensing applications, showcasing remarkable adaptability. For example, efficient sensors for arsenate detection in electrochemistry, self-powered biomotion and tactile sensing applications, electrochemically sensitive sensors for H_2O_2 detection, and as organoid gas sensors.[129,133,216] In summary, these sensors demonstrate outstanding selectivity, consistent reproducibility, and durable operational stability, attributes that collectively contribute to technological advancements in societal infrastructure. The unique combination of adjustable surface properties, architectural versatility, and expansive active interfaces has positioned MOF/MXene hybrid systems as a focal point in advanced materials

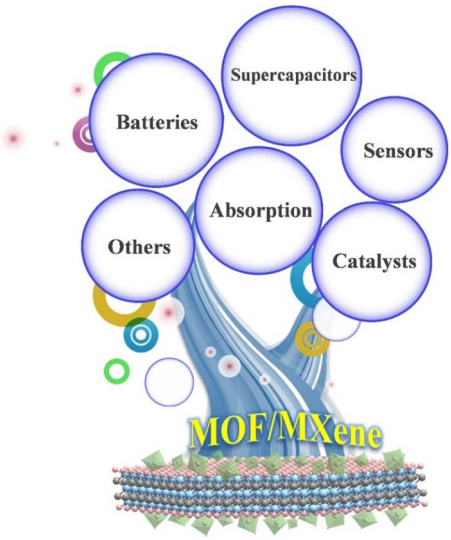

Scheme 3 Application of MOF/MXene-based materials.

research. These attributes make it a promising catalyst material with high electrical conductivity, including oxygen evolution reaction (OER),[304] hydrogen evolution reaction (HER),[305] ORR,[306] and photocatalysts.[307,308]

In the field of EMW absorption, MOF/MXene-based materials demonstrate exceptional EMW attenuation capabilities, significantly enhancing absorption efficiency and exhibiting great potential for next-generation intelligent electromagnetic shielding systems.[290] Due to their lightweight nature and broad absorption bandwidth, these materials can address a range of electromagnetic pollution issues in daily life. High-performance absorbing materials can markedly enhance the absorption performance of EMW and positively impact microwave absorption performance, showcasing an excellent absorption bandwidth.[286] This suggests that MOF/MXene-based materials play a significant role in societal development. MOF/MXene-based materials can serve as highly effective flame retardants, enhancing fire safety while also possessing adsorption and sterilization effects.[141,172] These hybrid systems show particular promise for dual applications in agricultural engineering (particularly paddy field management) and biomedical wound care, with documented therapeutic implementations already contributing to enhanced healthcare outcomes and quality-of-life improvements.[309]

3.1. Batteries

MOF materials demonstrate significant potential as battery electrode materials, offering advantages including numerous active sites, hierarchically porous architectures, minimized ion transport distances, and tunable chemical compositions.[310] However, their relatively low electronic conductivity remains a limitation. Therefore, developing innovative electrode architectures with enhanced energy storage performance and mechanical robustness represents a vital research direction. The research findings on MOF/MXene-based materials for battery over the past few years are presented in Table 1.

Within the realm of MOF/MXene composites, both 3D Ti_3C_2 MXene/NiCo-MOF composite films[182] and 2D MXene/NiCo MOF heterostructures[185] have been identified as highly effective anodes for high-performance LIBs. The optimized MXene/NiCo-MOF electrode showcases remarkable electrochemical characteristics, delivering a reversible capacity of 402 mA h g^{-1} at 0.1 A g^{-1} with sustained rate capability (256 mA h g^{-1} at 1 A g^{-1})

Table 1 MOF/MXene-based materials for batteries, including LIBs, LSBs and others

MOF/MXene-based materials	Type of batteries	Reversible capacity/ current density	Cycling performance (capacitance retention, cycle, current density)	Ref.
Ti_3C_2 MXene@NiCo-MOF	LIBs	402 mA h g^{-1}/0.1 A g^{-1}	85.7%, 400, 1 A g^{-1}	182
MXene@NiCo-MOF	LIBs	637 mA h g^{-1}/0.2 A g^{-1}	304 mA h g^{-1}, 800, 1 A g^{-1}	185
Ni-MOF@MXene	LIBs	980 mA h g^{-1}/0.2 A g^{-1}	80%, 5000, 5 A g^{-1}	311
PE-ZIF-8@MXene	LIBs	121 mA h g^{-1}/5C	89.6%, 500, 1C	221
MOFs-CoP@MXene	LIBs	706.5 mA h g^{-1}/0.2 A g^{-1}	585.8 mA h g^{-1}, 1000, 0.5 A g^{-1}	254
VSe_2–ZrO_2@C@MXene	LIBs	612.2 mA h g^{-1}/0.1 A g^{-1}	430 mA h g^{-1}, 1000, 1 A g^{-1}	264
$CoSe_2$/ZnSe@MXene	LIBs	536.7 mA h g^{-1}/1 A g^{-1}	63.1%, 2000, 1 A g^{-1}	310
Zn_xIn_yS/MXene	LIBs	1300 mA h g^{-1}/0.5 A g^{-1}	1097 mA h g^{-1}, 1000, 1 A g^{-1}	271
Co_3O_4@NGC/MXene	LIBs	327 mA h g^{-1}/50 A g^{-1}	830 mA h g^{-1}, 500, 1 A g^{-1}	248
Zr-MOF@$Ti_3C_2T_x$	LSBs	1017 mA h g^{-1}/0.1C	46%, 1000, 1C	177
$Ti_3C_2T_x$-UIO-66-NH_2	LSBs	840 mA h g^{-1}/0.5C	38.5%, 1500, 1C	293
$ZnCo_2O_4$@Ti_3C_2/S	LSBs	547 mA h g^{-1}/0.2C	26.8%, 400, 0.5C	244
45@ZnSe–CoSe/MXene	LSBs	478 mA h g^{-1}/0.2C	387.2 mA h g^{-1}, 400, 0.5C	266
FeCo@MXene	LSBs	703 mA h g^{-1}/4C	58%, 1000, 1C	231
ZnTe@C/$Ti_3C_2T_x$	KIBs	408 mA h g^{-1}/0.1 A g^{-1}	230.2 mA h g^{-1}, 3500, 1 A g^{-1}	268
MXene/ZnSe@NC	KIBs	180 mA h g^{-1}/0.5 A g^{-1}	238 mA h g^{-1}, 1000, 0.5 A g^{-1}	269
Co_3C/MXene@C	KIBs	236 mA h g^{-1}/0.2 A g^{-1}	129.3 mA h g^{-1}, 500, 0.5 A g^{-1}	312
CoP-NC@$Ti_3C_2T_x$	SIBs	142.3 mA h g^{-1}/0.05 A g^{-1}	101.6 mA h g^{-1}, 500, 0.5 A g^{-1}	255
CoP@N–C/MXene	SIBs	658.6 mA h g^{-1}/0.05 A g^{-1}	61 mA h g^{-1}, 500, 2 A g^{-1}	259
MXene@CoS_2/NC	SIBs	620 mA h g^{-1}/0.2 A g^{-1}	87.5%, 5000, 5 A g^{-1}	274
$CoSe_2$@C/MXene	SIBs	402.9 mA h g^{-1}/0.1 A g^{-1}	259.8 mA h g^{-1}, 1800, 1 A g^{-1}	265
$CoFe_2O_4$@carbon@MXene	SIBs	416 mA h g^{-1}/0.1 A g^{-1}	130, 1000, 1 A g^{-1}	240

through 300 cycles. These enhancements stem from synergistic effects including three-dimensional porous networks, expanded surface area, accelerated electron transport kinetics, and optimized Li^+ diffusion pathways. Long-term cycling stability data (Fig. 13a) reveal 85.7% capacity retention after 400 cycles at 1 A g^{-1}, confirming structural resilience under high current operation. Complementary cyclic voltammetry (CV) analysis conducted at various scan rates (Fig. 13b) further confirms the superior electrochemical behavior of these composites.[182] Electrochemical characterization of the $Ti_3C_2T_x$/NiCo MOF heterostructure displays progressive capacity enhancement during cycling (Fig. 13c), a phenomenon associated with gradual electrode activation and dynamic evolution of a functional gel-like interfacial layer. The material's exceptional rate adaptability, as shown in Fig. 13d, combined with its distinctive voltage profiles across cycling stages, highlights the advantages of combining conductive MXene substrates with redox-active bimetallic MOF structure (Fig. 13e).[185] Notably, the MOF@MXene heterostructure anode developed by Sun *et al.* exhibits remarkable electrochemical performance, maintaining 80% capacity retention over 5000 cycles at 5A g^{-1}, a significant improvement compared to individual MXene and MOF components. Li^+ kinetics were investigated *via* CV measurements across scan rates ranging from 0.1 to 1 mV s^{-1} (Fig. 13f), with long-term cycling stability at high current density is illustrated in Fig. 13g. Structural analysis in Fig. 13h identifies two distinct Li^+ adsorption sites (labeled 1 and 2) in the pure NF-MOF. Overall, this hybrid architecture demonstrates enhanced Li storage capabilities and superior rate performance as LIB anodes, exceeding the electrochemical characteristics of both constituent materials when used separately.[311]

Furthermore, a novel polymer composite electrolyte reinforced with ZIF-8@MXene nanosheets (PE-ZIF-8@MXene) was developed by Zhao *et al.* When implemented in symmetric lithium battery configurations, the PE-ZIF-8@MXene enabled stable operation for 2000 h at 0.5 mA cm^{-2}. Electrochemical performance evaluation revealed that Li|PE-ZIF-8@MXene|Li batteries maintained 89.6% of their initial capacity through 500 cycles (Fig. 14c). Comparative analysis with conventional PE demonstrated the modified electrolyte's superior voltage hysteresis characteristics across varying current densities (Fig. 14a). Current-dependent polarization effects were observed

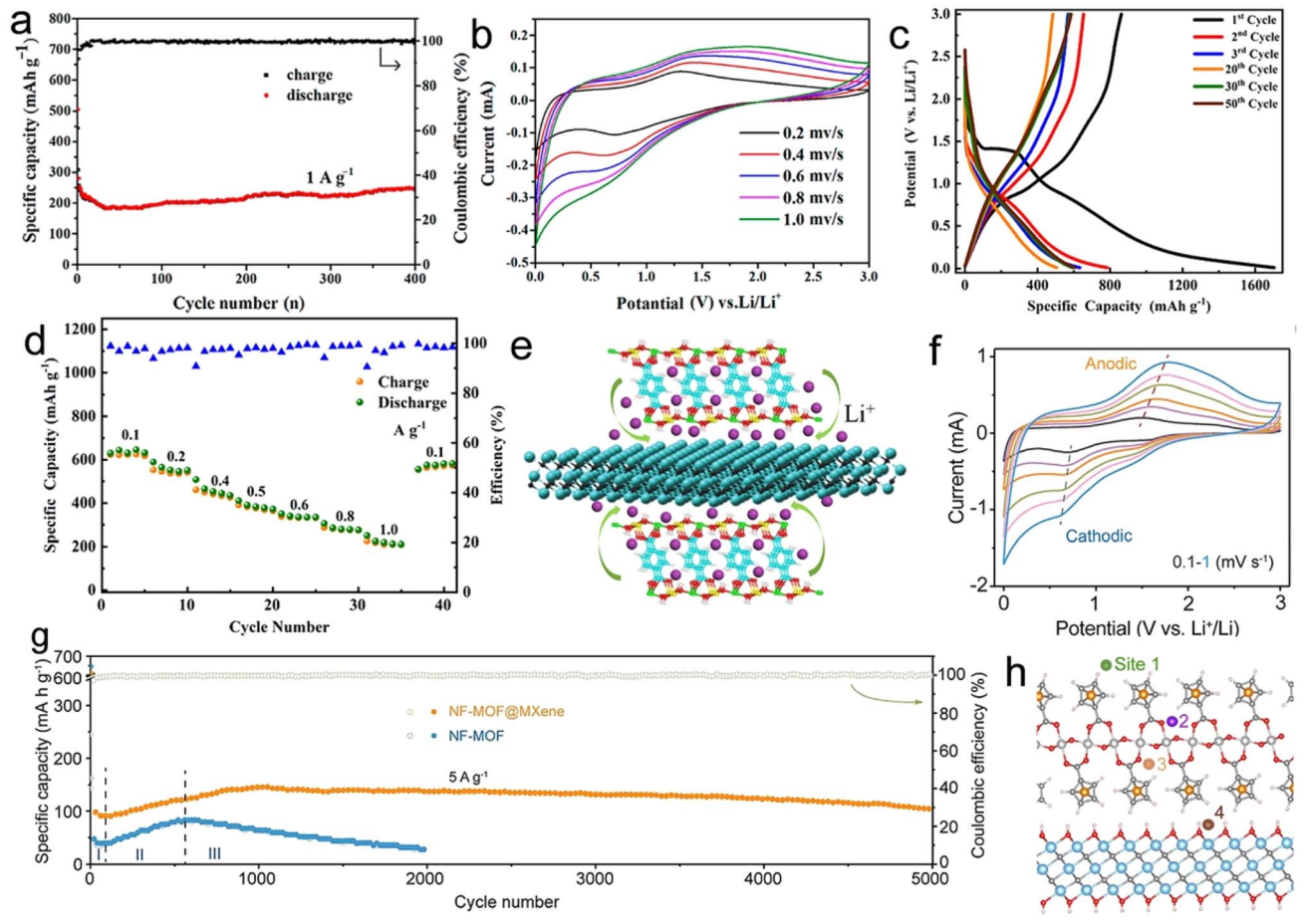

Fig. 13 (a) Cycle performance of MXene/NiCo-MOF at 1 A g^{-1}. (b) CV curves of the MXene/NiCo-MOF at different scan rates. (c) The discharging/charging curves of the $Ti_3C_2T_x$/NiCo-MOF electrode at 0.2 A g^{-1}. (d) Rate performance of the $Ti_3C_2T_x$/NiCo-MOF. (e) Illustration of the Li^+ intercalation of the MXene/NiCo-MOF heterostructure. (f) CV curves of NF-MOF@MXene at different scan rates. (g) Cycling performance at 5 A g^{-1}. (h) Lithium adsorbed at different sites. (a and b) Reproduced with permission.[182] Copyright 2020, Molecular Diversity Preservation International. (c–e) Reproduced with permission.[185] Copyright 2022, Elsevier. (f–h) Reproduced with permission.[311] Copyright 2022, Elsevier.

in the voltage–capacity profiles, with minimal increases noted when scaling current density from 0.5C to 2C (Fig. 14b).[221]

In the development of MOF derivative@MXene composites, Zong *et al.* synthesized an innovative MOFs-CoP@MXene hybrid through structural engineering. When employed as a LIB anode, this composite demonstrated exceptional cycling durability. As a cathode material for lithium–sulfur batteries (LSBs), it exhibited dual functionality: stable sulfur redox kinetics and significant mitigation of polysulfide shuttle phenomena through chemical confinement. Electrochemical characterization revealed distinct redox peaks in CV profiles (1.5–3.0 V, 0.1 mV s^{-1}), with the MOFs-CoP@MXene/S configuration showing enhanced cathodic activity evidenced by dual reduction peaks at 2.02 and 2.37 V, compared to the MOFs-CoP/S counterpart (Fig. 14d). The initial charge and discharge capacities of the MOFs-CoP@MXene/S were 1138.8 mA h g^{-1} at 0.2C (Fig. 14f). Fig. 14g presents the inherent mechanism by which MOFs-CoP@MXene/S inhibits the sulfide shuttle effect, thereby exerting its catalytic potential.[254] A MXene-based composite integrating VSe_2–ZrO_2 and carbon components (VSe_2–ZrO_2/C/MXene) was developed by Li and co-workers as advanced LIB anode material. This engineered material exhibited enhanced electrochemical characteristics, initially displaying capacity fluctuation before achieving remarkable improvement from 461.2 to 1238.5 mA h g^{-1} at 100 mA g^{-1}. Notably, the composite exhibited exceptional durability with

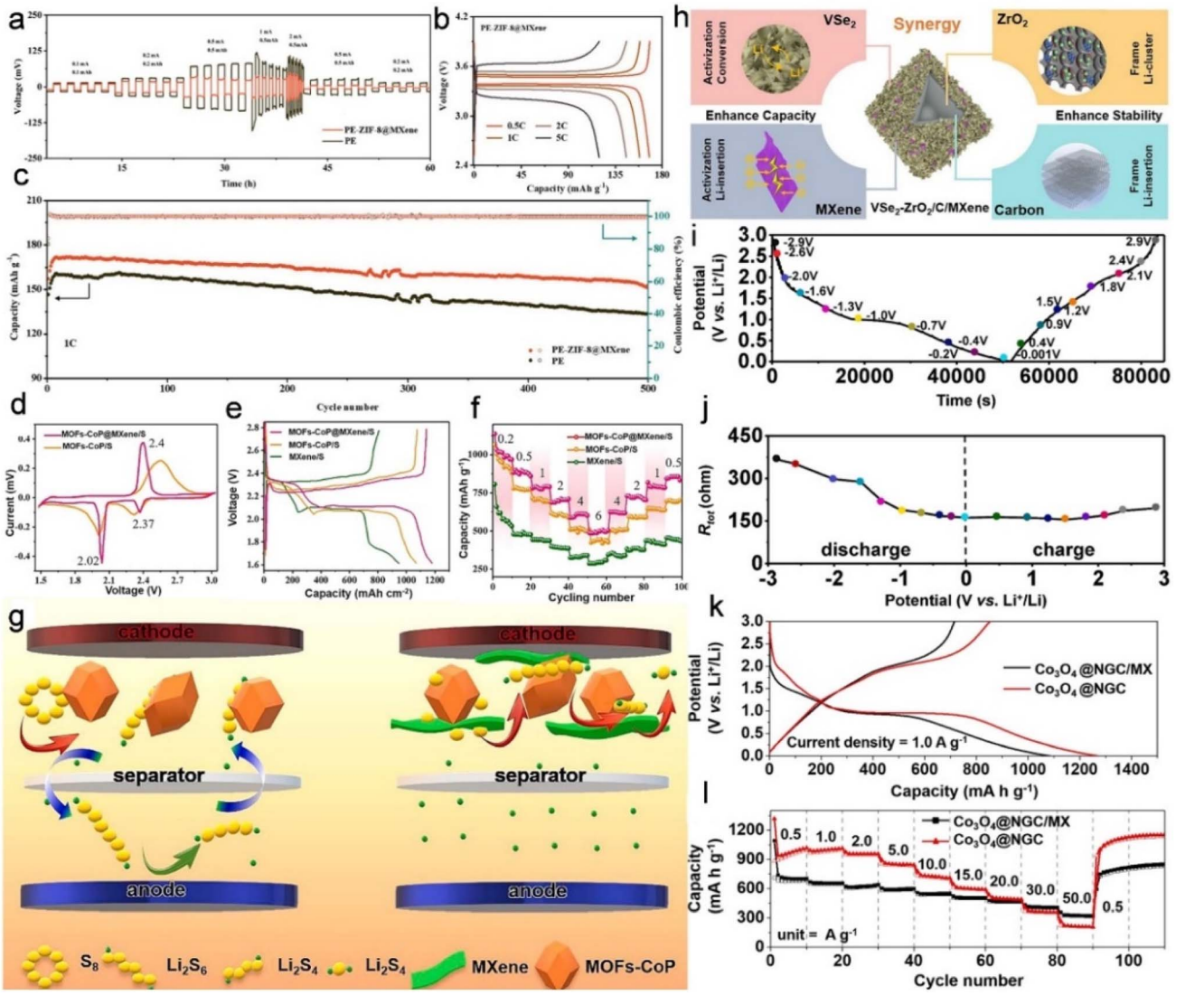

Fig. 14 (a) Rate performances of symmetric batteries with PE-ZIF-8@MXene and PE. (b) Concentrated voltage–capacity curves of PE-ZIF-8@MXene. (c) Cycling performance of PE-ZIF-8@MXene and PE. (d) CV curves of MOFs-CoP/S and MOFs-CoP@MXene/S. (e) Discharge–charge curves of MOFs-CoP@MXene. (f) Rate capability of MXene/S, MOFs-CoP/S and MOFs-CoP@MXene/S. (g) Schematic illustration of the inhibition mechanism of MOFs-CoP/S and MOFs-CoP@MXene/S. (h) Schematic of VSe_2–ZrO_2/C/MXene for the Li-ion storage mechanism. (i) Potential *vs.* time curve and (j) graph for the change of R_{tot} values at specific potential levels of Co_3O_4@NGC/MXene electrode for LIBs during the initial cycling. (k) The initial profile curves and (l) rate performance of Co_3O_4@NGC and Co_3O_4@NGC/MXene electrodes for LIBs. (a–c) Reproduced with permission.[221] Copyright 2022, Elsevier. (d–g) Reproduced with permission.[254] Copyright 2021, Elsevier. (h) Reproduced with permission.[264] Copyright 2023, Royal Society of Chemistry. (i–l) Reproduced with permission.[248] Copyright 2021, Elsevier.

430 mA h g^{-1} retention after 1000 cycles under1.0 A g^{-1}, confirming its structural resilience. The underlying charge storage mechanism is visually elucidated in the corresponding schematic diagram (Fig. 14h).[264] Recent studies by Oh *et al.* have identified the Co_3O_4@NGC/MXene hybrid as a promising LIBs anode material, demonstrating remarkable energy storage characteristics. The composite maintained 830 mA h g^{-1} after 500 cycles at 1.0 A g^{-1}, along with superior rate performance delivering 327 mA h g^{-1} at 50.0 A g^{-1}. The electrochemical behavior analysis reveals: Fig. 14i quantifies cycle endurance across different voltage windows, while Fig. 14j tracks the evolution of total resistance (R_{tot}) during initial battery operation. Comparative charge–discharge curves of Co_3O_4@NGC and Co_3O_4@NGC/MXene electrodes at 1.0 A g^{-1} are presented in Fig. 14k. Both configurations showed stable long-term cyclability, sustaining performance over 500 cycles as evidenced in Fig. 14l.[248]

LSBs have garnered significant attention as a promising rechargeable battery.[313] Wen *et al.* initially synthesized the 3D hierarchical Zr-MOF/$Ti_3C_2T_x$ nanocomposite, which displayed a substantial discharge/charge capacity of 801 mA h g^{-1} (Fig. 15b) at 1C and excellent cycling properties. Fig. 15c illustrates the long-term cycling performance of the Zr-MOF/$Ti_3C_2T_x$ composite over 1000 cycles at 1C rate. Fig. 15a depicts the working mechanism of the Zr-MOF/$Ti_3C_2T_x$/S composite in LSBs.[177] The superior architecture of the Zr-MOF/$Ti_3C_2T_x$ nanocomposites significantly enhances the electronic conductivity and charge transfer kinetics of the entire cathode, accelerates the redox conversion rate of chemisorbed polysulfide, and effectively protects the lithium anode from contamination. Building upon previous advancements, Wei and co-workers further engineered a $ZnCo_2O_4$@Ti_3C_2/S composite serving as an effective sulfur host material for LSBs. This innovative configuration achieved remarkable electrochemical metrics, including a primary discharge capacity of 1283.9 mA h g^{-1} and an exceptional initial coulombic efficiency of 98.7% under 0.1C. The system's electrochemical durability was further validated through extended cycling evaluations at 0.5C, with

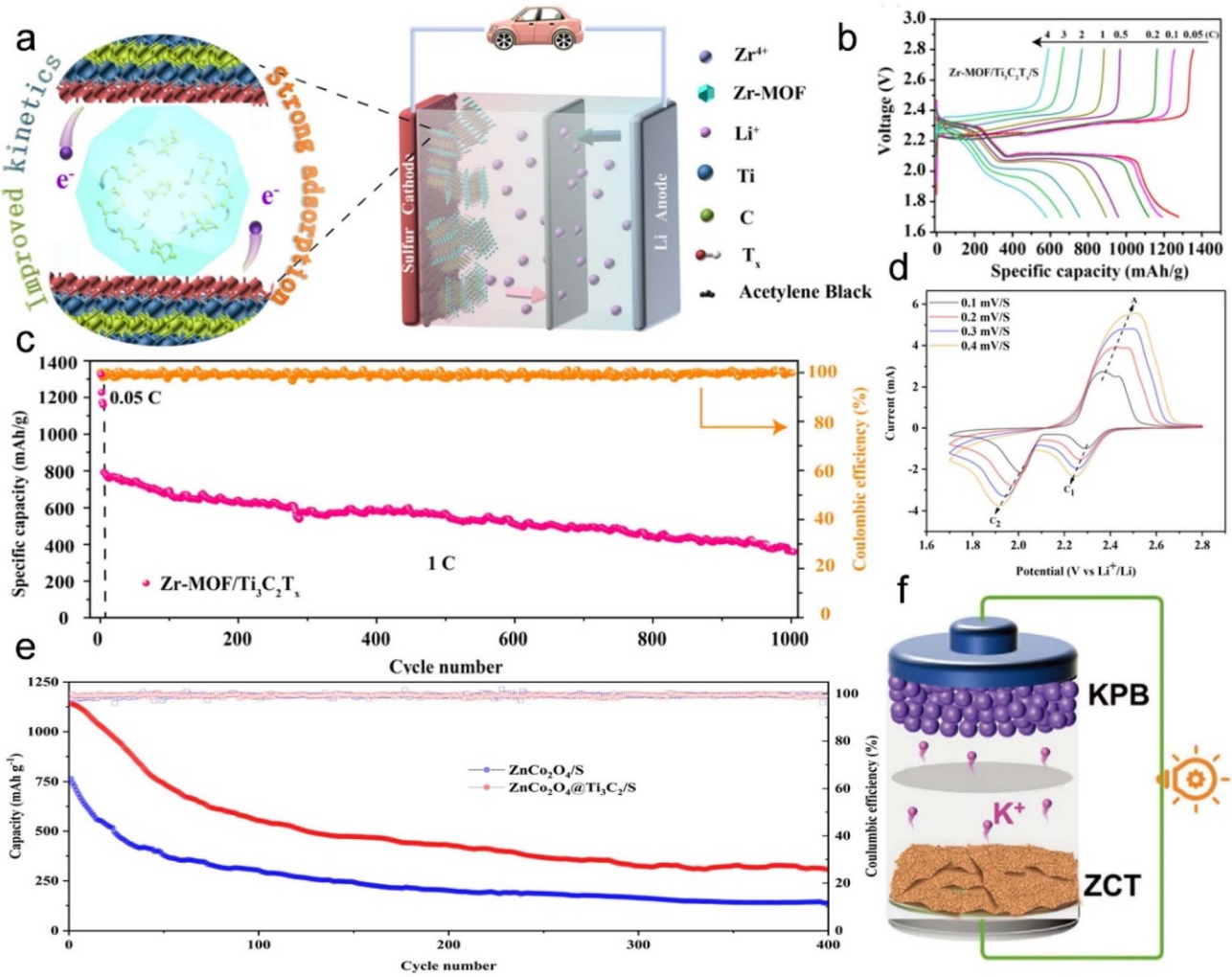

Fig. 15 (a) The working mechanism of the Zr-MOF/$Ti_3C_2T_x$/S in LSBs. (b) Charge/discharge voltage profiles of the Zr-MOF/$Ti_3C_2T_x$. (c) Cycle performance of the Zr-MOF/$Ti_3C_2T_x$ at 1C. (d) CV curves of $ZnCo_2O_4$@Ti_3C_2/S. (e) Cycling performance for $ZnCo_2O_4$@Ti_3C_2/S cathodes at 0.5C. (f) Schematic illustration of KPB||ZCT full cells. (a–c) Reproduced with permission.[177] Copyright 2021, American Chemical Society. (d and e) Reproduced with permission.[244] Copyright 2021, Elsevier. (f) Reproduced with permission.[268] Copyright 2022, Wiley.

corresponding data visualization provided in Fig. 15e. The CV curves analysis across scanning rates (0.1–0.4 mV s^{-1}), as depicted in Fig. 15d, confirmed the material's stable redox behavior.[244] Recent developments introduced the 45@ZnSe–CoSe/MXene/S composite as a high-performance cathode candidate for LSB systems. Comprehensive electrochemical characterization demonstrated multiple superior attributes: a substantial initial capacity of 1198.5 mA h g^{-1} at 0.1C, robust rate capability maintaining 489.8 mA h g^{-1} at 2C, along with exceptional cycling stability and electrochemical reversibility. These collective properties significantly enhance sulfur redox kinetics, positioning this material as a promising solution for durable LSB applications.[266]

In addition to the previously discussed LIBs and LSBs, several other representative battery systems have been explored. For instance, Hu and co-workers demonstrated ZnTe an effective anode candidate for K^+ storage, subsequently synthesizing the ZnTe@C/$Ti_3C_2T_x$ (ZCT) nanohybrids.[268] The ZCT exhibited a high capacity of 408.0 mA h g^{-1} at 0.1 A g^{-1} and superior long-term cycle ability (230.2 mA h g^{-1} at 1.0 A g^{-1} after 3500 cycles), making it a promising candidate for practical applications. Fig. 15f provides a schematic illustration of potassium Prussian blue (KPB)||ZCT full cells. Furthermore, Na *et al.* have highlighted the application of 3D MXene/ZnSe@NC as anode materials in KIBs. This innovative architecture exhibited enhanced electrochemical performance, maintaining a capacity retention of 238 mA h g^{-1} at 0.5 A g^{-1} through 1000 charge–discharge cycles, while delivering 110 mA h g^{-1} under 2.0 A g^{-1}.[269] Concurrently, sodium-ion batteries (SIBs) have garnered as a cost-effective energy storage solution, benefiting from the abundant availability and versatile substitution characteristics of Na^+-related materials, establishing it as a leading candidate to replace Li^+-based systems in contemporary battery applications. Yang and co-workers successfully prepared Ti_3C_2-ZIF-67, which was utilized as microbial fuel cell anode material. This engineered interface significantly enhanced extracellular electron transport efficiency through optimized microorganism colonization and enhanced biodiversity preservation at the bioelectrode interface. These findings establish new paradigms for MXene-based nanomaterials in bioelectrochemical energy conversion systems.[127] Shi and co-workers reported the $CoSe_2$@C/MXene composite, which, when used as an electrode for SIBs, exhibited high cyclic stability and rate performance.[265] Subsequently, the $CoFe_2O_4$@carbon@alkalized MXene composite was found to reduce the diffusion pathways for both Li^+ and Na^+. As a negative electrode material for batteries, it demonstrated superior rate capability and high capacity retention, achieving a satisfactory rate performance of 149 mA h g^{-1} at 5 A g^{-1} and a discharge capacity of 130 mA h g^{-1} at 1 A g^{-1} even after 1000 cycles for SIBs.[240] In parallel, the Co_3C/MXene@C electrodes were constructed, exhibiting exceptional energy storage characteristics including enhanced specific capacity and remarkable electrochemical activity. The optimized architecture enabled stable charge storage with capacity retention of 236 mA h g^{-1} after 100 cycles for KIB, while SIB systems demonstrated 275.9 mA h g^{-1} under identical cycling conditions. Particularly noteworthy were the high-rate capabilities, with capacities maintaining 80.6 mA h g^{-1} for KIBs and 105 mA h g^{-1} for SIBs at 2000 mA g^{-1}.[312] In complementary research, Liu *et al.* developed a hierarchically structured CoP-NC@$Ti_3C_2T_x$ composite. Electrochemical evaluation revealed that this sandwich-type architecture achieved outstanding rate performance (147.8 mA h g^{-1} at 2000 mA g^{-1}) along with unprecedented cycling stability, sustaining capacity retention exceeding 100% through 2000 continuous charge–discharge cycles.[255] Recently, Sun *et al.*[314] developed zinc ion batteries (ZIBs) based on 3D cross-linked VO_X/V_2CT_X-MXene-*x* composite, the device delivers specific capacities of 336.39 mA h g^{-1} and 213.06 mA h g^{-1} at 1 A g^{-1} and 10 A g^{-1} with excellent rate performance, and an energy density of 356.27 Wh kg^{-1} at 1280 W kg^{-1}.

3.2. Supercapacitors

SCs have emerged as promising candidates for next-generation energy storage devices due to their exceptional cycle longevity, fast charge/discharge capabilities, and sustainable characteristics. These distinctive advantages enable SCs to outperform conventional energy storage technologies including dielectric capacitors, fuel cells, and rechargeable batteries.[139] The implementation of MOF materials leverages their unparalleled structural versatility, adjustable nanoscale porosity, and expansive interfacial areas,[70] while MXene demonstraties particular efficacy as an electrochemical substrate through its remarkable mechanical resilience and densely populated reactive sites.[152] Therefore, the unique properties of MOF/MXene composites are crucial for SCs.[315,316] A comprehensive compilation of recent advancements in MOF/MXene composite research specific to SCs has been systematically organized in Table 2.

Early studies by Jia *et al.* engineered MIL-100(Fe)/$Ti_3C_2T_x$ MXene electrodes for SCs. The nanospheres, embedded within MXene nanosheets, were able to store more ionic charge. The composite electrode exhibited a maximum energy density of 85.53 Wh kg^{-1} coupled with 962.17 F g^{-1} specific capacitance at 0.5 A g^{-1}.[134] More recently, Ramachandran *et al.* successfully synthesized Co-MOF/$Ti_3C_2T_x$, which exhibited an ultra-high areal capacitance of 18.7 F cm^{-2} and demonstrated good reversibility. This material was proposed as a novel binder-free electrode material for SCs. Fig. 16a presents the CV response of Co-MOF/$Ti_3C_2T_x$@Ni at various scan rate. The cycling stability of Co-MOF@Ni and Co-MOF/$Ti_3C_2T_x$@Ni was comparatively analyzed through galvanostatic charge–discharge (GCD) measurements at 6 mA cm^{-2}, as illustrated in Fig. 16b. Notably, the Co-MOF/$Ti_3C_2T_x$@Ni hybrid demonstrated enhanced electrochemical durability with 92.1% capacitance preservation after 3000 cycles.[139] Yang *et al.* fabricated MOF/MXene/NF-300 as electrode, which demonstrated superior performance (1 A g^{-1}, 2453 F g^{-1}). Notably, the prepared MOF/MXene/NF-300 electrode material showed exceptional electrochemical durability, maintaining 83.84% capacitance retention through 3000 cycles.[151] Zhang *et al.* constructed a $Ti_3C_2T_x$/Ni-MOF-based SC achieving remarkable energy storage performance, with specific capacitance reaching 1124 F g^{-1} at 1 A g^{-1}(Fig. 16c). This configuration maintained 62% capacity

Table 2 MOF/MXene-based materials for SCs

MOF/MXene-based materials	Surface area	Current density	Capacitance	Cycling performance (capacitance retention, cycle, current density)	Electrolyte	Ref.
Pure MOF/MXene						
MIL-100(Fe)/$Ti_3C_2T_x$	529.49 $m^2 g^{-1}$	0.5 A g^{-1}	962.17 F g^{-1}	93%, 10 000, 0.5 A g^{-1}	6 M KOH	134
Co-MOF/$Ti_3C_2T_x$	14.012 $m^2 g^{-1}$	3 mA cm^{-2}	18.7 F cm^{-2}	92.1%, 3000, 6 mA cm^{-2}	3 M KOH	139
$Ti_3C_2T_x$/Ni-MOF	96.6 $m^2 g^{-1}$	1 A g^{-1}	1124 F g^{-1}	83.2%, 4000, 10 A g^{-1}	6 M KOH	148
MXene/Ni-MOF	184 $m^2 g^{-1}$	0.5 A g^{-1}	979 F g^{-1}	98%, 5000, 3 mA cm^{-2}[a]	3 M KOH	70
Ni-ZIF-67-200/K-Ar-MXene	549.78 $m^2 g^{-1}$	0.5 A g^{-1}	557C g^{-1}	66%, 5000, 2 A g^{-1}	6 M KOH	150
Ni-MOF/$Ti_3C_2T_x$	167.74 $m^2 g^{-1}$	0.5 A g^{-1}	497.6 F g^{-1}	85%, 1000, 0.5 A g^{-1}	6 M KOH	152
Ni-BDC/V_2CT_x/NF	14.34 $m^2 g^{-1}$	1 A g^{-1}	2453 F g^{-1}	83.84%, 3000, 1 A g^{-1}	1 M KOH	151
MXene@Ni-HHTP	—	0.5 A g^{-1}	416.6 F g^{-1}	102.13%, 3000, 3 A g^{-1}	3 M KOH	156
Ni-MOF@MXene	—	1 A g^{-1}	1160.5 F g^{-1}	52.2%, 10 000, 10 A g^{-1}	3 M KOH	157
Ni-MOF/MXene	—	1 A g^{-1}	716.19 F g^{-1}	74.22%, 2000, 5 A g^{-1}[a]	1 M KOH	158
MXene/ZIF-8	—	0.5 A g^{-1}	1279.5 F g^{-1}	90.88%, 10 000, 5 A g^{-1}	7 M KOH	168
Ti-MOF@$Ti_3C_2T_x$	85 $m^2 g^{-1}$	0.2 A g^{-1}	154 F g^{-1}	84%, 5000, 1 A g^{-1}	1 M KOH	203
Ni/Co-MOF@$Ti_3C_2T_x$-NH_2	129.22 $m^2 g^{-1}$	0.5 A g^{-1}	1924 F g^{-1}	58.13%, 10 000, 10 A g^{-1}	3 M KOH	186
NiCo-MOF/MXene	38.2 $m^2 g^{-1}$	1 A g^{-1}	1176.8 F g^{-1}	72.5%, 5000, 10 A g^{-1}	2 M KOH	188
MXene/Ni,Co-MOF	11 $m^2 g^{-1}$	1 A g^{-1}	58 mA h g^{-1}	89%, 10 000, 1 A g^{-1}	1 M KOH	189
MXene-FeCu-MOF	—	3 mA cm^{-2}	440 mA h g^{-1}	93%, 5000, 15 mA cm^{-2}	2 M KOH	193
Meso-CuZn-MOFs@$Ti_3C_2T_x$	72 $m^2 g^{-1}$	0.2 A g^{-1}	404 F g^{-1}	88.7%, 5000, 1 A g^{-1}[a]	3 M KOH	196
MnNi-MOF-MXene	251.77 $m^2 g^{-1}$	1 A g^{-1}	1028C g^{-1}	68.9%, 10 000, 10 A g^{-1}	2 M KOH	198
MOF composite/MXene						
$Ti_3C_2T_x$/ZIF-67/CoV_2O_6	49.466 $m^2 g^{-1}$	1 A g^{-1}	285.5 F g^{-1}	94.4%, 4000, 3 A g^{-1}	3 M KOH	120
CA@MIL-101(Cr)/MXene	208 $m^2 g^{-1}$	1.5 A g^{-1}	2720 F g^{-1}	84%, 10 000, —	—	219
MOF derivative/MXene						
Co_3O_4@MXene	76.14 $m^2 g^{-1}$	1 A g^{-1}	732.5 F g^{-1}	83%, 5000, 7 A g^{-1}	6 M KOH	317
$CoFe_2O_4$/$Ti_3C_2T_x$	—	0.2 mA cm^{-2}	2467.6 F cm^{-3}	88.2%, 10 000, 1.5 mA cm^{-2}[a]	1 M LiCl	238
MnO_2@Co_3O_4-PC@MXene-CNF	230.24 $m^2 g^{-1}$	1 A g^{-1}	475.4 mA h g^{-1}	92.08%, 10 000, 2 A g^{-1}	2 M KOH	245
Co_9S_8@MXene@Bi_2O_3	73.57 $m^2 g^{-1}$	1 A g^{-1}	646.1 F g^{-1}	86.8%, 7000, 2 A g^{-1}	6 M KOH	251
MXene@$NiCo_2S_4$	53.92 $m^2 g^{-1}$	1 A g^{-1}	451.12 mA h g^{-1}	90.68%, 10 000, 5 A g^{-1}[a]	2 M KOH	273
$CoNi_2S_4$/MXene/NF	—	1 A g^{-1}	933C g^{-1}	80.5%, 10 000, 10 A g^{-1}[a]	3 M KOH	318
MXene-CoS	399 $m^2 g^{-1}$	3 mA cm^{-2}	447 mA h g^{-1}	94%, 5000, 30 mA cm^{-2}	2 M KOH	275
MXene@$CoSe_2$/Ni_3Se_4	740.93 $m^2 g^{-1}$	1 A g^{-1}	283 mA h g^{-1}	75%, 10 000, 5 A g^{-1}	3 M KOH	263
GO/MXene@NiZrP	48.89 $m^2 g^{-1}$	1 A g^{-1}	2358 F g^{-1}	87.5%, 10 000, 10 A g^{-1}	6 M KOH	260
MXene@PCNF	405.59 $m^2 g^{-1}$	1 A g^{-1}	572.7 F g^{-1}	96.4%, 10 000, 2 A g^{-1}	3 M KOH	319
MXene@cobalt hydroxide	85.10 $m^2 g^{-1}$	1 A g^{-1}	348.55 F g^{-1}	—	3 M KOH	320

[a] Electrochemical properties measured in a two-electrode configuration, others in three-electrode configuration.

retention at 20 A g^{-1}.[148] Further advancements were reported by Zheng *et al.* through MXene@Ni-MOF composites synthesis, attaining 979 F g^{-1} specific capacitance at 0.5 A g^{-1} with merely 2% capacity degradation after 5000 cycles. The electrochemical charge storage mechanism of this hybrid material is visually detailed in Fig. 16e.[70] Olatoye and co-workers introduced a novel Ni-ZIF-67 (NZ) composite architecture, followed by the development of NZ-R-2-200/K-Ar-MXene through surface modification of K-Ar-MXene with NZ-R-2-200 NPs. The fabricated asymmetric supercapacitor, employing NZ-R-2-200/K-Ar-MXene as positive electrode in combination with NPC/rGO negative electrode, demonstrated exceptional electrochemical performance. This configuration achieved specific energy and power values of 27.48 Wh Kg^{-1} and 400 W kg^{-1} respectively, while maintaining operational stability through 2000 cycles.[150] Fig. 16f depicts an all-solid-state asymmetric flexible SC assembled using a Ni-MOF/$Ti_3C_2T_x$ nanocomposite as the cathode and activated carbon (AC) as the anode.[152] The Ni-MOF//MXAC composite was electrochemically characterized in a 2 M KOH electrolyte under a two-electrode configuration. CV analysis at 30 mV s^{-1} revealed capacitive performance of 536 F g^{-1} (1 A g^{-1}, 0–0.4 V) and 298 F g^{-1} (−1–0 V) for this electrode system.[153] In comparative studies, MXene/ZIF-8-4 hydrogel-based asymmetric supercapacitors achieved notable energy storage characteristics with 354.7 F g^{-1} at 0.5 A g^{-1} and 57.84 Wh kg^{-1} energy density at 0.628 kW kg^{-1}.[168] Another system, Ni/Co-MOF@MXene-NH_2//AC configuration demonstrated enhanced energy storage metrics in three-electrode testing, delivering 1924 F g^{-1} at 0.5 A g^{-1} with sustained 98.1 Wh kg^{-1} at 600 W kg^{-1}, alongside exceptional cycling stability through 15 600 cycles.[186] The NiCo-MOF/MXene system exhibited superior charge storage capacity (1176.8 F g^{-1} at 1 A g^{-1}) combined with 72.5% capacity retention after extended cycling, confirming its structural durability.[188] MXene-FeCu-MOF//AC hybrids displayed remarkable electrochemical persistence, maintaining 89% initial capacity (440 mA h g^{-1}) through 10 000 operational cycles.[193]

In the realm of MOF composites/MXene, Liu *et al.* strategically engineered 3D hollow-structured $Ti_3C_2T_x$/ZIF-67/CoV_2O_6 hybrids through the synergistic integration of ZIF-67 and

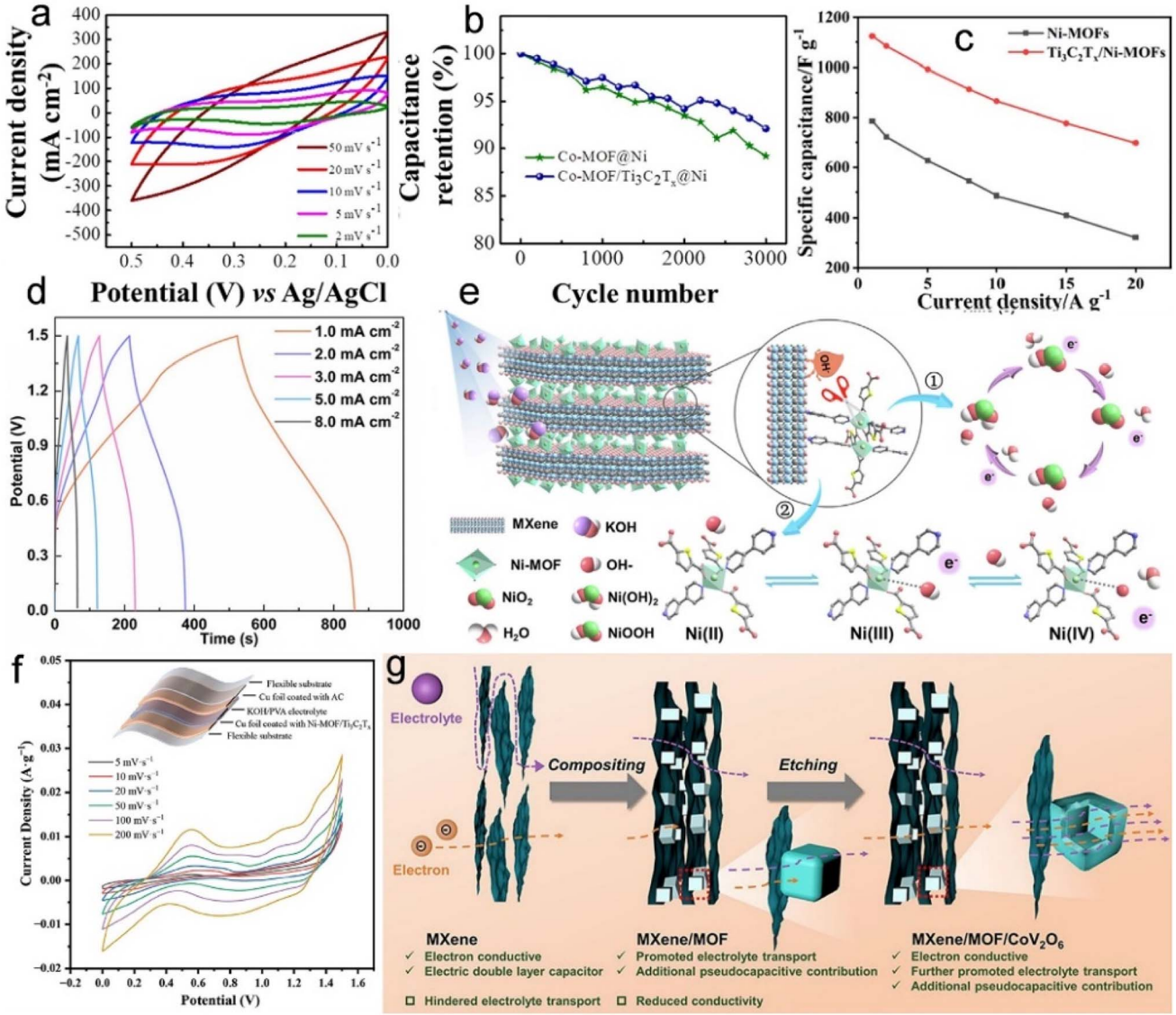

Fig. 16 (a) CV curves of Co-MOF/$Ti_3C_2T_x$@NF at different scan rates. (b) Capacitance retention of Co-MOF@NF and Co-MOF/$Ti_3C_2T_x$@NF. (c) Rate performance of $Ti_3C_2T_x$/Ni-MOF. (d) GCD curves of MXene@Ni-MOF. (e) The charge/discharge mechanism of MXene@Ni-MOF. (f) Schematic illustration of flexible SC and the CV curves of Ni-MOF/$Ti_3C_2T_x$//AC device. (g) Schematic of electrolyte/electron transport in $Ti_3C_2T_x$, $Ti_3C_2T_x$/ZIF-67 and hollow $Ti_3C_2T_x$/ZIF-67/CoV_2O_6 electrodes. (a and b) Reproduced with permission.[139] Copyright 2018, Elsevier. (c) Reproduced with permission.[148] Copyright 2021, Elsevier. (d and e) Reproduced with permission.[70] Copyright 2022, Elsevier. (f) Reproduced with permission.[152] Copyright 2023, Multidisciplinary Digital Publishing Institute. (g) Reproduced with permission.[120] Copyright 2023, Wiley.

$Ti_3C_2T_x$/ZIF-67. Electrochemical evaluations revealed that the optimized composite electrode exhibited a specific capacitance of 285.5 F g^{-1}, a significant increase compared to that of the ZIF-67 and $Ti_3C_2T_x$/ZIF-67 electrode. The schematic representation in Fig. 16g illustrates electron/electrolyte transport pathways within $Ti_3C_2T_x$-based electrodes.[120]

In the field of MOF derivatives/MXene composites, Xie and colleagues fabricated a porous Co–Fe oxide nanorod derived from $Ti_3C_2T_x$-supported MOF. This innovative design enabled the fabrication of fully pseudocapacitive flexible supercapacitors with enhanced energy storage characteristics. The optimized composite exhibited outstanding electrochemical performance in 1 M LiCl electrolyte, achieving a high volumetric capacitance of 2467.6 F cm^{-3}. The flexible energy storage device maintained 88.2% initial capacitance after 10 000 cyclic operations, demonstrating remarkable durability.[238] Kshetri *et al.* engineered multifunctional composite electrodes through an innovative integration strategy: capacitive-type Co-PC@MXene-CNF paired with battery-type MnO_2@Co_3O_4-PC@MXene-CNF. This configuration enabled their flexible wearable hybrid SC to achieve 72.5 Wh kg^{-1} energy density at 832.4 W kg^{-1}, while demonstrating exceptional cyclic stability with >90.36% capacity preservation.[245] In a parallel advancement, Wu *et al.* synthesized a Ti_3C_2@Co_3O_4/ZnO composite. When paired with AC cathodes in Li-ion hybrid capacitors, the system exhibited remarkable energy storage characteristics: 196.8 Wh kg^{-1} at

174.9 W kg^{-1}, sustaining 87.5Wh kg^{-1} even under high-power conditions (3500 W kg^{-1}). The device maintained 75% capacitance retention after 6000 cycles at 2 A g^{-1}, confirming its electrochemical durability.[246] Wang *et al.* synthesized Co_9S_8-2@MXene@Bi_2O_3 composite, which exhibited long-term cyclic stability and high discharge capacitance (646.1 F g^{-1} at 1 A g^{-1}), these enhanced electrochemical properties were attributed to the unique core–shell architecture and optimized interfacial interactions between MXene and Bi_2O_3.[251] In contrast, Yang *et al.* fabricated a hierarchically structured MXene@$CoSe_2$/Ni_3Se_4 with honeycomb morphology, delivering 283 m Ah g^{-1} capacity at 1 A g^{-1} while maintaining 80% initial capacity after 5000 cycles, thereby establishing new benchmarks for SC energy storage systems.[263] Meanwhile, MXene-CoS hybrids derived from MOFs have emerged as promising alternatives, leveraging their mesoporous structure (447 mA h g^{-1} at 3 mA cm^{-2}) with enhanced ion transport pathways and surface reactivity.[275] Most recently, Hussain *et al.*[321] reported a novel NH^{4+} hybrid SC, assembled by Co-MOF@MXene carbonized nanofibers (MXCNF) cathode constructed by Co-MOF nanoflowers hydrothermally anchored on MXCNF through integrated electrospinning-carbonization synthesis, and a MXCNF anode. The architecture leveraged vertically aligned MXene cores for enhanced electrical conduction, complemented by homogeneously dispersed Co-MOF surface modifications that optimized redox-active surface utilization. This configuration achieved remarkable electrochemical performance, delivering 41.5 mW h kg^{-1} at 800 mW kg^{-1} power output while maintaining 87% cyclic stability over 16 000 cycles.

3.3. Sensors

MOF/MXene-based materials are extensively utilized in the realm of sensing.[322,323] Table 3 provides a comprehensive summary of MOF/MXene-based materials for sensors.

A novel electrochemical approach for As(III) monitoring was developed by Xiao *et al.*, utilizing a Fe-MOF/MXene composite-modified GCE. Fig. 17a illustrates the operational mechanism of adsorption-enhanced As(III) quantification through square wave anodic stripping voltammetry (SWASV). Experimental results indicate that the synergistic interaction between Fe-MOF nanostructures and MXene substrates significantly enhances both the preconcentration efficiency of As(III) and the electrochemical detection sensitivity, outperforming the individual components. This sensor has been successfully applied to the determination of As(III) in real water samples. Fig. 17b presents the SWASV responses of the Fe-MOF/MXene-1.5/GCE in 0.1 M PBS electrolyte containing progressively increasing concentrations of As(III). A linear relationship between electrochemical signals and analyte levels is demonstrated in the inset through current-concentration calibration curves.[133] Wang *et al.* successfully applied TiO_2/Ni-NC in detecting Hg^{2+}, demonstrating good catalytic activity for the electrochemical reaction of Hg^{2+}.[324] Subsequently, Cheng *et al.* constructed a H_2O_2-sensitive electrochemical platform based on Cu-MOF/MXene/GCE. Chronoamperometric analysis at −0.35 V revealed a wide detection range (1 μM–6.12 mM). The sensor displayed ultrahigh sensitivity, rapid response kinetics, and straightforward operational design, highlighting its strong potential for practical diagnostic applications.[129] Parallel research efforts addressed DA sensing requirements through innovative nanocomposite design. Paul and co-workers engineered a MOF-Ti_3C_2 hybrid system combining Zn-based MOF ([Zn_4(1,2,4,5-benzenetetra carboxylate)$_2$(H_2O)$_6$]$_n$·3$n$$H_2O$) with MXene substrates for redox-active DA quantification. Optimized conditions established linear current-concentration correlations (90–300 nM) *via* differential pulse voltammetry, achieving detection thresholds between 90–130 nM through enhanced anodic peak amplification.[130] MOF/MXene-based composites have further expanded biosensing applications: $Ti_3C_2T_x$/ZIF-8 composites enabled hydrazine monitoring[169] and HIV-1 protein,[170] with mechanistic illustrations provided in Fig. 17c. Notably, a Ce-MOF/MXene assembly was developed as a selective L-Trp detector, maintaining stable performance across 10–50 μM concentrations (Fig. 17d).[200] Furthermore, Ravipati *et al.* engineered an innovative MOF-71/V_2C MXene hydrogel using solvothermal synthesis followed by lyophilization, establishing this nanocomposite as a precision biosensor for dual-analyte quantification of levothyroxine (LT4) and carbamazepine (CBZ).[325] The developed sensor demonstrated exceptional analytical performance with extended linear response ranges spanning 10 nM to 100 μM (LT4) and 10 nM to 500 μM (CBZ), coupled with excellent selectivity and remarkably low detection thresholds of 5.6 nM (LT4) and 6.7 nM (CBZ). Owing to its intrinsic adaptability, the hydrogel showed applicability in flexible electrochemical wearables, creating new opportunities for biomedical sensor development.

Recent advances in MOF composite/MXene architectures have demonstrated remarkable versatility in self-powered biomotion and tactile sensing applications. A prominent example is the Ecoflex@Co-NPC@MXene developed by Rana *et al.*, which has been successful implementation in self-powered biodynamic detection systems.[216] This innovative configuration employs a hierarchical nanocomposite as a charge-enhancement layer in TENG, achieving a fourfold amplification in power generation efficiency compared to conventional designs. The structural architecture of this single-electrode TENG system is schematically illustrated in Fig. 17e. In the field of pathogen detection, the Zr-Fc MOF/AuNPs/4-MPBA sensing platform has emerged as a promising candidate for the ultrasensitive detection of *E. coli* O_{157}:H_7.[209] The engineered MOF matrix capitalizes on its expansive surface topology to facilitate 4-MPBA through boronic acid-cis-diol interactions with bacterial lipopolysaccharides. This interaction enables signal labels to be fixed on the electrodes, forming a faradaic cage-type structure. The resulting sensor exhibits high sensitivity, excellent selectivity, and robust stability, highlighting its potential for real-world diagnostic applications. Given the significant health risks posed by pesticide residues, there is an urgent need to develop a sensitive and rapid method for pesticide monitoring. Addressing this critical demand for agrochemical monitoring, Tu *et al.*[215] engineered a nanoengineered electrochemical sensing platform based on MXene/CNHs/β-CDMOFs for sensitive detection of carbendazim pesticide. The

Table 3 MOF/MXene-based materials for sensors[a]

MOF/MXene-based materials	Detection	Electrode	Linear ranges	Detection limits	Selectivity	Sensitivity	Ref.
Pure MOF/MXene							
Cu-MOF/MXene	H_2O_2	GCE	1–6120 μM	0.35 μM	AA, DA, UA, Glu	—	129
MOF-Ti_3C_2	DA	GCE	90–300 nM	110 nM	AA, 5-AVA	—	130
Fe-MOF/MXene	As(III)	GCE	1–10 ng L^{-1}	0.58 ng L^{-1}	—	8.94 μA ng^{-1} L^1 cm^{-2}	133
MXene@MOF	GPNMB	—	—	180.33 pg mL^{-1}	AA, GSH, IgG, Glu, L-His	—	165
MXene/ZIF-8	N_2H_4	GCE	10–7700 μM	5.1 μM	NO_3^-, SO_4^{2-}, K^+, Cl^-, DMF, ethanol, acrylic acid, 2-propanol	—	169
$Ti_3C_2T_x$/ZIF-8	HIV protein	GCE	1 fM–1 nM	0.3 fM	BSA, PSA, AFP, CEA	—	170
Ce-MOF/$Ti_3C_2T_x$	L-Trp	GCE	0.2–139 μM	0.19 μM	AA, DA, UA, L-Cys, Glu, KCl, NaCl	0.1556 μA $μM^{-1}$ cm^{-2}	200
MXene-NH_2@CeFe-MOF-NH_2	Pb^{2+}, Hg^{2+}	GCE	5–50 nM, 1–35 nM	0.95 nM, 0.32 nM	Na^+, K^+, Ca^{2+}, Fe^{3+}, Ni^{2+}, Mn^{7+}, Mg^{2+}, Al^{3+}, Cl^-, SO_4^{2-}	—, —	322
MOF composite/MXene							
Co-MOF-MXene@carbon black	Blood creatinine	—	10–800 μM	0.005 μM	UA, urea, DA, GSH	1.1 μA $μM^{-1}$ cm^{-2}	144
MXene/CNHs/β-CD-MOFs	Carbendazim	GCE	0.003–10.0 μM	1.0 nM	Cl^-, SO_4^{2-}, Na^+, Cu^{2+}, Al^{3+}, UA, AA, Glu, malathion, thiabendazole, chlorophene, fenitrothion	5.253 A mol^{-1} L	215
Eu-MOF/PDA@MXene/Fe_3O_4	TMAO	Magnetic GCE	9×10^{-18}–9×10^{-15} M	1.25×10^{-18} M	Urea, Plasma	63.73 μA M^{-1} cm^2	223
MXene@PDA/MOF	L-Cys	GCE	0.01–5 (10^{-6} M)	0.00374 (10^{-6} M)	L-Arg, L-Leu, L-Trp, L-Phe, L-Met, L-Asp, AA, UA	—	224
rGO/PDA@MXene/FeCu-MOF	Ribavirin	GCE	—	0.053 nM	Lamivudine, sulfadiazine, inosine, uridine, DA, GSH, Glu	1.43 μA nM^{-1} cm^{-2}	230
MOF derivative/MXene							
In_2O_3/$Ti_3C_2T_x$ MXene	NH_3	Au	5–100 ppm	5 ppm	HCHO, CH_3OH, CH_3COCH_3, C_2H_5OH, C_6H_6, CO, NO_2	—	242
In_2O_3/ZnO/$Ti_3C_2T_X$ MXene	Ethanol gas	—	2.15–10 ppm	—	C_2H_5OH, CH_3OH, C_3H_6O, C_3H_9N, HCHO, NH_3, $C_6H_{15}N$, NO_2	—	243
Co_3O_4/$Ti_3C_2T_x$ MXene	Ethanol gas	—	—	1 ppm	CH_3OH, C_3H_8O, C_3H_6O, NH_3	—	247
MnO_2/Mn_3O_4@Ti_3C_2 MXene/Au NPs	Methamidophos	GCE	10^{-12}–10^{-6} M	1.34×10^{-13} M	Glu, citric acid, NO_3^-, SO_4^{2-}, PO_4^{3-}, Cu^{2+}, Fe^{3+}, Zn^{2+}, Pb^{2+}	—	253
MXene-Cu/Cu_2O/C	Glu	Au	3–10 mM	1.70 mM	Lactose, fructose, sucrose, AA, urea, NaCl, KCl	—	279
TiO_2/Ni-NC	Hg^{2+}	GCE	0.001–10 μM	0.79 nM	Ca^{2+}, Pb^{2+}, Mn^{2+}, Zn^{2+}, Cd^{2+}, Cu^{2+}	—	324

[a] AA: ascorbic acid; DA: dopamine; UA: uric acid; Glu: glucose; 5-AVA: 5-aminovaleric acid; L-Trp: L-tryptophan; L-Cys: L-cysteine; GPNMB: glycoprotein nonmetastatic melanoma protein B; GSH: glutathione; IgG: human serum immunoglobulin G; L-His: L-histidine; TMAO: trimethylamine oxide; L-Arg: L-Arginine; L-Leu: L-leucine; L-Phe: L-phenylalanine; L-Met: L-methionine; L-Asp: L-aspartate; HIV: human immunodeficiency virus; DMF: *N*,*N*-dimethylformamide; BSA: bovine serum albumin; PSA: prostate-specific antigen; AFP: alpha-fetoprotein; CEA: carcinoembryonic antigen.

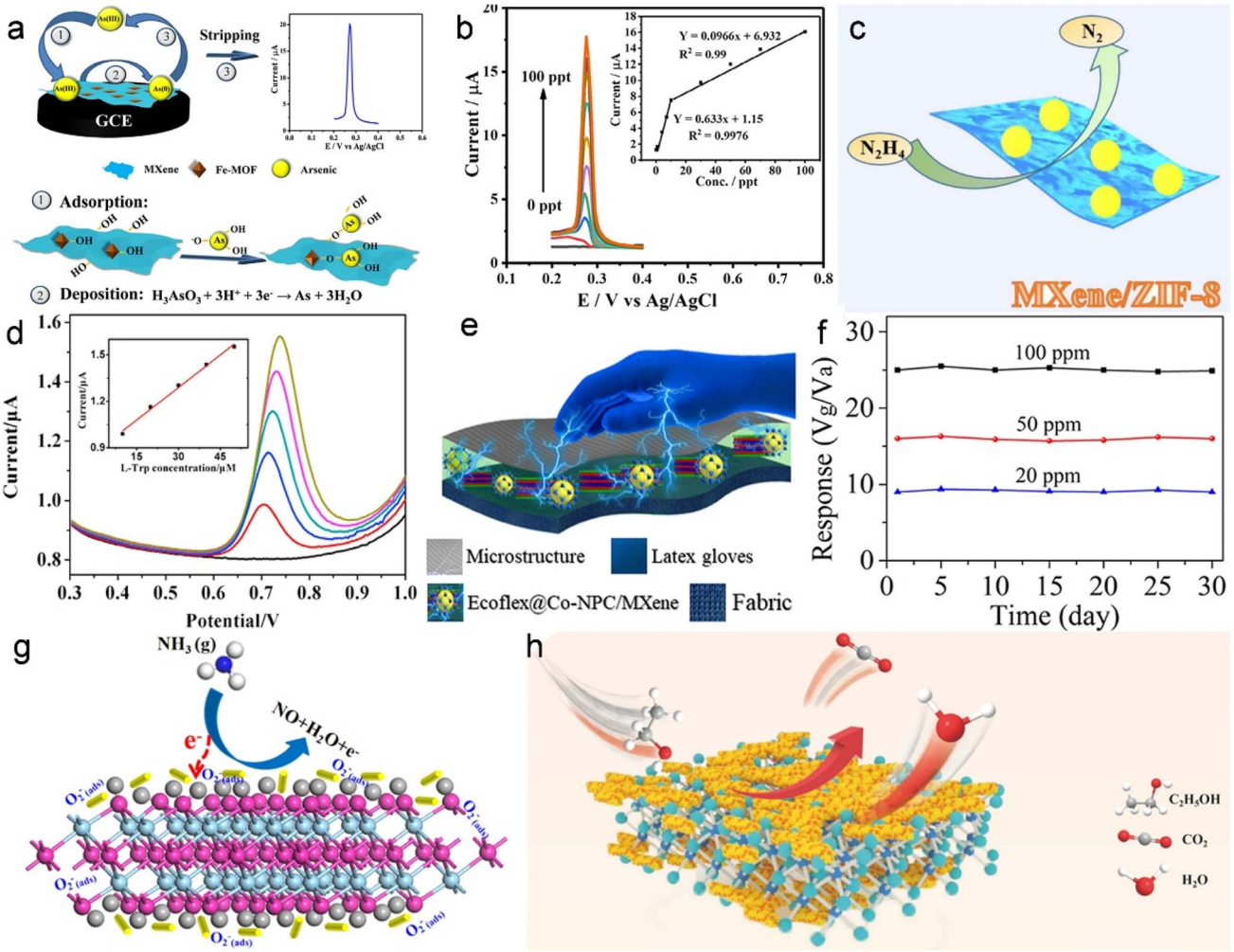

Fig. 17 (a) The schematic illustration of the adsorption-assisted As(III) detection on Fe-MOF/MXene/GCE by SWASV. (b) SWASV curves of the Fe-MOF/MXene/GCE in 0.1 M PBS solution with different As(III) concentrations. (c) Schematic illustration of N_2H_4 sensing. (d) differential pulse voltammetry curves of the Ce-MOF/$Ti_3C_2T_x$ MXene/GCE. (e) Schematic of the single electrode Ecoffex@MXene@Co-NPC nanocomposite based TENG. (f) The long-term stability of self-powered MXene/CuO sensor. (g) Schematic diagram for the possible mechanism of In_2O_3/$Ti_3C_2T_x$ MXene composites toward NH_3. (h) Schematic diagram of the gas sensing mechanism of In_2O_3/ZnO/$Ti_3C_2T_x$ MXene-based sensor. (a and b) Reproduced with permission.[133] Copyright 2021, Elsevier. (c) Reproduced with permission.[169] Copyright 2021, Wiley. (d) Reproduced with permission.[200] Copyright 2022, Elsevier. (e) Reproduced with permission.[216] Copyright 2022, Elsevier. (f) Reproduced with permission.[252] Copyright 2021, American Chemical Society. (g) Reproduced with permission.[242] Copyright 2022, Elsevier. (h) Reproduced with permission.[243] Copyright 2023, Elsevier.

synergistic action of MXene/CNHs and β-CD-MOFs extends the linear range of the MXene/CNHs/β-CD-MOFs electrode from 3.0 nM to 10.0 μM, with a low detection limit of 1.0 nM (S/N = 3). The sensor demonstrates outstanding selectivity against common interferents, excellent reproducibility, and long-term operational stability, underscoring its practical applicability for on-site and routine monitoring of pesticide contaminants.

In the field of MOF derivatives integrated with MXene architectures, Song *et al.* developed an innovative biosensing system by combining MnO_2/Mn_3O_4 with MXene/Au NPs hybrids for the detection of organophosphorus pesticides. This electrochemical platform exhibited exceptional analytical performance, demonstrating a broad detection window spanning six orders of magnitude (10^{-12} M to 10^{-6} M) and an ultralow detection threshold of 1.34×10^{-13} M. The superior sensing characteristics stem from the collaborative interaction between the MnO_2/Mn_3O_4 and MXene/Au NPs composites, which collectively establish extensive active surfaces for electrochemical processes while preserving acetylcholinesterase functionality through favorable biocompatibility. These attributes position the platform as a highly promising tool for environmental monitoring and agricultural safety evaluation.[253] Regarding MXene/CuO, an organ-like gas sensor was developed for the detection of NH_3. The TENG-driven self-powered NH_3 sensor exhibited a strong response at room temperature (V_g/V_a = 24.8@100 ppm) and showed promise in monitoring pork quality. As depicted in Fig. 17f, the MXene/CuO hybrid sensor maintained consistent performance over time, confirming its

operational durability.[252] Similarly, Liu *et al.* reported MOF-derived $In_2O_3/Ti_3C_2T_x$ MXene composites that achieved efficient NH_3 detection with strong linear correlation ($R^2 = 0.9785$) across 5–100 ppm concentrations. The architecture demonstrated rapid response and recovery dynamics (3/2 s), with Fig. 17g visually summarizing the proposed room-temperature sensing mechanism of these engineered nanomaterials.[242] More recently, $Co_3O_4/Ti_3C_2T_x$ nanocomposites with a mesoporous structure were synthesized by Bu and co-workers for ethanol sensing applications. The resulting sensor displayed excellent sensitivity, fast response and recovery kinetics, a low detection limit, high selectivity, and robust long-term stability, making it suitable for practical gas-sensing applications.[247] Additionally, $In_2O_3/ZnO/Ti_3C_2T_x$ MXene nanocomposites have been identified as a promising sensing material for ethanol detection, as depicted in Fig. 17h. These nanocomposites demonstrate a strong response to ethanol concentrations ranging from 2.15 to 10 ppm, along with outstanding selectivity towards ethanol gas.[243] Furthermore, a novel wearable, stretchable multifunctional double-layer TENG has been developed, which combines the superior nanoporosity of NPCO with the charge capture and transport characteristics of MXene/silicone. This TENG functions as a high-performance self-powered biosensor and delivers a high power density of 10.4 W m^{-2}.[250]

3.4. Catalysts

In light of rapid societal advancement, environmental pollution and escalating energy consumption have emerged as critical challenges threatening sustainable human development. Consequently, There is a growing demand for renewable energy and green energy sources within society.[326,327] In response, an increasing number of researchers are dedicated to identifying viable, sustainable, and pollution-free solutions to address these urgent global issues. Among these efforts, catalysts-serving as the core tool of green chemistry, are becoming the key to break through the technical bottlenecks.[297,328] This section systematically examines recent advancements in MXene/MOF composite catalysts and their electrocatalytic applications for energy conversion systems.

OER, HER, and ORR are three crucial reactions in the pursuit of sustainable energy.[329,330] Among these, OER serves as a fundamental process in numerous renewable energy systems. Consequently, the search for cost-effective and efficient electrocatalysts to overcome the slow kinetics and high overpotential associated with OER is paramount.[331] MOF materials have emerged as particularly attractive catalytic candidates owing to their customizable chemical properties, varied architectural features, and expansive active surfaces, positioning them at the forefront of catalyst innovation. Nevertheless, intrinsic limitations such as poor electrical conductivity and structural instability under operational conditions restrict their standalone performance. To address these challenges, researchers have strategically integrated MOFs with conductive MXene nanostructures, leveraging the excellent electron transport properties of MXenes to significantly enhance the overall electrocatalytic activity of the hybrid systems.[332,333] Notable examples include CoNi-ZIF-67@MXene and Co_2Ni-MOF@MXene, representative MOF/MXene composites developed for OER applications. Wen *et al.* fabricated a $Ti_3C_2T_x$ MXene-supported CoNi-ZIF-67 composite (CoNi-ZIF-67@$Ti_3C_2T_x$), demonstrating enhanced OER performance relative to pristine CoNi-ZIF-67, specifically achieving 275 mV onset potential *versus* RHE and a Tafel slope of 65.1 mV dec^{-1}. Comparative electrochemical metrics at 10 mA cm^{-2} are visually contrasted in Fig. 18a.[132] Furthermore, Tan *et al.* developed a series of 2D MOF/MXene composites, in which the Co_2Ni-MOF layer is tightly anchored onto the MXene nanosheet, and the well-defined interface between the two layers facilitates the accelerated charge transfer kinetics during electrocatalytic operation. The OER performances of the Co_2Ni-MOF@MXene are depicted in Fig. 18b, while the Tafel curves of Co_2Ni-MOF@MXene are presented in Fig. 18c. Among the series, Co_2Ni-MOF@MXene-1 demonstrated superior electrocatalytic activity compared to other evaluated materials, achieving both the smallest Tafel slope (51.7 mV dec^{-1}) and minimal overpotential requirement (265 mV at 10 mA cm^{-2}). These results indicate that electrostatically driven directional assembly is a viable and effective strategy for fabricating high-performance 2D OER catalysts.[187] In the realm of MOF derivatives/MXene, Zou *et al.* synthesized NiCoS/$Ti_3C_2T_x$ hybrid demonstrating enhanced electrocatalytic performance. This improvement was attributed to the strong synergistic coupling between NiCoS and $Ti_3C_2T_x$, which facilitated improved charge carrier mobility and optimized electron transport pathways.[272] Conversely, Du *et al.* investigated the influence of MXene incorporation on the OER activity of CoNi-MOF@MXene nanocomposites and observed an unexpected decrease in catalytic efficiency. This behavior was mechanistically attributed to the electron-donating nature of $Ti_3C_2T_x$ MXene, which may alter the electronic structure of the active metal sites and suppress oxidative processes.[183] Furthermore, Hu's group successfully employed CoFe-LDH/Ti_3C_2 as potential electrocatalysts for OER, achieving remarkable catalytic efficiency manifested by ultra-low overpotentials of 170 mV (10 mA cm^{-2}) and 238 mV (100 mA cm^{-2}).[277] Fig. 18d presents free energy diagrams at 0 V for the OER on the surface of individual CoFe-LDH and CoFe-LDH/MXene composite. Additionally, MXene@MOF-Co_2P composite material with engineered porosity demonstrated superior electrocatalytic behavior, requiring only 246 mV at 10 mA^{-2} with accelerated kinetics evidenced by a 28.18 mV dec^{-1} Tafel slope. This performance enhancement arises from three synergistic effects: (1) heteroatom (C, N) doping-induced electronic modulation, (2) hierarchical pore networks preserved from MOF precursors, and (3) interfacial charge transfer between Co_2P and MXene components.[257] HER significantly contributes to carbon mitigation strategies and net-zero emissions objectives. For instance, Zong *et al.* synthesized the MXene@MOF-CoP composite as a bifunctional catalyst. This innovative electrode configuration achieved notable hydrogen generation efficiency in diverse pH environments, particularly demonstrating 112 mV overpotential at pH = 14. The bifunctional activity based on MXene@MOF-CoP under alkaline conditions had a bias of

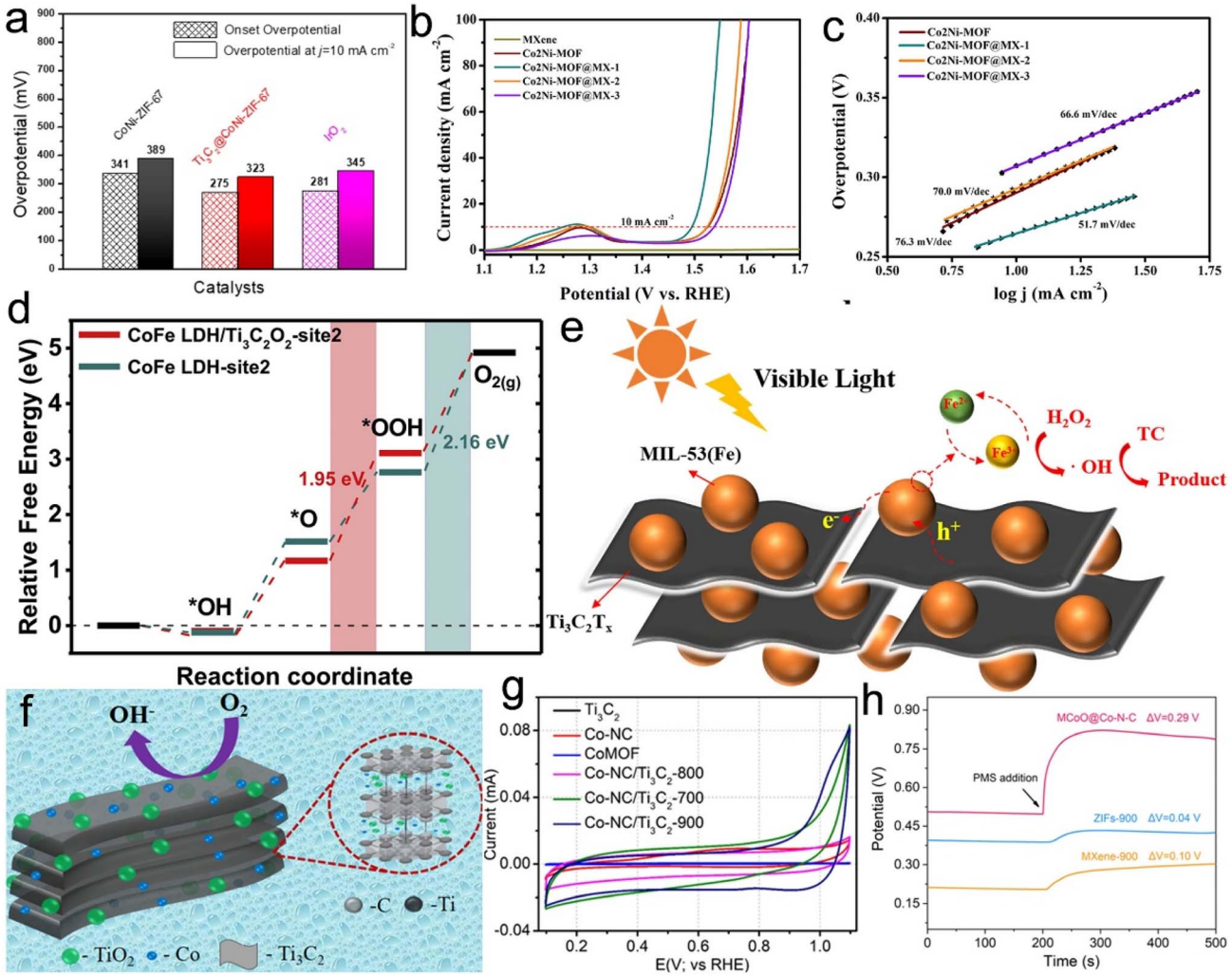

Fig. 18 (a) A comparison of the CoNi-ZIF-67@$Ti_3C_2T_x$ and CoNi-ZIF-67 catalysts in the onset potential and overpotential at 10 mA cm^{-2}. (b) LSV curves and (c) Tafel plots of Co_2Ni-MOF and Co_2Ni-MOF@MXene. (d) Free energy diagrams at 0 V for OER on the surface of individual CoFe LDH and CoFe LDH/$Ti_3C_2O_2$. (e) A schematic illustration of degradation of $Ti_3C_2T_x$ over $Ti_3C_2T_x$/MIL-53(Fe) composite under visible light irradiation. (f) A schematic illustration of electroreduction of oxygen over Co-NC/Ti_3C_2-800. (g) Comparative CV curves for the Co-NC/Ti_3C_2 composites. (h) Variation of open circuit potential for MXene-CoO@Co–N–C, ZIF, and MXene catalysts. (a) Reproduced with permission.[132] Copyright 2019, Multidisciplinary Digital Publishing Institute. (b and c) Reproduced with permission.[187] Copyright 2022, Elsevier. (d) Reproduced with permission.[277] Copyright 2021, Elsevier. (e) Reproduced with permission.[126] Copyright 2020, Elsevier. (f and g) Reproduced with permission.[232] Copyright 2021, American Chemical Society. (h) Reproduced with permission.[334] Copyright 2022, Elsevier.

1.61 V at 10 mA cm^{-2}. The catalyst prepared using the MXene@MOF-CoP electrode exhibited excellent catalytic stability.[256] Similarly, $Ti_3C_2T_x$@ZIF-8 catalyst developed by Hao *et al.* emerges as a viable alternative to expensive Pt-based catalysts, owing to its structural adaptability, enhanced conductivity, and expanded surface characteristics. CV measurements indicate an electrochemical active surface area of 122.5 cm^2 for this material, implying sustained operational stability through extended testing periods.[175] In energy conversion systems, ORR is a critical electrochemical process. Research by Parse *et al.* highlights the exceptional ORR catalytic behavior of Co-NC/Ti_3C_2-800 composite, achieving an onset potential (E_{onset}) of 1.04 V with current density reaching 4.8 mA cm^{-2} and half-wave potential ($E_{1/2}$) at 0.93 V. This performance enhancement originates from synergistic effects between the Co REDOX center and the NC matrices that form conformal coatings on $Ti_3C_2T_x$ skeleton, establishing optimized electron transport pathways during redox processes. Concurrent surface oxidation generating TiO_2 on MXene substrates further improves reaction kinetics by facilitating mass transport, ultimately boosting catalytic efficiency.[232] A schematic illustration of the oxygen electroreduction mechanism on the Co-NC/Ti_3C_2-800 composite is provided in Fig. 18f, while Fig. 18g compares the CV responses of various catalysts in N_2-saturated electrolyte.

Photocatalysts, which exhibit excellent catalytic abilities under visible light, play a crucial role in the degradation of numerous wastes. Liu *et al.* developed a novel Ti_3C_2–Fe composite demonstrating enhanced visible-light photocatalytic performance with exceptional operational stability.[126] Fig. 18e schematically illustrates the tetracycline decomposition

mechanism over TiCFe-1 under visible light. Subsequently, Qin's group engineered a Ti_3C_2-QD/Ni-MOF architecture that achieved exceptional N_2 reduction efficiency, generating 88.79 μmol g_{cat}^{-1} h^{-1} of NH_3.[146] Addressing the environmental concerns associated with methylene blue (MB), Cheng *et al.* synthesized Ni-MOF/Ti_3C_2 composites, which exhibited superior activity for the photocatalytic degradation of MB. When Ti_3C_2 was loaded with 1.5% wt%, the activity increased nearly fourfold.[147] MOF composites with high porosity and tunable bandgap energy (4.99 eV), combined with exceptional surface area characteristics, effectively enhance charge transport kinetics while suppressing photogenerated electron–hole recombination, demonstrating superior dye degradation capabilities in photocatalytic applications.[176] Zhu and co-workers developed a MXene/CuPMOF nanohybrid, which achieved efficient hydrogen evolution photocatalysis through optimized interphase connectivity.[163] Other examples of the catalytic aspects of MOF/MXene composites include a novel hybrid material synthesized by the hybrid reaction of hust-1 and $Ti_3C_2T_x$ by Gu's group. The resulting hybrid material exhibited good catalytic performance, with a conversion rate of 76.7% in the ring–opening reaction of styrene's catalytic oxidation, significantly higher than the 23.1% achieved with pure hust-1, with full activity recovery maintained through six catalytic cycles.[159] Cheng *et al.* further engineered 2D/2D Ni-MOF/Ti_3C_2 heterostructures with conductive interfaces, showing 4-fold photocatalytic activity enhancement compared to pure Ni-MOF at optimal 1.5% wt% Ti_3C_2 loading.[147] In electrocatalysis, Zhan *et al.* synthesized nitrogen-doped MXene-supported carbon-encapsulated CoP nanoarrays decorated with ultrafine Pt nanoparticles. The synergistic interaction between lattice-incorporated nitrogen, CoP, and Pt effectively mitigated CO poisoning, stabilized Pt nanoparticles, and enhanced the intrinsic activity of Pt active sites, resulting in superior electrocatalytic performance for relevant energy conversion reactions.[335]

Additionally, Li *et al.* developed a VCo-MOF@$Ti_3C_2T_x$ composite catalyst demonstrating remarkable peroxymonosulfate (PMS) activation efficiency, achieving 96.14% ciprofloxacin (CIP, 20 mg L^{-1}) within 30 min using merely 5 mg catalyst. This enhanced performance stems from the material's dual functionality in PMS adsorption and activation processes.[192] Furthermore, Guo's group engineered a MXene-CoO@Co–N–C heterostructure with sandwich-like architecture that maintained 100% bisphenol A degradation efficiency under hypersaline conditions (200 mM). The system achieved exceptional catalytic turnover (TOF = 8.64 min^{-1}) at low reagent concentrations (0.05 g per L catalyst + 0.1 g L^{-1} of PMS), representing a 22.5-fold enhancement over MOF-derived catalyst without MXene. Comparative open-circuit potential variations across catalyst types are illustrated in Fig. 18h.[334] This MXene-CoO@Co–N–C catalyst has been successfully employed to remove trace organic contaminants from brackish water using PMS, exhibiting robust decontamination efficacy even under high-salinity environments.[334] Additionally, the TS-V_2CT_x/CoV_2O_6 HN hybrid demonstrates enhanced electrocatalytic performance in both HER and OER. The MOF-derived CoV_2O_6 nanocubes possess hollow architectures that optimize electrolyte infiltration while promoting efficient charge transfer kinetics. When configured as a water splitting module, this heterostructure achieves stable current output at 10 mA cm^{-2} with a low battery voltage of 1.358 V.[249]

3.5. Electromagnetic/microwave absorption

Growing environmental challenges, particularly pervasive air pollution, have spurred intensive research into advanced adsorbent materials. Parallel demands exist for electromagnetic pollution mitigation, driving the need for lightweight broadband EMW absorbers.[336,337] MOF/MXene-based materials play a pivotal role in advancing critical technological applications.[338] The results of the latest studies on electromagnetic/microwave absorption are summarized in Table 4.

Table 4 MOF/MXene-based materials for electromagnetic/microwave absorption

MOF/MXene-based materials	EAB[a]/GHz	Thicknesses/mm	RL[b]/dB	Ref.
Electromagnetic absorption				
$Ti_3C_2T_x$/CNTs/Co	6.10	1.40	−85.80	234
$NiSe_2$–$CoSe_2$@C/$Ti_3C_2T_x$	5.68	2.60	−60.46	262
Co/TiO_2–C	9.00	2.00	−41.10	285
Fe&TiO_2@C	6.50	1.60	−51.80	286
$Ti_3C_2T_x$@CoFe@TiO_2	5.02	1.40	−62.90	239
Co/Nb_2CT_x/carbon	4.00	1.67	−60.25	288
CoPC/CNTs@MXene	5.60	1.80	−10.00	258
CNCM-7	6.80	2.70	−65.30	284
Microwave absorption				
MXene/Co-CZIF 50%	10.20	2.70	−60.09	233
MXene/Ni-CZIF 50%	4.56	3.40	−64.11	233
MXene/1D N-CNTs	8.40	1.49	−57.78	282
MXene fibers/CoNi/C and CNTs/CoNi	4.50	1.60	−51.60	184
$Ti_3C_2T_x$/CNFs/TiO_2/CoNi	4.00	1.76	−54.60	235
Ni/TiO_2/C	3.40	1.50	−45.60	287

[a] EAB: effective absorption bandwidth. [b] RL: reflection loss.

High-performance EMW absorption materials with multi-functional properties have attracted considerable scientific and technological interest. Nevertheless, significant challenges remain in their development and optimization. Xiang *et al.* reported a $Ti_3C_2T_x$/CNT/Co nanocomposite exhibiting outstanding EMW absorption performance. The enhanced EMW capability originates from synergistic mechanisms, including charge carrier migration, dipolar polarization (both electric and magnetic), interfacial polarization effects, natural resonance phenomena, and optimized multi-path reflection configurations. As predicted, the engineered composite manifests outstanding absorption characteristics with a remarkable reflection loss value reaching −85.8 dB while maintaining an ultrathin profile of merely 1.4 mm.[234] Similarly, Hou *et al.* prepared a device with a maximum RL of −60.46 dB at 2.6 mm using a $NiSe_2$–$CoSe_2$@C $Ti_3C_2T_x$ composite material with a mass fraction of $Ti_3C_2T_x$ at 40 wt%. The RL <−10 db can reach 5.68 GHz (10.32–16 GHz). This innovative EMW absorption material derives its enhanced performance from two distinctive attributes: a hierarchically layered architecture and intrinsic metalloid characteristics.[262] Additionally, Liao and co-workers synthesized a novel Co/TiO_2–C composite material through thermal treatment. This material exhibits superior microwave absorption characteristics, attaining optimal RL of −41.1 dB at 9.0 GHz (3.0 mm thickness) and −31.0 dB at 13.9 GHz (2.0 mm thickness). The operational bandwidth (RL ≤−10 dB) reached 3.04 GHz and 4.04 GHz at these frequencies, respectively. Comparative analysis with pristine MOF-derived carbon composites reveals three primary enhancement mechanisms: (1) multilayered microstructure-induced EMW scattering; (2)

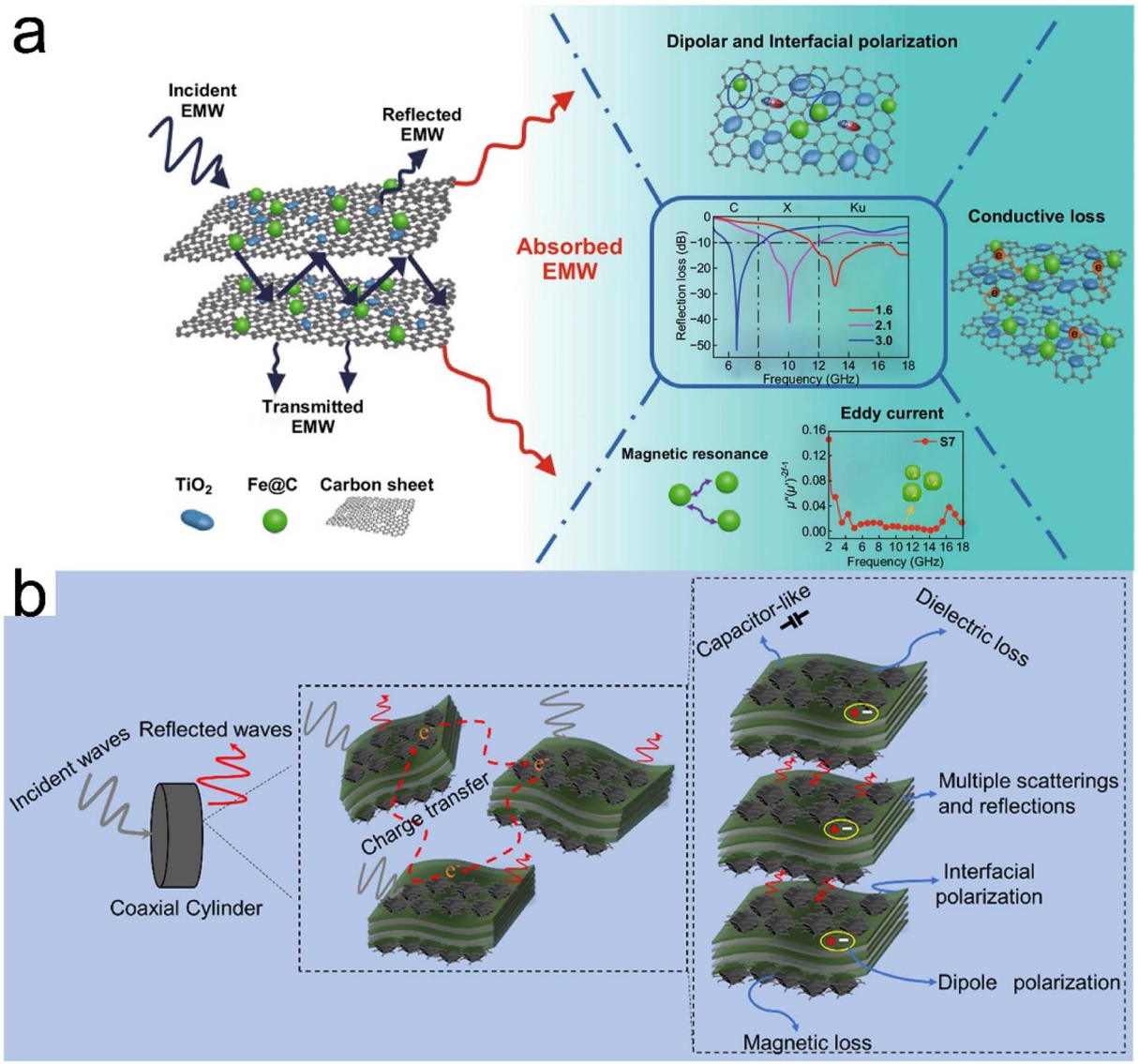

Fig. 19 (a) Illustration of EMW absorption mechanisms for Fe&TiO_2@C nanocomposites. (b) Schematic illustration of the possible MA mechanism for MXene@Co-CZIF and MXene@Ni-CZIF. (a) Reproduced with permission.[286] Copyright 2020, Springer. (b) Reproduced with permission.[233] Copyright 2020, American Chemical Society.

interface/dipole polarization effects arising from heterojunctions, structural defects, and carbon matrix interactions; (3) improved dielectric dissipation through optimized electrical conductivity. These attributes render the Co/TiO_2–C hybrid composite a promising candidate for electromagnetic absorption applications.[285]

EMW absorbing materials play a crucial role in military and engineering applications, underscoring the pressing demand for advanced absorption solutions. Lei *et al.* developed a sandwich-like $Ti_3C_2T_x$-based nanocomposite that demonstrated superior EMW absorption properties, attaining −62.9 dB minimum RL at 1.2 mm thickness within 17.95 GHz spectrum. The material demonstrated 5.02 GHz EAB (12.74–17.76 GHz) when fabricated at 1.4 mm depth, highlighting its capability as a thin, broadband absorber for mitigating pervasive electromagnetic interference in modern electronic environments.[239] In a related advancement, Deng *et al.* investigated an innovative 2D hybrid architecture incorporating Fe&TiO_2 NPs within carbon matrices. As depicted in Fig. 19a, the composite achieved 6.5 GHz EAB absorption bandwidth at 1.6 mm thickness while demonstrating −51.8 dB peak attenuation at 6.6 GHz with 3 mm configuration, offering new perspectives for MXene-derived nanomaterial synthesis.[286] Employing a porous structural engineering approach, Cui *et al.* synthesized a porous Co/Nb_2CT_x/CA composite. This composite, characterized by its low density (54.03 mg cm^{-3}), superior reflection loss, and expansive effective absorption bandwidth (reaching −60.25 dB and 4 GHz, respectively) at an ultra-thin thickness of 1.67 mm and an ultra-low filling content of 10 wt%, demonstrated a radar cross section reduction value of 31.24 dB m^{-2}, suggesting promising potential for excellent thermal insulation and flame retardant properties.[288] To develop efficient EMW absorbing materials with robust absorption capacity, Wang and colleagues synthesized the CoPC/CNTs@MXene (CCM) absorber through controlled pyrolysis of ZnCo-MOF precursors at 800 °C, followed by electrostatic self-assembly within the $Ti_3C_2T_x$ matrix. Notably, the CCM-20 composite demonstrated exceptional EMW absorption at 5.56 GHz, achieving a minimum RL of −54.2 dB. More remarkably, the CCM-30 composite variant attained effective microwave attenuation (EAB <−10 dB) at 5.6 GHz with merely 1.8 mm thickness, attributed to its hierarchical 0D/1D/2D structure that enhances electromagnetic energy dissipation through synergistic scattering mechanisms.[258]

High-performance microwave absorbing materials featuring layered and 3D architectures with abundant interfacial structures can significantly enhance EMW absorption efficiency. Such structural designs also contribute to improved microwave absorption performance, particularly by broadening the effective absorption bandwidth. Han *et al.* fabricated advanced MXene@Co-CZIF and MXene@Ni-CZIF composites (Fig. 19b) through electrostatic self-assembly, achieving exceptional EMW attenuation. The MXene/Co-CZIF 50% variant displayed notable absorption capabilities, attaining a minimum RL of −60.09 dB at 7.36 GHz with 9.3 GHz effective bandwidth (RL <−10 dB). Meanwhile, the MXene/Ni-CZIF 50% counterpart exhibited superior performance metrics, registering a peak RL value of −64.11 dB at 5.12 GHz accompanied by a 4.56 GHz operational

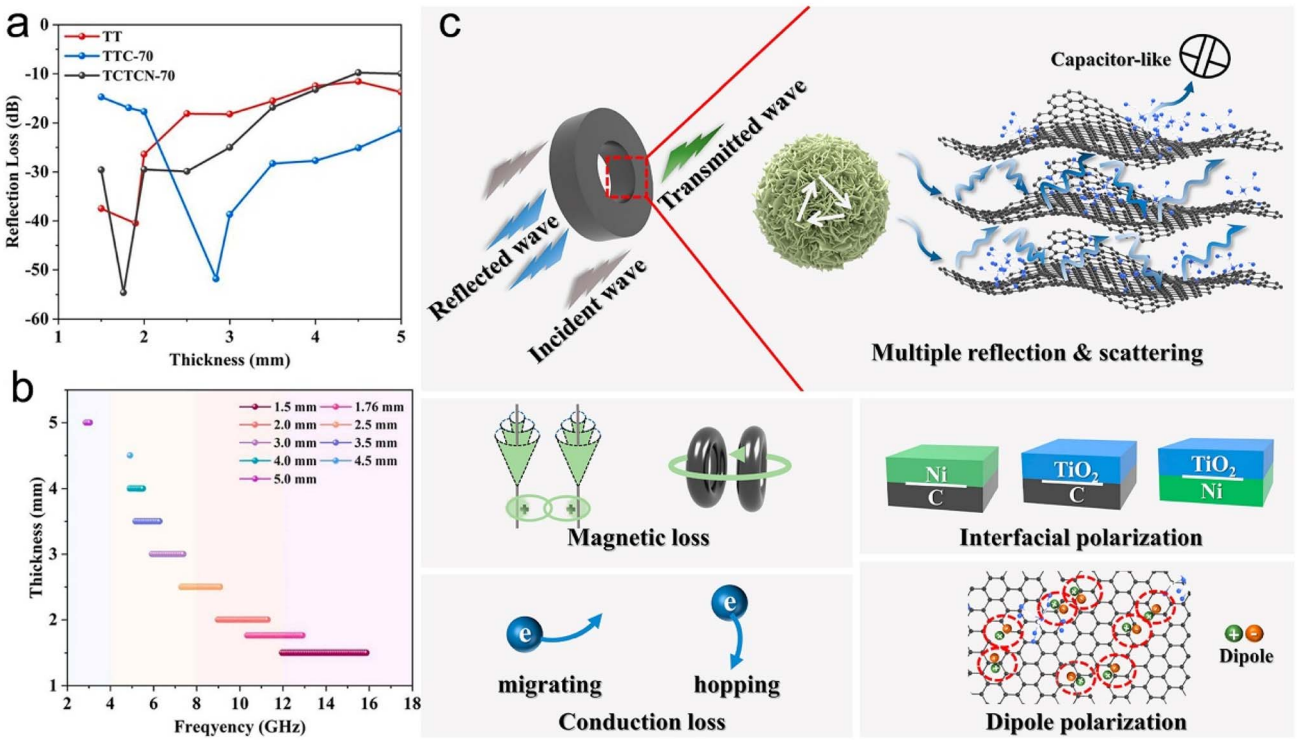

Fig. 20 (a) Dependence of the minimum RL values on the thickness and (b) EAB of $Ti_3C_2T_x$/CNFs/TiO_2/CoNi. (c) Schematic illustration of possible EMW absorption mechanisms for the Ni/TiO_2/C nanocomposites. (a and b) Reproduced with permission.[235] Copyright 2022, Elsevier. (c) Reproduced with permission.[287] Copyright 2022, Elsevier.

bandwidth under equivalent threshold conditions. This methodology provides novel design principles for developing MOF-MXene hybrid absorbers with enhanced functionality.[233] Furthermore, Liu *et al.* successfully synthesized a $Ti_3C_2T_x$/CNFs/TiO_2/CoNi nanocomposite through electrostatic self-assembly and thermal treatment, demonstrating superior EMW absorption characteristics. In this architecture, Ni-catalyzed CNFs interconnect layered MXene substrates (originally employed for MOF anchoring) to establish an interconnected framework. This structural configuration enhances dielectric loss through the creation of extensive heterogeneous interfaces, while the incorporation of CoNi NPs introduces additional magnetic loss mechanisms, enabling balanced impedance matching and synergistic attenuation. With 40 wt% filler loading, the $Ti_3C_2T_x$/CNFs/TiO_2/CoNi-70 composite achieves a RL of −54.6 dB and 4.0 GHz EAB at 1.76 mm thickness (Fig. 20a and b). This methodology advances microwave absorption material design through synergistic structural engineering.[235] Despite its high electrical conductivity, 2D laminated $Ti_3C_2T_x$ MXene suffers from an excessively high dielectric constant and a lack of magnetic loss, leading to significant impedance mismatch that restricts its practical application in EMW absorption. To tackle this challenge, Wang *et al.* successfully synthesized a multilayered Ni/TiO_2/C nanocomposite. Remarkable enhancement in EMW absorption properties was observed through precision modulation of calcination parameters. As depicted in Fig. 20c, the optimized specimen treated at 700 °C exhibited exceptional absorption characteristics: a minimum RL of −45.6 dB, an EAB of 3.40 GHz (14.6–18.0 GHz), and ultra-thin 1.5 mm. This study establishes a novel pathway for developing high-performance MXene-derived electromagnetic absorbers through simplified synthesis protocols.[287] Like other 2D materials, MXene are prone to severe aggregation and stacking issues that impede their applications. To overcome this issue, Wu *et al.* assembled a 1D heterostructure without the need for templates or rigid frameworks. The results indicated that the absorber attained a minimum RL of −51.6 dB at a matched thickness of 1.6 mm, with an EAB (RL <−10 dB) extending across 4.5 GHz within the 13.2–17.7 GHz frequency range. These findings advance the methodology for engineering efficient microwave absorption materials.[184]

3.6. Others

MOF/MXene hybrid systems exhibit dual functionalities that extend beyond the previously described chemical interactions, serving as highly effective flame-retardant additives with significant protective capabilities. For instance, Wan *et al.* employed solvothermal synthesis to fabricate 3D flower-shaped Ni-MOFs while achieving functionalization of multi-terminal layered $Ti_3C_2T_x$. The engineered Ni-MOF@$Ti_3C_2T_x$ integration substantially improved the flame-retardant performance of TPU. Quantitative analysis revealed distinct combustion parameter reductions: TPU composites containing 2% Ni-MOF, 1% Ni-MOF@$Ti_3C_2T_x$, and 2% Ni-MOF@$Ti_3C_2T_x$ exhibited smoke production rate (SPR) reductions of 41.2%, 44.1%, and 35.3% respectively, along with corresponding total smoke production decreases measuring 22.5%, 26.4%, and 23.0% relative to pure TPU. Mechanistic investigations identified three synergistic protective mechanisms: MXene's physical barrier formation, catalytic carbonization capability, and gaseous-phase radical quenching, complemented by MOF-mediated enhancement of MXene dispersion efficiency, thermal resilience, and flame suppression effectiveness.[128] To develop an eco-friendly flame-retardant system with multi-component synergy for polymer composites, Gong *et al.* synthesized a biomimetic MXene@Bi-MOF composite through interfacial engineering and integrated it into epoxy resin (EP). Experimental characterization revealed that the 2 wt% MXene@Bi-MOF modified EP composite exhibited superior fire safety performance compared to pristine EP, demonstrating significant reductions in key combustion parameters: 28.8% peak heat release rate, 45.3% peak smoke production rate, 36.5% total heat release, 30.7% peak CO emission, and 55.3% smoke factor. Additionally, the composite simultaneously achieved decreased char residue carbonization efficiency and reduced fire growth index, indicating enhanced flame inhibition mechanisms. This performance enhancement originates from the complementary interactions between MXene's catalytic carbonization capability and Bi-MOF's gas-phase radical trapping function during thermal degradation processes.[199] In another effort to enhance the flame resistance of TPU, Wan and colleagues successfully synthesized ZIF-67@MXene and integrated it into TPU materials. Remarkably, even at a low loading of 0.5 wt%, the composite demonstrated substantial fire safety enhancements: a 26% reduction in peak heat release, 9% decrease in total heat emission, 50% suppression of maximum smoke generation, and 22% mitigation in both total smoke output and carbon monoxide formation relative to unmodified TPU.[141] These improvements primarily stem from the hybrid material's barrier mechanism that effectively impedes combustion propagation within the polymer matrix.

Furthermore, MOF/MXene exhibits adsorption and sterilization properties.[339] In the design of antibacterial platforms, Guo *et al.* developed an oxygen-enriched Schottky interface by partially substituting Zn coordination sites in Zn-MOF with Ti atoms derived from $Ti_3C_2T_x$ nanosheets. This structural innovation facilitated superior separation efficiency and accelerated electron transfer of photogenerated charge carriers under 808 nm near-infrared illumination. The resulting Zn-MOF@$Ti_3C_2T_x$ composite exhibited remarkable biocompatibility and multimodal antibacterial performance, showing promising therapeutic applications for *Staphylococcus aureus*-infected wound regeneration.[172] Triazole fungicides, widely utilized in agriculture due to their high efficacy, broad-spectrum activity, and chemical stability, are the primary agents for controlling rice blast. To mitigate environmental concerns associated with triazole fungicide residues, Lu *et al.* fabricated a novel magnetic composite, Fe_3O_4@MXene@MOF-74, *via* a facile synthesis approach. Various analytical techniques were employed to characterize the morphology and properties of the fabricated composite, with its adsorption capabilities being methodically evaluated. In practical applications, satisfactory removal effects were achieved for paddy water samples.

Importantly, Fe_3O_4@MXene@MOF-74 exhibited notable antibacterial properties, achieving a 50% effective inhibitory concentration against Magnaporthe oryzae proliferation. These results underscore the composite's dual-functional capability in simultaneously removing pollutants and suppressing phytopathogens, positioning Fe_3O_4@MXene@MOF-74 as a promising candidate for agricultural water remediation.[213] More recently, Zhu *et al.* synthesized MXene/Cu-MOF composites with varying MXene loadings (3.3%, 6.7%, and 13.3%) through an *in situ* precipitation method. Compared to pristine MXene and Cu-MOF, the optimized 3.3% MXene/Cu-MOF composite showed a significant improvement in the adsorption performance of methylbenzyl sulfide in model fuels, with an equilibrium adsorption capacity reaching 87.4 mg g^{-1}.[340]

The continuous progress in science and technology has enabled the development of ion-based flexible actuators capable of sustained shape adaptation, offering a promising alternative to conventional rigid mechanical components. This innovation has generated considerable attention regarding their prospective utilization in emerging metaverse platforms and flexible robotic systems. In this regard, Garai *et al.* introduced a novel $Ti_3C_2T_x$ electrode-anchored Mn-based MOF (MnBTC), which can be utilized for super-stable electro-ionic artificial muscles. The $Ti_3C_2T_x$-MnBTC composite nanostructure forms coordination bonds, hydrogen bonds, and hydrophilic interactions with the conductive polymer poly(3,4-ethylenedioxythiophene) polystyrene sulfonate, resulting in an electrode with both mechanical flexibility and ionic activity. The $Ti_3C_2T_x$-MnBTC composite electrode ion actuator demonstrated a substantial bending displacement of 12.5 mm under 0.5 V at 0.1 Hz. It also exhibited an ultra-fast drive response time of 0.77 s at a DC input signal of 0.5 V, without any backlash phenomenon. Notably, the actuator maintained 98% long-term durability for over 43 200 seconds ($\approx$12 h) at a frequency of 1 Hz, with no distortion of the electrodes. These findings highlight the viability of MXene-MOF hybrid constructs as foundational materials for next-generation biomimetic systems requiring both dynamic performance and operational longevity.[309] More recently, Memon *et al.* developed MOF-808@MXene composites for use as triboactive materials in TENG, which exhibited a high triboelectric output of 296.22 V, 30.7 μA, and 67.4 mW m^{-2}. Furthermore, the device was stable in repetitive cycles of 5000 and showed only 34% degradation after a duration of 10 weeks, thus making it suitable as a durable and long-lasting power source based on applications in microcircuit devices.[341]

In an effort to enhance the flux, antifouling, and dye separation properties of polyether-based membranes, Yao *et al.* developed mixed matrix membranes using polyether blends combined with ZIF-8@$Ti_3C_2T_x$. With a 3% microemulsion content, the membrane achieved an optimal flux of 280 L m^{-2} h^{-1} and demonstrated an antifouling performance with a 91% bovine serum albumin rejection rate. Notably, the membrane maintained a 140 L m^{-2} h^{-1} high flux in high-salinity wastewater, achieving a dye removal efficiency of up to 98% while only removing 5% of salt ions.[173] To address the challenge of antifouling coating degradation and efficacy loss, Wang and his collaborators successfully synthesized a novel MOF, MZ-8, based on mercaptobenzothiazole (MBT). By integrating MZ-8 with MXene nanosheets, they formulated an organic–inorganic nanocomposite, MZ-8/MXene, which was employed as a reinforcing filler in PU resin. The resulting MZ-8/MXene/PU coating exhibited reduced microbial adhesion due to photothermal effects, zinc ions release, and MBT presence, leading to over 99% reduction in surface-adherent bacteria and 93% in microalgae. This advanced coating system, combining robust antifouling performance with intrinsic self-healing capabilities, presents significant potential for applications in marine antifouling and biomedical devices.[342]

Li and colleagues successfully fabricated a 3D amidoxime-functionalized $Ti_3C_2T_x$/ZIF-67 structure that demonstrated a uranium extraction capacity of 2224.54 mg g^{-1} at 1 V. The material showed exceptional selectivity towards uranium, with a reusability rate of 63.51% after 10 cycles. Furthermore, $Ti_3C_2T_x$/ZIF-67 displayed nearly 100% bactericidal efficiency against *Escherichia coli* and *Staphylococcus aureus*, underscoring its superior antibacterial properties. Under an electric field, the uranium adsorption rate of $Ti_3C_2T_x$/ZIF-67 reached 11.40 mg g^{-1} within 24 h, which is 5.3 times higher than that of physicochemical adsorption. This study presents a promising method for the efficient capture of uranium resources from seawater through electro adsorption.[142] Subas Kashif *et al.*[178] fabricated the UiO-66/MXene composite material *via* a solvothermal method. A series of studies have shown that the UiO-66/MXene composite exhibits removal rates of 98% for MB, 97% for rhodamine B, and 99% for tetracycline. The maximum adsorption capacities of UiO-66/MXene for MB, rhodamine B, and tetracycline are 312, 285, and 476 mg g^{-1}, respectively. These findings offer a promising outlook for the development of water-refining adsorbents. In another study, Deng *et al.* developed MXene nanosheets and ZIF-8 functionalized PU sponges (PU-$Ti_3C_2T_x$-MOF), resulting in excellent hydrophobicity and a water contact angle of 135°. The sponges demonstrated high adsorption capacities for liquid hazardous chemicals, absorbing up to 48–91 times their weight. Additionally, the materials exhibited excellent recyclability, retaining significant adsorption capabilities toward oils and organic solvents through five consecutive usage cycles. This study proposes a novel engineering approach for fabricating specialized polymeric sponges with significant promise for rapid response to accidental chemical spills.[174]

Navid Rabiee *et al.*[171] conducted a study on an inorganic MXene/MOF-5 nanostructure for the co-delivery of drugs and genes. The results indicated a complete dose-dependency, with a significant decrease in relative cell viability observed as the treatment time extended from 24 h to 72 h, characterized by a pronounced slope. The chitosan-alginate bilayer coating approach significantly enhanced the mitigation efficiency of nanocarriers. To evaluate their dual delivery capability, the engineered nanosystems were functionalized with pCRISPR for simultaneous tracking and therapeutic assessment. Confocal microscopy analysis demonstrated effective pCRISPR internalization in both HEK-293 and HeLa cellular models, particularly evidenced by 26% elevation in green fluorescent protein signal

intensity observed in HeLa populations. These findings suggest that this strategy, along with the optimized MXene/MOF-5 nanosystem, holds promise for further development in drug/gene co-delivery applications in animal models. To address the challenge of efficiently treating bacterially infected wounds, Guo *et al.* developed a new oxygen-rich vacancy Schottky junction. This junction notably enhances the separation of photo-induced carriers and electron transfer kinetics under 808 nm near-infrared irradiation. The resulting Zn-MOF@$Ti_3C_2T_x$ composite demonstrates remarkable biocompatibility along with multimodal antimicrobial efficacy against both *Staphylococcus aureus* and *Escherichia coli*, while promoting rapid wound healing post-*Staphylococcus aureus* infection, achieving a wound closure rate of 99%.[172] Acknowledging the limited availability of biosensors capable of detecting both chemical and biological signals, Lin *et al.* designed a multifunctional biosensor. The device integrates three functionalities: sweat-based electrochemical biosensing for UA/Glu monitoring, electrophysiological signal recording, and electrostimulation therapy delivery. Additionally, they fabricated a MOF/MXene electrode suitable for electrical muscle stimulation therapy. This research underscores its considerable potential in muscle therapy and daily noninvasive monitoring, while also offering timely nutritional guidance to individuals with hyperuricemia or hyperglycemia.[154] More recently, Alqahtani *et al.*[343] based on MXene coupled with Zn-BTC MOF and coated by chitosan for smart drug delivery, forming a MXene-Zn-BTC@chitosan nanosystem. The nanosystem could enhance cancer cell therapy by combining controlled release with effective cancer treatment and improving the cells sensitivity to therapeutic intervention, thus improving the therapeutic effect of the cisplatin-MXene-Zn-BTC@chitosan nanocomposites as a chemo-photothermal therapy agent against HepG2 cancer cells.

3.7 Summary

The superior performance of MOF/MXene-based materials across a wide range of application fields (from energy storage and sensing to catalysis and electromagnetic interference shielding) highlights their great potential. However, the scalability of these materials from laboratory-scale synthesis to industrial production and real-world deployment remains a critical, application-specific challenge that must be addressed for their widespread adoption.

A critical analysis reveals that the primary bottlenecks are inherent to the synthesis of the constituent materials and the manufacturing of final devices. The production of high-quality MXene typically involves hazardous etchants (*e.g.*, HF) and multi-step processes, which are energy-intensive and difficult to control. This poses a significant obstacle to safe, cost-effective, and environmentally sustainable large-scale production. Similarly, the synthesis of many MOF materials, especially those that require solvothermal conditions, is usually time-consuming and relies on large volumes of organic solvents, increasing the overall cost and environmental pollution. The challenges of scalability manifest differently in various applications:

(1) In energy storage (*e.g.*, batteries, SCs), the performance of electrodes like MXene@ hydroxide and ZIF-67@MXene is highly dependent on precise control of morphology and composition. Scaling up while maintaining this level of control, and ensuring the long-term stability of the MXene component, is a significant engineering hurdle.

(2) In sensing applications, the high selectivity and sensitivity of devices usually rely on complex nanostructures and surface functionalization, which may be difficult to reproduce consistently and affordably on a large scale.

(3) In catalysis, the hydrogen evolution performance of materials depends on the interfacial connectivity and exposure of active sites. Expanding the synthesis scale while maintaining these nanoscale features is a challenge.

(4) In electromagnetic interference shielding, achieving high performance typically requires a high filler loading and precise control of microstructure for the composites to balance impedance matching and attenuation. The dispersion of 2D MXene sheets and prevention of restacking are critical for maintaining performance at scale.

Furthermore, the susceptibility of MXene to oxidation under environmental conditions raises concerns about long-term reliability and shelf life, which are critical for commercial products. It is crucial to develop stable, low-cost, and scalable device fabrication processes (*e.g.*, printing, roll-to-roll manufacturing) to maintain high performance. In conclusion, while MOF/MXene-based materials offer a compelling combination of properties, their path to widespread application depends on overcoming these multifaceted scalability barriers. Future research should prioritize the development of greener, more efficient, and scalable synthesis routes for both MXene and MOF, alongside the design of stable and simplified device architectures. As highlighted in recent perspectives on zinc–air batteries,[107] a concerted effort from materials scientists, chemical engineers, and industry partners is required to bridge the gap between the laboratory and the market.

4. Summary and outlook

In summary, this review has systematically presented the synthesis and applications of MOF/MXene-based materials, categorized into pure MOF/MXene, MOF composite/MXene, and MOF derivative/MXene. The synergistic integration of the high surface area and tunable functionality of MOF materials with the exceptional electrical conductivity and rich surface chemistry composition of MXene has led to remarkable advancements across diverse fields, including energy storage, sensing, catalysis, and electromagnetic interference shielding. This powerful combination has established MOF/MXene-based materials as a development direction for next-generation materials. However, to fully exploit the potential of these materials and transform laboratory innovation into influential industrial technologies, a concerted effort is needed to address key challenges and explore new fields.

4.1. Specific research directions

Future research should focus on advancing a deeper understanding and precise control of MOF/MXene-based materials. Building upon the synthesis strategies discussed, a primary direction is advanced interfacial engineering to achieve strong chemical bonds (*e.g.*, Ti–O–C) at the interface, which is crucial for efficient and stable charge transfer. This requires a deeper mechanistic understanding of the nucleation and growth processes, potentially through the application of *in situ* characterization techniques. Furthermore, it is crucial to develop more environmentally friendly and scalable synthetic strategies. This includes innovating *in situ* and *ex situ* methods and ensuring the environmental sustainability of production processes. The field of MOF derivatives offers a rich platform for innovation, with opportunities to design novel bimetallic or multi-functional hybrids with MXene for enhanced catalytic and electrochemical performance. Finally, reinforcing the integration of theoretical and experimental research will be essential to elucidate the structure–property relationships and guide the rational design of these materials.

4.2. Challenges to commercialization

The path to commercialization is fraught with significant hurdles. The large-scale, cost-effective, and environmentally sustainable production of both high-quality MXene and MOF remains the most critical bottleneck. The synthesis of MXene usually involves hazardous etchants and complex, energy-intensive processes, while MOF synthesis can rely on large volumes of organic solvents. The long-term stability of these composites, particularly the susceptibility of MXene to oxidation, is a major concern for device reliability. Additionally, the integration of these nanomaterials into practical devices presents engineering challenges. Combining bottom-up self-assembly approaches with scalable manufacturing technologies, such as 3D printing and roll-to-roll deposition, may facilitate large-scale integration. Fostering collaboration between academia, industry, and government is crucial to translate lab innovations into commercial technologies.

4.3. Interdisciplinary opportunities

The future of MOF/MXene-based materials lies in interdisciplinary collaboration. By merging expertise from materials science, chemistry, physics, and engineering, these composites can be tailored for next-generation technologies. A promising frontier is flexible and wearable electronics, where the mechanical flexibility of MXene and the functional versatility of MOF can be harnessed for integrated health-monitoring devices. Another significant opportunity lies in smart systems and the internet of things, where MOF/MXene composites can serve as multifunctional units combining sensing, energy storage, and signal processing. Exploring their use in solid-state batteries, fuel cells, SCs, and water-splitting devices for hydrogen production represents a crucial interdisciplinary venture. This collaborative effort is indispensable for transforming the exceptional laboratory performance of MOF/MXene-based materials into transformative practical applications.

Author contributions

Shasha Zheng: writing review & editing, data curation, formal analysis, project administration, investigation, supervision. Keke Zhou: writing original draft, software. Xiaoxue Zhang: writing original draft, investigation. Ning Ren: methodology, investigation.

Conflicts of interest

There are no conflicts to declare.

Data availability

No primary research results, software or code have been included and no new data were generated or analysed as part of this review.

Acknowledgements

This work was supported by the Key Scientific Research Projects Plan of Colleges and Universities in Henan Province (No. 24A150021) and Youth Science and Technology Innovation Special Project of Zhumadian (No. QNZX202308).

References

1 Z. Pei, H. Lei and L. Cheng, *Chem. Soc. Rev.*, 2023, **52**, 2031–2081.
2 X. Luo, Y. Zhai, P. Wang, B. Tian, S. Liu, J. Li, C. Yang, V. Strehmel, S. Li, K. Matyjaszewski, G. Yilmaz, B. Strehmel and Z. Chen, *Angew. Chem., Int. Ed.*, 2024, **63**, e202316431.
3 L. Liu, Y. Pan, L. Ye, C. Liang, X. Mou, X. Dong and Y. Cai, *Coord. Chem. Rev.*, 2024, **517**, 216006.
4 S. Liang, J. Yao, D. Liu, L. Rao, X. Chen and Z. Wang, *Adv. Mater.*, 2023, **35**, 2211130.
5 I. E. Khalil, J. Fonseca, M. R. Reithofer, T. Eder and J. M. Chin, *Coord. Chem. Rev.*, 2023, **481**, 215043.
6 T. Yao, X. Zeng, X. Tao and H. Xu, *Chem. Eng. J.*, 2024, **487**, 150641.
7 S. Guo, M. Gao, W. Zhang, F. Liu, X. Guo and K. Zhou, *Adv. Mater.*, 2023, **35**, 2303065.
8 Y. Wang, Y. Yang, J. Liu, X. Zi, H. Zhu, X. Sun, Y. Miao and Y. Fu, *Chem. Eng. J.*, 2024, **500**, 156850.
9 S. Zhou, F. Jia, Y. Wei, J. Du, J. Liu, W. Dong, J. Sui, W. Xue, Y. Yang, L. Chen, X. Meng and S. Yu, *Adv. Funct. Mater.*, 2024, **34**, 2314012.
10 J. M. Huang, X. D. Zhang, J. Y. Huang, D. S. Zheng, M. Xu and Z. Y. Gu, *Coord. Chem. Rev.*, 2023, **494**, 215333.
11 S. Li, W. Han, Q. An, K. Yong and M. Yin, *Adv. Funct. Mater.*, 2023, **33**, 2303447.
12 J. Li, C. Hou, C. Chen, W. Ma, Q. Li, L. Hu, X. Lv and J. Dang, *ACS Nano*, 2023, **17**, 10947–10957.

13 Y. Song, C. Yu, D. Ma and K. Liu, *Coord. Chem. Rev.*, 2024, **499**, 215492.
14 A. H. Mamaghani, J. Liu, Z. Zhang, R. Gao, Y. Wu, H. Li, M. Feng and Z. Chen, *Adv. Energy Mater.*, 2024, **14**, 2402278.
15 J. Park, M. Lee, D. Feng, Z. Huang, A. C. Hinckley, A. Yakovenko, X. Zou, Y. Cui and Z. Bao, *J. Am. Chem. Soc.*, 2018, **140**, 10315–10323.
16 A. M. Patil, S. Moon, Y. Seo, S. B. Roy, A. A. Jadhav, D. P. Dubal, K. Kang and S. C. Jun, *Small*, 2023, **19**, 2205491.
17 H. Zhu, S. Li, L. Peng, W. Zhong, Q. Wu, S. Cheng and J. Xie, *Nano Energy*, 2024, **125**, 109571.
18 W. Zhou, Y. Tang, X. Zhang, S. Zhang, H. Xue and H. Pang, *Coord. Chem. Rev.*, 2023, **477**, 214949.
19 P. Wiśniewska, J. Haponiuk, M. R. Saeb, N. Rabiee and S. A. Bencherif, *Chem. Eng. J.*, 2023, **471**, 144400.
20 H. Abed, R. Sabouni and M. Ghommem, *RSC Adv.*, 2024, **14**, 39472–39497.
21 T. Zhao, H. Wu, X. Wen, J. Zhang, H. Tang, Y. Deng, S. Liao and X. Tian, *Coord. Chem. Rev.*, 2022, **468**, 214642.
22 B. Xu, Z. Huang, Y. Liu, S. Li and H. Liu, *Nano Today*, 2023, **48**, 101690.
23 H. Yang, L. Wang and X. Huang, *Coord. Chem. Rev.*, 2023, **495**, 215372.
24 G. Tatrari, R. An and F. U. Shah, *Coord. Chem. Rev.*, 2024, **512**, 215876.
25 R. Abazari, S. Sanati, W. K. Fan, M. Tahir, S. Nayak, K. Parida, M. El-Shahat, R. M. Abdelhameed, D. S. Nesterov, A. M. Kirillov and J. Qian, *Coord. Chem. Rev.*, 2025, **523**, 216256.
26 W. Zhang, X. Li, X. Ding, K. Hua, A. Sun, X. Hu, Z. Nie, Y. Zhang, J. Wang, R. Li and S. Liu, *RSC Adv.*, 2023, **13**, 10800–10817.
27 R. Ji, Z. Cui, T. Wu, Y. Xu, M. Yang, R. Zhang, F. Kang, Q. Huang, Q. Zhang and D. Tian, *Coord. Chem. Rev.*, 2025, **540**, 216778.
28 S. Zheng, X. Li, B. Yan, Q. Hu, Y. Xu, X. Xiao, H. Xue and H. Pang, *Adv. Energy Mater.*, 2017, **7**, 1602733.
29 Y. Xue, S. Zheng, H. Xue and H. Pang, *J. Mater. Chem. A*, 2019, **7**, 7301–7327.
30 Y. Du, X. Jia, L. Zhong, Y. Jiao, Z. Zhang, Z. Wang, Y. Feng, M. Bilal, J. Cui and S. Jia, *Coord. Chem. Rev.*, 2022, **454**, 214327.
31 C. Zhang, Y. Wu, D. Li and H. L. Jiang, *Chem. Sci.*, 2025, **16**, 13149–13172.
32 L. Jia, S. Zhou, A. Ahmed, Z. Yang, S. Liu, H. Wang, F. Li, M. Zhang, Y. Zhang and L. Sun, *Chem. Eng. J.*, 2023, **475**, 146361.
33 Z. Wang, C. Wei, H. Jiang, Y. Zhang, K. Tian, Y. Li, X. Zhang, S. Xiong, C. Zhang and J. Feng, *Adv. Mater.*, 2024, **36**, 2306015.
34 W. Zeng, X. Ye, Y. Dong, Y. Zhang, C. Sun, T. Zhang, X. Guan and L. Guo, *Coord. Chem. Rev.*, 2024, **508**, 215753.
35 Z. Wu, S. Liu, Z. Hao and X. Liu, *Adv. Sci.*, 2023, **10**, 2207174.
36 W. Cao, J. Nie, Y. Cao, C. Gao, M. Wang, W. Wang, X. Lu, X. Ma and P. Zhong, *Chem. Eng. J.*, 2024, **496**, 154097.
37 H. Wu, M. Almalki, X. Xu, Y. Lei, F. Ming, A. Mallick, V. Roddatis, S. Lopatin, O. Shekhah, M. Eddaoudi and H. N. Alshareef, *J. Am. Chem. Soc.*, 2019, **141**, 20037–20042.
38 C. Zheng, Y. Yao, X. Rui, Y. Feng, D. Yang, H. Pan and Y. Yu, *Adv. Mater.*, 2022, **34**, 2204988.
39 D. Lei, N. Liu, T. Su, Q. Zhang, L. Wang, Z. Ren and Y. Gao, *Adv. Mater.*, 2022, **34**, 2110608.
40 C. Wei, Q. Zhang, Z. Wang, W. Yang, H. Lu, Z. Huang, W. Yang and J. Zhu, *Adv. Funct. Mater.*, 2023, **33**, 2211889.
41 S. Kazim, C. Huang, N. H. Hemasiri, A. Kulkarni, S. Mathur and S. Ahmad, *Adv. Funct. Mater.*, 2024, **34**, 2315694.
42 J. Li, L. Han, Y. Li, J. Li, G. Zhu, X. Zhang, T. Lu and L. Pan, *Chem. Eng. J.*, 2020, **380**, 122590.
43 L. Sun, J. Sun, S. Zhai, T. Dong, H. Yang, Y. Tan, X. Fang, C. Liu, W. Deng and H. Wu, *Adv. Energy Mater.*, 2022, **12**, 2200113.
44 Y. Chen, H. Yang, Z. Han, Z. Bo, J. Yan, K. Cen and K. K. Ostrikov, *Energy Fuels*, 2022, **36**, 2390–2406.
45 B. Zhang, A. Boretti and S. Castelletto, *Chem. Eng. J.*, 2022, **435**, 134959.
46 X. Bai and J. Guan, *Small Struct.*, 2023, **4**, 2200354.
47 M. Bilal, A. K. Singh, H. M. N. Iqbal and G. Boczkaj, *Chem. Eng. J.*, 2023, **474**, 145020.
48 X. Fan, Y. Yang, X. Shi, Y. Liu, H. Li, J. Liang and Y. Chen, *Adv. Funct. Mater.*, 2020, **30**, 2007110.
49 L. Wang, H. Song, L. Yuan, Z. Li, P. Zhang, J. K. Gibson, L. Zheng, H. Wang, Z. Chai and W. Shi, *Environ. Sci. Technol.*, 2019, **53**, 3739–3747.
50 M. Mozafari, A. Arabi Shamsabadi, A. Rahimpour and M. Soroush, *Adv. Mater. Technol.*, 2021, **6**, 2001189.
51 I. Persson, J. Halim, H. Lind, T. W. Hansen, J. B. Wagner, L. Å. Näslund, V. Darakchieva, J. Palisaitis, J. Rosen and P. O. Å. Persson, *Adv. Mater.*, 2019, **31**, 1805472.
52 Y. Zhou, Y. Zhang, K. Ruan, H. Guo, M. He, H. Qiu and J. Gu, *Sci. Bull.*, 2024, **69**, 2776–2792.
53 J. Liu, M. Wang, C. Guo, Z. Tao, M. Wang, L. He, B. Liu and Z. Zhang, *Food Chem.*, 2023, **416**, 135839.
54 Y. Jo, Y. K. Jo, J. Lee, H. W. Jang, I. Hwang and D. J. Yoo, *Adv. Mater.*, 2023, **35**, 2206842.
55 R. Qin, J. Nong, K. Wang, Y. Liu, S. Zhou, M. Hu, H. Zhao and G. Shan, *Adv. Mater.*, 2024, **36**, 2312761.
56 S. Elbeltagi, M. Al-zharani, F. A. Nasr, A. M. Ismail, H. M. El-Tohamy, K. M. Abdelbased and Z. E. Eldin, *Int. J. Pharm.*, 2025, **674**, 125492.
57 B. Deng, Z. Liu, F. Pan, Z. Xiang, X. Zhang and W. Lu, *J. Mater. Chem. A*, 2021, **9**, 3500–3510.
58 M. Liu, Z. Zhang, M. Yang, P. Li, Y. Wang, Y. He and J. Yuan, *Composites, Part A*, 2022, **161**, 107122.
59 L. Wang, H. Liu, X. Lv, G. Cui and G. Gu, *J. Alloys Compd.*, 2020, **828**, 154251.
60 Y. Ji, Y. Zhang, J. Lu, F. Gao, X. Lv, X. Qu, G. Zhu, T. Tian, H. Pang, Y. Tian and X. Dong, *Adv. Healthc. Mater.*, 2025, **14**, 2404723.
61 Y. He, Y. Zou, L. Sun, F. Xu, Y. Xia, Y. Chen, S. Wang, Z. Hu, S. Hao and C. Xiang, *J. Energy Storage*, 2025, **119**, 116385.
62 X. Zhang, G. Jin, Y. Liu, Y. Liu, M. Zhang, C. Li, X. Zhang and D. Cao, *Adv. Compos. Hybrid Mater.*, 2025, **8**, 206.

63 X. Zhuang, S. Zhang, Y. Tang, F. Yu, Z. Li and H. Pang, *Coord. Chem. Rev.*, 2023, **490**, 215208.
64 H. Saini, N. Srinivasan, V. Šedajová, M. Majumder, D. P. Dubal, M. Otyepka, R. Zbořil, N. Kurra, R. A. Fischer and K. Jayaramulu, *ACS Nano*, 2021, **15**, 18742–18776.
65 T. Xu, Y. Wang, Y. Xue, J. Li and Y. Wang, *Chem. Eng. J.*, 2023, **470**, 144247.
66 F. Ren, L. Ma, C. Li, T. Wu, J. Zhang, L. Pei, Y. Jin, Z. Sun, Z. Guo, P. Song and P. Ren, *Carbohydr. Polym.*, 2025, **356**, 123369.
67 A. Hanan, M. N. Lakhan, F. Bibi, A. Khan, I. A. Soomro, A. Hussain and U. Aftab, *Chem. Eng. J.*, 2024, **482**, 148776.
68 I. Ijaz, A. Bukhari, E. Gilani, A. Nazir and H. Zain, *RSC Adv.*, 2023, **13**, 5643–5655.
69 H. Kefayati, Y. Yamini and M. Ghaemmaghami, *Microchim. Acta*, 2025, **192**, 145.
70 S. Zheng, H. Zhou, H. Xue, P. Braunstein and H. Pang, *J. Colloid Interface Sci.*, 2022, **614**, 130–137.
71 S. Huang, H. Wang, C. Xiang, D. Luo, H. Zeng, A. Cai, X. Ma, C. Fang and J. Deng, *J. Membr. Sci.*, 2025, **719**, 123738.
72 A. Chaouiki, M. Chafiq, R. Salghi, N. Elboughdiri, J. H. Kang, Y. G. Ko and M. Abboud, *J. Energy Chem.*, 2025, **104**, 687–715.
73 S. Bibi, S. S. A. Shah, M. A. Nazir, M. H. Helal, S. M. El-Bahy, Z. M. El-Bahy, S. Ullah, M. A. Wattoo and A. ur Rehman, *Adv. Sustain. Syst.*, 2024, **8**, 2400011.
74 Y. Zhao, J. Zhang, X. Guo, X. Cao, S. Wang, H. Liu and G. Wang, *Chem. Soc. Rev.*, 2023, **52**, 3215–3264.
75 N. Kitchamsetti and J. S. Cho, *J. Energy Storage*, 2024, **80**, 110293.
76 H. Wang, X. Li, Y. Deng, J. Jiang, H. Ma and J. Zou, *Coord. Chem. Rev.*, 2025, **529**, 216462.
77 H. Ji, Y. Liu, G. Du, T. Huang, Y. Zhu, Y. Sun and H. Pang, *Chem. Res. Chin. Univ.*, 2024, **40**, 943–963.
78 G. T. Tran, T. T. T. Nguyen and T. Van Tran, *Coord. Chem. Rev.*, 2025, **544**, 217002.
79 R. Ghanbari and E. Nazarzadeh Zare, *Coord. Chem. Rev.*, 2024, **518**, 216089.
80 Y. Zheng, S. Zheng, H. Xue and H. Pang, *Adv. Funct. Mater.*, 2018, **28**, 1804950.
81 N. A. I. M. Mokhtar, R. M. Zawawi, W. M. Khairul and N. A. Yusof, *Environ. Chem. Lett.*, 2022, **20**, 3099–3131.
82 S. Ullah, A. ur Rehman, T. Najam, I. Hossain, S. Anjum, R. Ali, M. U. Shahid, S. S. A. Shah and M. A. Nazir, *J. Ind. Eng. Chem.*, 2024, **137**, 87–105.
83 S. Gautam, S. Rialach, S. Paul and N. Goyal, *RSC Adv.*, 2024, **14**, 14311–14339.
84 Y. Absalan, M. Gholizadeh, E. B. Kim, S. Ameen, Y. Wang, Y. Wang and H. He, *Coord. Chem. Rev.*, 2024, **515**, 215972.
85 A. K. Bindra, D. Wang and Y. Zhao, *Adv. Mater.*, 2023, **35**, 2300700.
86 Y. Zhang, X. Feng, S. Yuan, J. Zhou and B. Wang, *Inorg. Chem. Front.*, 2016, **3**, 896–909.
87 F. Parsapour, M. Moradi, V. Safarifard and S. Sojdeh, *J. Energy Storage*, 2024, **82**, 110487.
88 C. Brahmi, M. Benltifa, C. Vaulot, L. Michelin, F. Dumur, F. Millange, M. Frigoli, A. Airoudj, F. Morlet-Savary, L. Bousselmi and J. Lalevée, *Eur. Polym. J.*, 2021, **154**, 110560.
89 M. Kalaj, K. C. Bentz, S. Ayala, J. M. Palomba, K. S. Barcus, Y. Katayama and S. M. Cohen, *Chem. Rev.*, 2020, **120**, 8267–8302.
90 I. Salahshoori, M. Golriz, M. Namayandeh Jorabchi, S. Moghari and H. A. Khonakdar, *Coord. Chem. Rev.*, 2025, **543**, 216919.
91 W. Lv, Y. Song, H. Pei and Z. Mo, *J. Ind. Eng. Chem.*, 2023, **128**, 17–54.
92 T. Wu, X. Liu, Y. Liu, M. Cheng, Z. Liu, G. Zeng, B. Shao, Q. Liang, W. Zhang, Q. He and W. Zhang, *Coord. Chem. Rev.*, 2020, **403**, 213097.
93 J. Aguilera-Sigalat and D. Bradshaw, *Coord. Chem. Rev.*, 2016, **307**, 267–291.
94 M. Zahran, S. Tian, J. Li, A. H. Marei, Y. Xie, Q. Liu, J. Huang, D. Wang, X. Ning, J. Wang, H. Chi and X. Li, *RSC Adv.*, 2025, **15**, 10801–10815.
95 Y. Liu, Z. Liu, D. Huang, M. Cheng, G. Zeng, C. Lai, C. Zhang, C. Zhou, W. Wang, D. Jiang, H. Wang and B. Shao, *Coord. Chem. Rev.*, 2019, **388**, 63–78.
96 M. Mukoyoshi and H. Kitagawa, *Chem. Commun.*, 2022, **58**, 10757–10767.
97 S. Tang, Y. Wang, P. He, Y. Wang and G. Wei, *Materials*, 2024, **17**, 2660.
98 J. Yu, C. Mu, B. Yan, X. Qin, C. Shen, H. Xue and H. Pang, *Mater. Horiz.*, 2017, **4**, 557–569.
99 Y. Liu, D. Huang, M. Cheng, Z. Liu, C. Lai, C. Zhang, C. Zhou, W. Xiong, L. Qin, B. Shao and Q. Liang, *Coord. Chem. Rev.*, 2020, **409**, 213220.
100 X. Lian, Y. Fang, E. Joseph, Q. Wang, J. Li, S. Banerjee, C. Lollar, X. Wang and H. C. Zhou, *Chem. Soc. Rev.*, 2017, **46**, 3386–3401.
101 J. Jiang, Y. Shi, M. Wu, M. Rezakazemi, T. M. Aminabhavi, R. Huang, C. Jia and S. Ge, *Chem. Eng. J.*, 2024, **494**, 152932.
102 Y. Chen, Y. Shi, G. Song, B. Yang and H. Pang, *Next Mater.*, 2025, **6**, 100323.
103 Q. Wu, J. Liang, D. Wang, R. Wang and C. Janiak, *Chem. Soc. Rev.*, 2025, **54**, 601–622.
104 W. K. Fan, A. Sherryna and M. Tahir, *ACS Omega*, 2022, **7**, 38158–38192.
105 Y. Ji, Y. You, G. Xu, X. Yang and Y. Liu, *Chem. Eng. J.*, 2024, **483**, 149365.
106 H. Yang, G. X. Zhang, H. J. Zhou, Y. Y. Sun and H. Pang, *Energy Mater. Adv.*, 2023, **4**, 0033.
107 T. Ramachandran, R. K. Raji and M. Rezeq, *J. Mater. Chem. A*, 2025, **13**, 12855–12890.
108 S. Venkateswarlu, S. Vallem, M. Umer, N. V. V. Jyothi, A. Giridhar Babu, S. Govindaraju, Y. Son, M. Jong Kim and M. Yoon, *J. Energy Chem.*, 2023, **86**, 409–436.
109 N. Khosroshahi, M. Bakhtian, A. Asadi and V. Safarifard, *Nano Express*, 2023, **4**, 042002.
110 B. Tahir, A. Alraeesi and M. Tahir, *Front. Chem.*, 2024, **12**, 1448700.
111 S. Afzal, A. ur Rehman, T. Najam, I. Hossain, M. A. I. Abdelmotaleb, S. Riaz, M. R. Karim, S. S. A. Shah and M. A. Nazir, *Chemosphere*, 2024, **364**, 143194.

112 S. Bagyalakshmi, K. S. Balamurugan, M. Mathankumar, A. Sivakami and N. R. Devi, *J. Mol. Struct.*, 2025, **1334**, 141838.
113 P. Cao, Y. L. Liu, Q. Zhang, C. Guo, J. Li and Q. Zeng, *Coord. Chem. Rev.*, 2025, **545**, 217018.
114 R. Verma, P. Thakur, A. Chauhan, R. Jasrotia and A. Thakur, *Carbon*, 2023, **208**, 170–190.
115 S. Feng, S. Wen, R. Wang, X. Yang, X. Yuan, Y. Liu, J. Ma and Z. Li, *Nanomaterials*, 2025, **15**, 841.
116 Z. Bai, L. Guo, J. Huang, H. Li, G. An, H. Zheng, N. Wang, Z. Li and Y. Zhu, *Chem. Eng. J.*, 2024, **479**, 147932.
117 Y. Liu, D. Luo, Y. Deng, J. Zheng, F. Wu, X. Dai and C. Deng, *J. Energy Storage*, 2023, **67**, 107641.
118 K. Sharma, V. Hasija, S. Patial, P. Singh, V. H. Nguyen, A. K. Nadda, S. Thakur, P. Nguyen-Tri, C. C. Nguyen, S. Y. Kim, Q. Van Le and P. Raizada, *Int. J. Hydrogen Energy*, 2023, **48**, 6560–6574.
119 Y. Sun, C. Song, X. Guo, S. Hong, J. Choi and Y. Liu, *J. Membr. Sci.*, 2020, **616**, 118615.
120 C. Liu, Y. Bai, W. Li, F. Yang, G. Zhang and H. Pang, *Angew. Chem., Int. Ed.*, 2022, **61**, e202116282.
121 M. Mahato, J. Kim, M. Lee, S. Jo, G. Kim, S. Nam, J. Kim, V. H. Nguyen, M. Garai, H. Yoo, D. Saatchi, Z. Ullah, C. W. Ahn, Y. Gogotsi and I. Oh, *Adv. Mater.*, 2025, 2500479.
122 X. Zhang, Z. Wang and X. Guo, *Sci. Rep.*, 2025, **15**, 3727.
123 G. Zeng, Y. Liu, Q. Lin, S. Pu, S. Zheng, M. B. M. Y. Ang and Y. H. Chiao, *Sep. Purif. Technol.*, 2022, **293**, 121052.
124 J. Zhang, Z. Li, Q. Zhang, L. Zhang, T. Ma, X. Ma, K. Liang, Y. Ying and Y. Fu, *ACS Appl. Mater. Interfaces*, 2023, **15**, 17222–17232.
125 J. Zhang, X. Cheng, J. Jiang, A. Pattanateeradetch, S. Shi, C. Chokejaroenrat, Q. Xu and J. Lu, *Inorg. Chem.*, 2025, **64**, 4920–4933.
126 N. Liu, Y. Zheng, C. Jing, B. Gao, W. Huang, Z. Li, J. Lei, X. Zhang, L. Cui and L. Tang, *J. Mol. Liq.*, 2020, **311**, 113201.
127 L. Yang, Y. Chen, Q. Wen, H. Xu, X. Pan and X. Li, *Electrochim. Acta*, 2022, **428**, 140959.
128 M. Wan, C. Shi, X. Qian, Y. Qin, J. Jing, H. Che, F. Ren, J. Li and B. Yu, *Composites, Part A*, 2022, **163**, 107187.
129 D. Cheng, P. Li, X. Zhu, M. Liu, Y. Zhang and Y. Liu, *Chin. J. Chem.*, 2021, **39**, 2181–2187.
130 J. Paul and J. Kim, *Appl. Surf. Sci.*, 2023, **613**, 156103.
131 R. Li, X. Fu, G. Liu, J. Li, G. Zhou, G. Liu and W. Jin, *J. Membr. Sci.*, 2022, **664**, 121097.
132 Y. Wen, Z. Wei, C. Ma, X. Xing, Z. Li and D. Luo, *Nanomaterials*, 2019, **9**, 775.
133 P. Xiao, G. Zhu, X. Shang, B. Hu, B. Zhang, Z. Tang, J. Yang and J. Liu, *J. Electroanal. Chem.*, 2022, **916**, 116382.
134 B. Jia, H. Yang, L. Wang, Z. Zhao and X. Wu, *Appl. Surf. Sci.*, 2022, **602**, 154386.
135 H. Li, H. Lin, S. Raza, C. Chen, W. Yu, Q. Zeng, Z. Zhao, X. Huang and L. Shen, *J. Membr. Sci.*, 2025, **718**, 123685.
136 J. Wang, Y. Shen, Y. Zhuang, J. Wang and Y. Zhang, *Anal. Chem.*, 2024, **96**, 12102–12111.
137 W. Han, Y. Yan, H. Wang, J. Li, P. Zhao, Z. Liu, F. Yu, J. Cui and G. Zhang, *Langmuir*, 2024, **40**, 21767–21779.
138 Y. Liu, X. Meng, Z. Ma, H. Gu, X. Luo, X. Yin, H. Yi and Y. Chen, *Food Chem.*, 2025, **463**, 141496.
139 R. Ramachandran, K. Rajavel, W. Xuan, D. Lin and F. Wang, *Ceram. Int.*, 2018, **44**, 14425–14431.
140 X. Liang, X. Ren, Q. Yang, L. Gao, M. Gao, Y. Yang, H. Zhu, G. Li, T. Ma and A. Liu, *Nanoscale*, 2021, **13**, 2843–2848.
141 M. Wan, C. Shi, X. Qian, Y. Qin, J. Jing and H. Che, *Nanomaterials*, 2022, **12**, 1142.
142 N. Li, L. Yang, R. Su, N. Shi, J. Wu, J. Zhao, L. Wen and Z. Wang, *Desalination*, 2023, **566**, 116940.
143 K. S. Ranjith, S. Sonwal, A. Mohammadi, G. Seeta Rama Raju, M.-H. Oh, Y. S. Huh and Y.-K. Han, *J. Mater. Chem. A*, 2024, **12**, 26132–26146.
144 D. Roy, R. Singh, S. Mandal and N. Chanda, *Anal. Methods*, 2024, **16**, 6183–6192.
145 J. Ding, Q. Wang, X. Liu, S. Li and H. Li, *J. Hazard. Mater.*, 2024, **480**, 136261.
146 J. Qin, B. Liu, K. H. Lam, S. Song, X. Li and X. Hu, *ACS Sustain. Chem. Eng.*, 2020, **8**, 17791–17799.
147 L. Cheng, Y. Tang, M. Xie, Y. Sun and H. Liu, *J. Alloys Compd.*, 2021, **864**, 158913.
148 X. Zhang, S. Yang, W. Lu, D. Lei, Y. Tian, M. Guo, P. Mi, N. Qu and Y. Zhao, *J. Colloid Interface Sci.*, 2021, **592**, 95–102.
149 H. Zhang, Z. Li, Z. Hou, H. Mei, Y. Feng, B. Xu and D. Sun, *Chem. Eng. J.*, 2021, **425**, 130602.
150 A. Ganiyat Olatoye, W. Li, E. Oluwaseyi Fagbohun, X. Zeng, Y. Zheng and Y. Cui, *J. Electroanal. Chem.*, 2023, **928**, 117036.
151 X. Yang, Y. Tian, S. Li, Y. P. Wu, Q. Zhang, D. S. Li and S. Zhang, *J. Mater. Chem. A*, 2022, **10**, 12225–12234.
152 S. Li, Y. Wang, Y. Li, J. Xu, T. Li and T. Zhang, *Nanomaterials*, 2023, **13**, 610.
153 O. P. Nanda, M. Ravipati, L. Durai and S. Badhulika, *Mater. Res. Bull.*, 2023, **168**, 112488.
154 X. Lin, D. Song, T. Shao, T. Xue, W. Hu, W. Jiang, X. Zou and N. Liu, *Adv. Funct. Mater.*, 2023, 2311637.
155 W. Xu, Y. Lu, Z. Zhang, Q. Zhou, W. Zhao, R. Yang, L. Zhang, L. Yang, X. Gao and G. Pan, *IEEE Sens. J.*, 2024, **24**, 9437–9448.
156 R. Zhu, Y. Gu, L. Liu, J. Lu and H. Pang, *New J. Chem.*, 2024, **48**, 10593–10598.
157 Y. Ji, W. Li, Y. You and G. Xu, *Chem. Eng. J.*, 2024, **496**, 154009.
158 D. S. Shivade, A. N. Kurade, R. K. Bhosale, S. S. Kundale, A. R. Shelake, A. D. Patil, P. P. Waifalkar, R. K. Kamat, A. M. Teli and T. D. Dongale, *J. Energy Storage*, 2024, **100**, 113754.
159 C. Gu, C. Lu, Y. X. Gao, P. Tan, S. S. Peng, X. Q. Liu and L. B. Sun, *Inorg. Chem.*, 2021, **60**, 1380–1387.
160 H. Hassan, E. Umar, M. W. Iqbal, A. K. Alqorashi, B. S. Almutair, H. Alrobei, A. M. Afzal and N. Ahmad, *New J. Chem.*, 2024, **48**, 6277–6295.
161 Z. Liu, H. Lv, Y. Zhang, J. W. He, L. Han, S. Li, L. Yang and Y. Xu, *ACS Sens.*, 2024, **9**, 3641–3651.

162 A. Sharma, H.-S. Lee, C.-M. Yeom, H. K. Surendran, C. Narayana, S. B. Eadi, R. Zboril, H.-D. Lee and K. Jayaramulu, *Chem. Mater.*, 2024, **36**, 8466–8476.
163 H. Zhu, Y. Chen, T. Zhang, L. Qin, S. Z. Kang and X. Li, *J. Solid State Chem.*, 2023, **327**, 124298.
164 W. H. Lin, T. Y. Huang, C. H. Bai, C. H. Hung, C. A. Lung, W. H. Hung, K. Gopinadhan and L. H. Yeh, *Nano Energy*, 2024, **128**, 109924.
165 Y. Wang, W. Yang, J. Cao, Y. Liu, M. Shao, X. Xu and H. Chen, *Sens. Actuators, B*, 2024, **417**, 136066.
166 Q. Zhou, Q. Ding, Z. Geng, C. Hu, L. Yang, Z. Kan, B. Dong, M. Won, H. Song, L. Xu and J. S. Kim, *Nano-Micro Lett.*, 2025, **17**, 50.
167 Y. Ge, D. Lei, C. Zhang, Q. Zhang, J. Mu and J. Li, *Adv. Sci.*, 2025, **12**, 2500027.
168 Y. Li, P. Kamdem and X. J. Jin, *J. Electrochem. Soc.*, 2020, **167**, 110562.
169 Y. Yao, X. Han, X. Yang, J. Zhao and C. Chai, *Chin. J. Chem.*, 2021, **39**, 330–336.
170 Y. Wang, W. Sun, Y. Li, X. Zhuang, C. Tian, F. Luan and X. Fu, *Microchem. J.*, 2021, **167**, 106332.
171 N. Rabiee, M. Bagherzadeh, M. Jouyandeh, P. Zarrintaj, M. R. Saeb, M. Mozafari, M. Shokouhimehr and R. S. Varma, *ACS Appl. Bio Mater.*, 2021, **4**, 5106–5121.
172 C. Guo, F. Cheng, G. Liang, S. Zhang, S. Duan, Y. Fu, F. Marchetti, Z. Zhang and M. Du, *Adv. NanoBiomed Res.*, 2022, **2**, 2200064.
173 Y. Yao, T. Wang, L. Wu and H. Chen, *Desalination*, 2022, **543**, 116116.
174 G. Deng, M. Sun, Y. Shi, Y. Feng, Y. Lv, L. Tang, J. Gao and P. Song, *J. Clean. Prod.*, 2023, **403**, 136887.
175 L. P. Hao, A. Hanan, R. Walvekar, M. Khalid, F. Bibi, W. Y. Wong and C. Prakash, *Catalysts*, 2023, **13**, 802.
176 H. Shahriyari Far, M. Najafi, M. Hasanzadeh and R. Rahimi, *Inorg. Chem. Commun.*, 2023, **152**, 110680.
177 C. Wen, D. Guo, X. Zheng, H. Li and G. Sun, *ACS Appl. Energy Mater.*, 2021, **4**, 8231–8241.
178 S. Kashif, S. Akram, M. Murtaza, A. Amjad, S. S. A. Shah and A. Waseem, *Diam. Relat. Mater.*, 2023, **136**, 110023.
179 B. Xiang, J. Gong, Y. Sun, W. Yan, R. Jin and J. Li, *J. Membr. Sci.*, 2024, **691**, 122247.
180 A. Maleki and A. Bozorg, *Chemosphere*, 2024, **364**, 143273.
181 Y. Meng, F. Yue, S. Zhang, L. Zhang, C. Li, M. Shi, Y. Ma, M. Berrettoni, X. Zhang and H. Zhang, *Carbon Capture Sci. Technol.*, 2024, **13**, 100274.
182 Y. Liu, Y. He, E. Vargun, T. Plachy, P. Saha and Q. Cheng, *Nanomaterials*, 2020, **10**, 695.
183 C. Du, Q. Song, Q. Liang, X. Zhao, J. Wang, R. Zhi, Y. Wang and H. Yu, *ChemNanoMat*, 2021, **7**, 539–544.
184 F. Wu, Z. Liu, J. Wang, T. Shah, P. Liu, Q. Zhang and B. Zhang, *Chem. Eng. J.*, 2021, **422**, 130591.
185 T. Xiao, J. Jin, Y. Zhang, W. Xi, R. Wang, Y. Gong, B. He and H. Wang, *Electrochim. Acta*, 2022, **427**, 140851.
186 L. Yue, L. Chen, X. Wang, D. Lu, W. Zhou, D. Shen, Q. Yang, S. Xiao and Y. Li, *Chem. Eng. J.*, 2023, **451**, 138687.
187 P. Tan, R. Gao, Y. Zhang, N. Han, Y. Jiang, M. Xu, S. J. Bao and X. Zhang, *J. Colloid Interface Sci.*, 2023, **630**, 363–371.
188 D. Xu, Z. Zhang, K. Tao and L. Han, *Dalton Trans.*, 2023, **52**, 2455–2462.
189 J. Liu, Q. Xia, L. Wang, Q. Hu, N. M. Shinde and A. Zhou, *ACS Appl. Mater. Interfaces*, 2024, **16**, 49380–49391.
190 M. Murtaza, K. Farooq, W. A. Shah, I. Ahmad and A. Waseem, *Nanoscale Adv.*, 2024, **6**, 6317–6327.
191 K. Yu, J. Zhang, Y. Hu, L. Wang, X. Zhang and B. Zhao, *Catalysts*, 2024, **14**, 184.
192 Z. Li, S. Ning, F. Hu, H. Zhu, L. Zeng, L. Chen, X. Wang, T. Fujita and Y. Wei, *J. Colloid Interface Sci.*, 2023, **629**, 97–110.
193 M. Adil, A. G. Olabi, M. A. Abdelkareem, H. Alawadhi, A. Bahaa, K. ElSaid and C. Rodriguez, *J. Energy Storage*, 2023, **68**, 107817.
194 M. Murtaza, K. Farooq, A. A. Amjad, S. S. A. Shah and A. Waseem, *Diam. Relat. Mater.*, 2024, **147**, 111379.
195 V. A. Thai, T. B. Nguyen, C. W. Chen, X. T. Bui, R. Doong and C. D. Dong, *Environ. Sci. Nano*, 2024, **11**, 3871–3886.
196 S. Li, L. Zhang, P. Ye, M. Zhu, Y. Nie, Y. Dai and F. Yang, *Cryst. Growth Des.*, 2024, **24**, 7445–7454.
197 M. Ali, A. M. Afzal, S. Mumtaz, K. Yusuf and A. Deifalla, *J. Energy Storage*, 2024, **92**, 111972.
198 S. Siva Shalini, Y. P. Fu and A. Chandra Bose, *Chem. Eng. J.*, 2024, **500**, 156751.
199 K. Gong, L. Cai, C. Shi, F. Gao, L. Yin, X. Qian and K. Zhou, *Composites, Part A*, 2022, **161**, 107109.
200 Y. Chen, S. Li, L. Zhang, T. Jing, J. Wang, L. Zhao, F. Li, C. Li and J. Sun, *J. Solid State Chem.*, 2022, **308**, 122919.
201 S. Li, H. Chai, L. Zhang, Y. Xu, Y. Jiao and J. Chen, *J. Colloid Interface Sci.*, 2023, **642**, 235–245.
202 Y. Zhang, H. Yuan, X. Chen, Z. Jiang, J. Lu and F. Xin, *ACS Appl. Polym. Mater.*, 2024, **6**, 8277–8290.
203 S. Li, Q. Cheng, P. Ye, Y. Zhang, L. Zhang, F. Liu, H. Qiu, X. Qu and Y. Nie, *Appl. Organomet. Chem.*, 2024, **38**, e7547.
204 K. Zhao, B. Zhang, X. Cui, X. Chao, F. Song, H. Chen and B. He, *Food Chem.*, 2024, **461**, 140828.
205 F. Yu, X. Yu, P. Jia, X. Zhou, H. Wang, Y. Hou, B. Wang, L. Song and Y. Hu, *Chem. Eng. J.*, 2024, **499**, 156145.
206 Y. Lin, W. Dong, S. Li, S. Zhang, X. Chen, B. Wang and L. Du, *Polym. Degrad. Stab.*, 2025, **234**, 111251.
207 G. Kaur, S. Sharma, N. Bhardwaj, M. K. Nayak and A. Deep, *Food Control*, 2024, **165**, 110694.
208 W. Wang, Y. Bai, P. Yang, S. Yuan, F. Li, W. Zhao, B. Jin, X. Zhang, S. Liu, D. Yuan and Q. Zhao, *Sci. Bull.*, 2023, **68**, 2180–2189.
209 G. Dai, Y. Li, Z. Li, J. Zhang, X. Geng, F. Zhang, Q. Wang and P. He, *ACS Appl. Nano Mater.*, 2022, **5**, 9201–9208.
210 H. Huang, J. Qin, C. Liu, L. Luo, Y. Lan, L. Yang, J. Zhang and H. He, *Carbon*, 2024, **226**, 119171.
211 W. Wen, Y. Dang, J. Tang, C. Su, S. Yu, J. Ma and Y. Zhou, *J. Electrochem. Soc.*, 2024, **171**, 057514.
212 X. Zhang, H. Wang, R. Dai, P. Zhao and Y. Wang, *J. Colloid Interface Sci.*, 2025, **690**, 137278.
213 Z. H. Lu, Q. Tian, D. D. Zhou, M. Chen, Y. W. Cao, L. Y. Zhuang, X. Liu, Z. H. Yang and I. A. Senosy, *J. Environ. Chem. Eng.*, 2022, **10**, 108037.

214 J. Chi, P. Ju, F. Bi, T. Jiang, S. Wen, Y. Cai, L. Wang and M. Qiu, *Adv. Funct. Mater.*, 2025, **35**, 2415174.
215 X. Tu, F. Gao, X. Ma, J. Zou, Y. Yu, M. Li, F. Qu, X. Huang and L. Lu, *J. Hazard. Mater.*, 2020, **396**, 122776.
216 S. M. S. Rana, M. T. Rahman, M. A. Zahed, S. H. Lee, Y. Do Shin, S. Seonu, D. Kim, M. Salauddin, T. Bhatta, K. Sharstha and J. Y. Park, *Nano Energy*, 2022, **104**, 107931.
217 A. Rajan, M. Daniel, J. Rafi, A. R. S. C. Lazuli and B. Neppolian, *ChemSusChem*, 2024, **18**, e202400207.
218 Y. Qi, Y. Chen, Q. Li, X. Dang and H. Chen, *Anal. Chim. Acta*, 2024, **1316**, 342876.
219 H. Hassan, K. Khan, S. Mumtaz, A. A. Rafi, A. M. Idris, A. Althobaiti and A. Mohammad, *J. Power Sources*, 2024, **623**, 235486.
220 Z. F. Lin, T. H. Wang, P. Venkatesan and R. A. Doong, *Chem. Eng. J.*, 2025, **505**, 159411.
221 X. Zhao, M. Zhu, C. Tang, K. Quan, Q. Tong, H. Cao, J. Jiang, H. Yang and J. Zhang, *J. Colloid Interface Sci.*, 2022, **620**, 478–485.
222 L. Guo, L. Tao and T. Wang, *Langmuir*, 2024, **40**, 8862–8871.
223 X. Liang, Y. Yan, G. Liu, S. Hou and S. Hou, *Chem. Eng. J.*, 2024, **483**, 149301.
224 S. Hou, M. Wen, J. Wei, L. Li and G. Liu, *J. Mol. Struct.*, 2025, **1321**, 140076.
225 X. Zhu, F. Liu, L. Meng, Q. Gao, X. Wang, M. Lou, X. Xu, W. Zhang, F. Li and B. Van der Bruggen, *Nano Lett.*, 2025, **25**, 2810–2819.
226 H. Yang, P. Zhang, Q. Zheng, A. Hayat, H. S. M. Abd-Rabboh, S. Raza, D. Li and Y. Sui, *J. Mater. Chem. C*, 2024, **12**, 17620–17634.
227 C. Sun, D. Lan, Z. Jia, Z. Gao and G. Wu, *Small*, 2024, **20**, 2405874.
228 H. Yang, S. Yin, P. Zhang, Q. Zheng, S. Raza, D. Li and Y. Sui, *Sep. Purif. Technol.*, 2025, **365**, 132600.
229 J. Bian, M. Liu, X. Liu, X. Bian, C. Gu, J. Ma and T. Jiang, *Microchem. J.*, 2025, **210**, 113021.
230 H. Gao, J. You, H. Wu and M. Tian, *Food Chem.*, 2025, **473**, 143092.
231 J. Wang, Y. Zhang, Z. Chen, Z. Zhou, J. Wang, C. Ma, W. Qiao, Z. Xu and L. Ling, *J. Colloid Interface Sci.*, 2025, **678**, 79–88.
232 H. B. Parse, I. Patil, B. Kakade and A. Swami, *Energy Fuels*, 2021, **35**, 17909–17918.
233 X. Han, Y. Huang, L. Ding, Y. Song, T. Li and P. Liu, *ACS Appl. Nano Mater.*, 2021, **4**, 691–701.
234 Z. Xiang, Y. Shi, X. Zhu, L. Cai and W. Lu, *Nano-Micro Lett.*, 2021, **13**, 150.
235 Z. Liu, J. Chen, M. Que, H. Zheng, L. Yang, H. Yuan, Y. Ma, Y. Li and X. Yang, *Chem. Eng. J.*, 2022, **450**, 138442.
236 W. Liu, X. Liu, X. Tan, M. Zhao, Z. Liu, M. Yi, Q. Ding, Y. Ren and H. Li, *Sens. Actuators, B*, 2025, **433**, 137577.
237 C. Ji, C. Yan, Z. Wei, T. Yu, J. Fan and Y. Li, *Chem. Eng. J.*, 2024, **483**, 149431.
238 W. Xie, Y. Wang, J. Zhou, M. Zhang, J. Yu, C. Zhu and J. Xu, *Appl. Surf. Sci.*, 2020, **534**, 147584.
239 B. Lei, X. Huang, P. Wu, L. Wang, J. Huang and Z. Wang, *Ceram. Int.*, 2022, **48**, 25111–25119.
240 C. Shi, Z. Long, C. Wu, H. Dai, Z. Li, H. Qiao, K. Liu, Q. H. Fan and K. Wang, *Small*, 2023, **19**, 2303802.
241 S. R. Shingte, V. D. Chavan, R. P. Dhavale, D.-K. Kim, H.-H. Park, T. D. Dongale and P. B. Patil, *J. Energy Storage*, 2024, **92**, 112169.
242 M. Liu, J. Wang, P. Song, J. Ji and Q. Wang, *Sens. Actuators, B*, 2022, **361**, 131755.
243 S. Zhang, Y. Ding, Q. Wang and P. Song, *Sens. Actuators, B*, 2023, **393**, 134122.
244 A. Wei, L. Wang and Z. Li, *J. Alloys Compd.*, 2022, **899**, 163369.
245 T. Kshetri, D. D. Khumujam, T. I. Singh, Y. S. Lee, N. H. Kim and J. H. Lee, *Chem. Eng. J.*, 2022, **437**, 135338.
246 W. Wu, C. Zhao, H. Liu, T. Liu, L. Wang and J. Zhu, *J. Colloid Interface Sci.*, 2022, **623**, 216–225.
247 X. Bu, F. Ma, Q. Wu, H. Wu, Y. Yuan, L. Hu, C. Han, X. Wang, W. Liu and X. Li, *Sens. Actuators, B*, 2022, **369**, 132232.
248 H. Geun Oh and S. K. Park, *Appl. Surf. Sci.*, 2021, **564**, 150415.
249 Y. Zhou, Y. Wu, D. Guo, J. Li, D. Chu, S. Na, M. Yu, D. Li, G. Sui and D. F. Chai, *J. Alloys Compd.*, 2023, **963**, 171133.
250 M. T. Rahman, S. M. S. Rana, M. Salauddin, M. A. Zahed, S. Lee, E. S. Yoon and J. Y. Park, *Nano Energy*, 2022, **100**, 107454.
251 J. Wang, Y. Huang, S. Zhang, X. Du, Z. Duan and X. Sun, *J. Mater. Sci. Technol.*, 2023, **147**, 112–123.
252 D. Wang, D. Zhang, Y. Yang, Q. Mi, J. Zhang and L. Yu, *ACS Nano*, 2021, **15**, 2911–2919.
253 D. Song, X. Jiang, Y. Li, X. Lu, S. Luan, Y. Wang, Y. Li and F. Gao, *J. Hazard. Mater.*, 2019, **373**, 367–376.
254 H. Zong, L. Hu, Z. Wang, R. Qi, K. Yu and Z. Zhu, *Chem. Eng. J.*, 2021, **416**, 129102.
255 X. Liu, F. Liu, X. Zhao and L. Z. Fan, *J. Mater.*, 2022, **8**, 30–37.
256 H. Zong, R. Qi, K. Yu and Z. Zhu, *Electrochim. Acta*, 2021, **393**, 139068.
257 J. Li, C. Chen, Z. Lv, W. Ma, M. Wang, Q. Li and J. Dang, *J. Mater. Sci. Technol.*, 2023, **145**, 74–82.
258 H. Wang, J. Zhao, J. Yu and Z. Wang, *Synth. Met.*, 2023, **292**, 117215.
259 Y. Ma, H. Zhang, H. Cong, Y. Wang, S. Xin, P. Xu, Y. Qin, G. Xu, X. Kang and F. Wang, *J. Alloys Compd.*, 2023, **968**, 171985.
260 Y. Cui, L. Zhao, D. He, J. Sun, J. Yang, W. Tang, H. Yu, C. Lou, W. Wang, X. Zhang and H. Zhao, *ACS Appl. Mater. Interfaces*, 2024, **16**, 47751–47762.
261 M. Zhang, S. Yun, T. Yang, G. Yang, M. Sun, J. Dang, Z. Wang, H. Yang, S. Yuan, A. Arshad and K. Wang, *J. Mater. Chem. A*, 2024, **12**, 29479–29492.
262 T. Hou, Z. Jia, B. Wang, H. Li, X. Liu, Q. Chi and G. Wu, *Chem. Eng. J.*, 2021, **422**, 130079.
263 Y. Yang, X. Huang, C. Sheng, Y. Pan, Y. Huang and X. Wang, *J. Alloys Compd.*, 2022, **920**, 165908.
264 H. Li, J. Li, L. Ma, X. Zhang, J. Li, J. Li, T. Lu and L. Pan, *J. Mater. Chem. A*, 2023, **11**, 2836–2847.

265 X. Shi, W. Liang, G. Liu, B. Chen, L. Shao, Y. Wu, Z. Sun and F. García, *Chem. Eng. J.*, 2023, **462**, 142271.
266 L. Wang, Z. Liu, Y. Ma, Z. Li, M. Xiao, B. Tu and H. Song, *Dalton Trans.*, 2023, 572–581.
267 W. Liang, M. Liu, X. Shi, B. Chen, L. Shao, J. Xu and Z. Sun, *Batter. Supercaps*, 2023, **7**, e202300462.
268 R. Hu, D. Sha, X. Cao, C. Lu, Y. Wei, L. Pan and Z. M. Sun, *Adv. Energy Mater.*, 2022, **12**, 2203118.
269 J. H. Na, H. G. Oh, S. Lee and S. K. Park, *J. Mater. Chem. A*, 2023, **12**, 2848–2855.
270 S. Vallem, S. Song, Y. Oh, J. Kim, M. Li, Y. Li, X. Cheng and J. Bae, *J. Colloid Interface Sci.*, 2024, **665**, 1017–1028.
271 Y. Xue, W. Li, R. Liu, T. Zhao, Y. Lv, J. Li, Y. Guo, R. Hao, X. Liu and H. He, *Batter. Supercaps*, 2025, e202400770.
272 H. Zou, B. He, P. Kuang, J. Yu and K. Fan, *ACS Appl. Mater. Interfaces*, 2018, **10**, 22311–22319.
273 J. Wei, F. Hu, C. Lv, L. Bian, X. Quan and Q. Ouyang, *Small*, 2025, **21**, 2411146.
274 Q. Li, Q. Jiao, Y. Yan, H. Li, W. Zhou, T. Gu, X. Shen, C. Lu, Y. Zhao, Y. Zhang, H. Li and C. Feng, *Chem. Eng. J.*, 2022, **450**, 137922.
275 M. Adil, A. G. Olabi, M. A. Abdelkareem, H. Alawadhi, A. Bahaa, K. ElSaid and C. Rodriguez, *J. Energy Storage*, 2023, **60**, 106537.
276 K. Farooq, M. Murtaza, Z. Yang, A. Waseem, Y. Zhu and Y. Xia, *Nanoscale Adv.*, 2024, **6**, 3169–3180.
277 L. Hu, R. Xiao, X. Wang, X. Wang, C. Wang, J. Wen, W. Gu and C. Zhu, *Appl. Catal., B*, 2021, **298**, 120599.
278 K. Kasinathan, Y. K. Park, B. Ravindran, K. Marimuthu, G. Munuswamy-Ramanujam, S. Woong Chang and J. H. Yim, *Chem. Eng. J.*, 2024, **482**, 149088.
279 A. Alshraim, S. Rahman, M. Al-Gawati, A. N. Grace and A. N. Alodhayb, *Int. J. Electrochem. Sci.*, 2025, **20**, 100980.
280 Y. Zhang, Z. Li, B. Qu, X. Shen, L. Tong, J. Wang, J. Cui, X. Li, Q. Xie and J. Wang, *Inorg. Chem.*, 2025, **64**, 6822–6831.
281 X. Liu, Y. Zhang and Y. Q. Liu, *Appl. Surf. Sci.*, 2025, **694**, 162859.
282 J. Zhou, G. Zhang, J. Luo, Y. Hu, G. Hao, H. Guo, F. Guo, S. Wang and W. Jiang, *Chem. Eng. J.*, 2021, **426**, 130725.
283 W. Gu, M. Wu, J. Xu and T. Zhao, *Int. J. Hydrogen Energy*, 2022, **47**, 17224–17232.
284 T. Wu, F. Ren, Z. Guo, J. Zhang, X. Hou, Z. Chen, Y. Jin and P. Ren, *J. Alloys Compd.*, 2024, **976**, 172984.
285 Q. Liao, M. He, Y. Zhou, S. Nie, Y. Wang, B. Wang, X. Yang, X. Bu and R. Wang, *Langmuir*, 2018, **34**, 15854–15863.
286 B. Deng, Z. Xiang, J. Xiong, Z. Liu, L. Yu and W. Lu, *Nano-Micro Lett.*, 2020, **12**, 55.
287 M. Wang, P. Zhou, T. Feng, Z. Song, Q. Ren, H. Gu, X. Shi, Q. Zhang and L. Wang, *Ceram. Int.*, 2022, **48**, 22681–22690.
288 C. Cui, L. Geng, S. Jiang, W. Bai, L. Dai, E. Ren, L. Liu and R. Guo, *Ind. Eng. Chem. Res.*, 2023, **62**, 8297–8311.
289 J. Zheng, C. Xu, Z. Li, C. Gu, X. Li, Z. Li, Y. Li, G. Lou and Y. Chen, *J. Mater. Chem. A*, 2024, **12**, 29103–29112.
290 Z. Guo, Y. Zhao, P. Luo, J. Wang, L. Pei, H. Yu, P. Song, F. Ren and P. Ren, *Chem. Eng. J.*, 2024, **497**, 155707.
291 Y. Yao, Y. Ma, C. Chen, K. Zhu, G. Wang, D. Cao and J. Yan, *J. Energy Storage*, 2025, **114**, 115877.
292 Q. Liu, H. Zhang, J. Xie, F. Yang, Z. Yang, X. Liu, H. Wu, Q. Liu and X. Lu, *Nano Energy*, 2023, **113**, 108567.
293 Y. Wang, R. Niu, L. Chen, Y. Yang, H. Yu and X. Qiu, *Chem. Eng. J.*, 2025, **512**, 162305.
294 M. Daniel, G. Mathew, M. Anpo and B. Neppolian, *Coord. Chem. Rev.*, 2022, **468**, 214627.
295 B. Mohanty, S. Kumari, P. Yadav, P. Kanoo and A. Chakraborty, *Coord. Chem. Rev.*, 2024, **519**, 216102.
296 Y. Lu, J. Sun, W. Xu, X. Di, W. Zhao, L. Zhang and G. Pan, *IEEE Sens. J.*, 2025, **25**, 5294–5303.
297 S. Vallem, S. Venkateswarlu, Y. Li, S. Song, M. Li and J. Bae, *Energy Storage Mater.*, 2024, **65**, 103159.
298 K. Farooq, Z. Yang, M. Murtaza, M. A. Naseeb, A. Waseem, Y. Zhu and Y. Xia, *Adv. Energy Sustain. Res.*, 2025, 2400400.
299 J. Liu, L. Chen, H. Cui, J. Zhang, L. Zhang and C.-Y. Su, *Chem. Soc. Rev.*, 2014, **43**, 6011–6061.
300 Y. Wang, J. Chen, J. Shi, J. Zhang, Y. Ma, X. Yang and Y. Li, *Appl. Surf. Sci.*, 2025, **710**, 163965.
301 B. Shan, Y. Wang, X. Ji and Y. Huang, *Nano-Micro Lett.*, 2024, **16**, 212.
302 F. Wu, P. Hu, F. Hu, Z. Tian, J. Tang, P. Zhang, L. Pan, M. W. Barsoum, L. Cai and Z. Sun, *Nano-Micro Lett.*, 2023, **15**, 194.
303 G. Song, Y. Shi, S. Jiang and H. Pang, *Adv. Funct. Mater.*, 2023, **33**, 2303121.
304 J. Liu, T. A. Goetjen, Q. Wang, J. G. Knapp, M. C. Wasson, Y. Yang, Z. H. Syed, M. Delferro, J. M. Notestein, O. K. Farha and J. T. Hupp, *Chem. Soc. Rev.*, 2022, **51**, 1045–1097.
305 S. Bai, M. Yang, J. Jiang, X. He, J. Zou, Z. Xiong, G. Liao and S. Liu, *npj 2D Mater. Appl.*, 2021, **5**, 78.
306 Z. Qian, R. Zhang, Y. Xiao, H. Huang, Y. Sun, Y. Chen, T. Ma and X. Sun, *Adv. Energy Mater.*, 2023, **13**, 2300086.
307 A. Fattah-alhosseini, Z. Sangarimotlagh, M. Karbasi and M. Kaseem, *Nano-Struct. Nano-Objects*, 2024, **38**, 101192.
308 Y. Chen, Y. Qiu, T. Chen and H. Wang, *ACS Nano*, 2025, **19**, 6588–6600.
309 M. Garai, M. Mahato, S. Nam, E. Kim, D. Seo, Y. Lee, V. H. Nguyen, S. Oh, P. Sambyal, H. Yoo, A. K. Taseer, S. A. Syed, H. Han, C. W. Ahn, J. Kim and I. K. Oh, *Adv. Funct. Mater.*, 2023, **33**, 2212252.
310 F. Wei, F. Liang, Y. Zhao, Z. Ji, T. Yan, R. Li, H. Liu, Y. Kong, H. He, W. Huang, C. Cao, W. Zhang, B. Fei and M. Ge, *J. Mater. Chem. A*, 2025, **13**, 13070–13080.
311 L. Sun, H. Wang, S. Zhai, J. Sun, X. Fang, H. Yang, D. Zhai, C. Liu, W. Q. Deng and H. Wu, *J. Energy Chem.*, 2023, **76**, 368–376.
312 H. Zhang, D. Xiong, Y. Xie, K. Wu, Z. Feng, K. Wen, Z. Li and M. He, *Colloids Surf., A*, 2023, **656**, 130332.
313 W. Wang, J. Si, L. Yue, W. Zhang, Q. Chen, H. Huang, F. Lin, Y. Zhao, S. Meng and L. Liu, *Chem. Eng. J.*, 2025, **507**, 160363.
314 J. Sun, L. Zhang, F. Li, F. Yang, M. Liu, S. Li and D. Zhang, *Adv. Funct. Mater.*, 2025, 2501181.
315 J. Li, X. Qiang, B. Jia, L. Wang and X. Wu, *Appl. Surf. Sci.*, 2025, **695**, 162867.

316 M. Saeed, S. Sharif, J. H. Shah, T. T. R. Afzal, M. Shahbaz, A. M. Shehzad, A. Shahzad, O. Şahin and S. Shahzad, *RSC Adv.*, 2025, **15**, 17130–17141.
317 J. Kunwar, D. Acharya, K. Chhetri, B. Karki, B. Deo, R. M. Bhattarai, S. Neupane, M. P. Adhikari and A. P. Yadav, *J. Electroanal. Chem.*, 2023, **950**, 117915.
318 C. Ruan, D. Zhu, J. Qi, Q. Meng, F. Wei, Y. Ren, Y. Sui and H. Zhang, *Surf. Interfaces*, 2021, **25**, 101274.
319 I. Pathak, D. Acharya, K. Chhetri, P. Chandra Lohani, S. Subedi, A. Muthurasu, T. Kim, T. H. Ko, B. Dahal and H. Y. Kim, *J. Mater. Chem. A*, 2023, **11**, 5001–5014.
320 C. Liu, W. Feng, Y. Bai and H. Pang, *Inorg. Chem. Front.*, 2022, **9**, 5463–5468.
321 N. Hussain and S. M. Mobin, *Chem. Sci.*, 2025, **16**, 8460–8469.
322 Y. Shi, F. Dong, A. Rodas-Gonzalez, G. Wang, L. Yang, S. Chen, H.-B. Zheng and S. Wang, *Food Chem.*, 2025, **475**, 143362.
323 Y. Wang, X. Wang, M. Chu, J. Xin, Y. Liu, H. Pang, G. Yang and H. Ma, *Anal. Chim. Acta*, 2025, **1346**, 343770.
324 X. Wang, X. Bai, W. Wang, Z. Zhao and J. Shan, *J. Electrochem. Soc.*, 2023, **170**, 037519.
325 M. Ravipati, D. Ramasamy and S. Badhulika, *Electrochim. Acta*, 2025, **525**, 146154.
326 X. Zheng, M. Yuan, P. Su, J. Xu and G. Sun, *Appl. Surf. Sci.*, 2025, **692**, 162742.
327 M. Murtaza, K. Farooq, W. A. Shah and A. Waseem, *Fuel*, 2025, **394**, 135095.
328 Z. H. Zhu, X. Y. Wu, J. F. Lu, H. Xu, S. L. Hou, J. Zhao, S. J. Liu and H. R. Wen, *Inorg. Chem.*, 2025, **64**, 8261–8269.
329 A. P. Tiwari, P. Chandra, M. S. Rahman, K. A. Mirica and W. J. Scheideler, *Nanoscale*, 2025, **17**, 11028–11036.
330 J. Jiang, C. Xi, Y. Zhao, Y. Zhu, K. Hu, Y. Wang, S. Wang, Z. Zhang and S. Han, *ACS Catal.*, 2025, **15**, 2561–2575.
331 I. Pathak, D. Acharya, K. Chhetri, Y. R. Rosyara, A. Muthurasu, T. Kim, T. H. Ko and H. Y. Kim, *Composites, Part B*, 2025, **296**, 112238.
332 T. Fang, J. Ma, Y. Dai, J. Gou, X. Li, C. Li and J. Tong, *ACS Appl. Nano Mater.*, 2025, **8**, 3519–3526.
333 S. Raza, A. U. Rehman, C. Chen, T. Zhao, A. Hayat, T. Bashir, L. Shen, Y. Orooji and H. Lin, *J. Mater. Chem. A*, 2025, **13**, 4390–4403.
334 X. Guo, H. Zhang, Y. Yao, C. Xiao, X. Yan, K. Chen, J. Qi, Y. Zhou, Z. Zhu, X. Sun and J. Li, *Appl. Catal., B*, 2023, **323**, 122136.
335 W. Zhan, L. Ma and M. Gan, *Mater. Today Chem.*, 2022, **26**, 101041.
336 Y. Zhou, Y. Duan, Y. Liu, Y. Geng, Z. Jin, L. Yu and S. Li, *Appl. Surf. Sci.*, 2025, **691**, 162621.
337 Z. Lin, H. Xiao, Y. Chen and H. Cai, *J. Alloys Compd.*, 2025, **1020**, 179368.
338 Q. Peng, W. Yu, C. Gao, L. Geng, P. Fatehi, S. Wang and F. Kong, *Adv. Compos. Hybrid Mater.*, 2025, **8**, 232.
339 G. Zhang, G. Zhang, H. Zhang, Y. Lu, Q. Shi, R. Li and J. Song, *Appl. Surf. Sci.*, 2025, **688**, 162327.
340 Y. Zhu, Y. Yang, S. Li, C. Zhu, Z. Qiu and Q. Zhu, *New J. Chem.*, 2025, **49**, 2889–2897.
341 M. H. Memon, A. Mir, F. Rehman, U. Amjad and M. Mustafa, *Energy Technol.*, 2025, 2500041.
342 P. Wang, B. He, B. Wang, S. Liu, Q. Ye, F. Zhou and W. Liu, *Chem. Eng. J.*, 2023, **474**, 145835.
343 A. S. Alqahtani, A. S. Alahmari, Z. E. Eldin and S. Elbeltagi, *Inorg. Chem. Commun.*, 2025, **176**, 114128.